INVESTIGATION OF DROPLET BREAKUP IN ACTIVE-GRID GENERATED ANISOTROPIC TURBULENT FLOW

ONUR ŞEN

ÖZYEĞİN UNIVERSITY

SEPTEMBER, 2025

INVESTIGATION OF DROPLET BREAKUP IN ACTIVE-GRID GENERATED ANISOTROPIC TURBULENT FLOW

by
Onur Şen

Thesis
Submitted in Partial Fulfillment of the
Requirements for the Degree of

Master of Science

in
Mechanical Engineering

Advisor: Assoc. Prof. Özgür Ertunç

Graduate School of Science and Engineering
Özyeğin University
İstanbul

September, 2025

INVESTIGATION OF DROPLET BREAKUP IN ACTIVE-GRID GENERATED ANISOTROPIC TURBULENT FLOW

Approved by:

Associate Professor Özgür Ertunç, Advisor
Department of Mechanical Engineering
Özyeğin University

Assistant Professor Altuğ Melik Başol
Department of Mechanical Engineering
Özyeğin University

Professor Metin Muradoğlu
Department of Mechanical Engineering
Koç University

Approval Date: July 24, 2025

Dedicated to my cherished parents, sister, and dear friends whose inspiration and unwavering support have been crucial throughout my pursuits.

DECLARATION OF ORIGINALITY

I hereby declare that I am the sole author of this thesis and that this is the true copy of my thesis, including the final revisions, approved by my thesis committee. All data and information have been obtained, produced, and presented in accordance with the rules of research ethics and principles of academic honesty. As required by these rules, to the best of my knowledge I have acknowledged ideas, thoughts, and any copyrighted material in accordance with the standard referencing rules. I certify that any part of this thesis has not been submitted for a degree or diploma in another educational institution.

Onur ŞEN

ABSTRACT

Droplet breakup mechanisms play a critical role in various engineering systems, with their behavior strongly dependent on continuous fluid parameters, particularly velocity. While traditional studies define breakup modes across Weber number regimes under uniform flow conditions, the influence of turbulence on droplet breakup remains poorly understood. This study investigates the effect of turbulence on droplet instability to enhance atomization understanding. An experimental setup was designed incorporating a radial fan and an active grid system with ten independent shafts and square winglets, coupled with a specific-ratio nozzle to generate controlled anisotropic turbulence. Through high-speed imaging and hotwire-anemometry measurements, 7,200 droplets were analyzed alongside nearly 1 billion hotwire measurements, which is equivalent to a total of 48 hours of hotwire measurement campaign. Results demonstrated that active grid motion significantly altered droplet breakup mechanisms, particularly in lower Weber number ranges where atomization changes were most pronounced. Image processing quantification of atomization intensity confirmed these effects. These results also display the significant effects of the local turbulent structures and their statistical properties, such as turbulent kinetic energy and dissipation rate, on the instability and breakup regimes of the droplets. These results may be used to update existing models for more accurate prediction of turbulent breakup mechanisms and, at the same time, design of effective systems with increased atomization efficiency.

Keywords: Anisotropic Turbulence, Secondary Atomization, Rapid Distortion Theory, Active Grid, Hot-wire Anemometry

ÖZET

Damla parçalanma mekanizmaları, çeşitli mühendislik sistemlerinde kritik bir rol oynamakta olup, davranışları büyük ölçüde sürekli fazın parametrelerine, özellikle de hıza bağlıdır. Geleneksel çalışmalar, üniform akış koşulları altında Weber sayısı rejimlerine göre parçalanma modlarını tanımlasa da, türbülansın damla parçalanması üzerindeki etkisi hâlâ yeterince anlaşılmamıştır. Bu çalışma, türbülansın damla kararsızlığı üzerindeki etkisini araştırarak atomizasyon sürecine dair anlayışı derinleştirmeyi amaçlamaktadır. Bu amaçla, kontrollü anizotropik türbülans oluşturmak üzere belirli oranlı bir nozül ile eşleştirilmiş, on bağımsız şafta ve kare kanatçıklara sahip aktif ızgara sistemi ve radyal fan içeren deneysel bir düzenek tasarlanmıştır. Yüksek hızlı görüntüleme ve sıcak telli anemometri ölçümleri aracılığıyla 7.200 damla ve yaklaşık 1 milyar sıcak tel verisi analiz edilmiştir. Elde edilen sonuçlar, aktif ızgara hareketinin damla parçalanma mekanizmalarını önemli ölçüde değiştirdiğini, özellikle de düşük Weber sayısı aralığında atomizasyondaki değişimlerin daha belirgin olduğunu göstermiştir. Görüntü işleme ile yapılan atomizasyon yoğunluğu analizleri bu etkileri doğrulamıştır. Ayrıca elde edilen bulgular, yerel türbülans yapılarının ve bunlara ait türbülans kinetik enerjisi ile dağılım hızı gibi özelliklerin damlaların kararsızlık ve parçalanma rejimleri üzerindeki etkilerini açıkça ortaya koymuştur. Bu sonuçlar, mevcut modellerin güncellenmesinde ve aynı zamanda atomizasyon verimliliği yüksek sistemlerin tasarımında kullanılabilir.

Anahtar Kelimeler: Anizotropik Türbülans, İkincil Atomizasyon, Hızlı Bozulma Teorisi, Aktif Izgara, Sıcak Tel Anemometrisi

ACKNOWLEDGEMENTS

I would like to extend my deepest gratitude to my advisor, Assoc. Prof. Özgür Ertunç. It has been a privilege to work under his supervision both as a master's student and a research assistant. I am sincerely thankful for his wisdom, mentorship, unwavering support, patient guidance, and invaluable insights throughout the course of this thesis. His encouragement and expertise have been instrumental to the completion of this work, and I consider it an honor to have learned from him during my graduate studies.

I also wish to express my sincere appreciation to the members of my thesis committee, Asst. Prof. Altuğ M. Başol and Prof. Metin Muradoğlu, for their valuable time, thoughtful feedback, and contributions to the review of this thesis.

I gratefully acknowledge the Scientific and Technological Research Council of Türkiye (TÜBİTAK) for the financial support provided through project 119M087. I would also like to thank Kale Jet Engines for their support of this study.

I am thankful to all of my colleagues at the Fluid Dynamics and Spray Laboratory, specifically Veli Can Coşar, and Gökhan Kayansalçık, and İbrahim Bağlıca for the technical and non-technical discussions, and their assistance during my time at Özyeğin University.

Finally, I am forever grateful to my parents, Mustafa and Bahar, for their unconditional love and unwavering support. Their sacrifices have been the foundation of my journey. I also extend my heartfelt thanks to my sister, Selin, whose constant encouragement has meant a great deal to me. The trust and resilience my family has shown throughout this endeavor will always remain a profound source of strength in my life.

TABLE OF CONTENTS

DECLARATION OF ORIGINALITY iv

ABSTRACT v

ÖZET vi

ACKNOWLEDGEMENTS vii

LIST OF TABLES x

LIST OF FIGURES xi

LIST OF ACRONYMS AND ABBREVIATIONS xiv

LIST OF SYMBOLS xv

1 INTRODUCTION 1

1.1 Aerodynamic Droplet Breakup 1

1.2 Numerical Modeling of Turbulence 9

1.2.1 Rapid Distortion Theory (RDT) 13

1.3 Active Grid Generated Turbulence 16

1.4 Open Fields in the Literature 19

1.5 Hypothesis of the Study 20

1.6 Objectives of the Study 20

1.7 Methodology 21

1.8 Structure of the Thesis 22

2 WIND TUNNEL DESIGN FOR DROPLET ATOMIZATION UNDER ANISOTROPIC TURBULENCE CONDITIONS 24

2.1 Design of the Anisotropic Wind Tunnel 24

2.2 Active Grid Design 28

2.3 Motor Assembly 34

2.4 Diffuser Design 36

2.5 Nozzle Design 37

3 EXPERIMENTAL PROCEDURE 45
3.1 Active Grid Protocols 46
3.2 Pressure Measurement 48
3.3 Droplet Atomization Experiments 51
3.3.1 Droplet Generation 51
3.3.2 Droplet Visualization 52
3.4 Hot-wire Anemometry 54
3.4.1 Hot-wire Anemometry Experiments 55
3.4.2 Hot-wire Anemometry Calibration 56
4 RESULTS 59
4.1 Droplet Breakup Statistics 59
4.2 Turbulence Analysis 64
4.2.1 Power Spectral Density 64
4.2.2 Autocorrelation 67
4.2.3 Using Rapid Distortion Theory to Find Transverse Characteristics of Turbulence 71
4.3 Effect of Turbulence on Atomization 75
4.3.1 Break-up Modes and Probabilities 75
4.3.2 Atomization Rate 78
5 CONCLUSION AND FUTURE WORK 87
5.1 Conclusion 87
5.2 Future Works 89
6 END SECTIONS 91
6.1 Bibliography 91
6.2 Appendices 91
REFERENCES 92

LIST OF TABLES

Table 1.1: Breakup morphologies and their respective Weber number (We) ranges[1] with the addition of experimental visuals of the present study. 3

Table 3.1: Camera settings were optimized and standardized to ensure uniform image acquisition and maintain consistent imaging quality across all experimental conditions. 53

Table 3.2: Experimental data for different fan frequencies and corresponding flow parameters. 57

Table 4.1: Integral time scales corresponding to different We and grid protocols. . . . 68

Table 4.2: Integral length scales corresponding to different We and grid protocols. . 70

LIST OF FIGURES

Figure 1.1: Transition map of breakup morphologies. [2]..... 4

Figure 2.1: The overall view of the designed experimental setup. 26

Figure 2.2: Test section made from ultra-clear glasses and 2 holders for integration to the tip of the nozzle.(a) Isometric view, (b) cross-sectional view. 27

Figure 2.3: The bird eye view of the components of the setup. 28

Figure 2.4: Designed active grid. (a) Top view , (b) isometric view. 29

Figure 2.5: The open and closed states of the grid. (a) Open grid , (b) closed grid. . 30

Figure 2.6: Shaft configuration with square winglets. 31

Figure 2.7: Results of the dynamic analyses done utilizing solid stress and finite element solid energy models in STAR-CCM+ (15.06.007) for a single shaft rotating at a rate of 3000 Revolutions Per Minute (RPM); the maximum rating of the motors. 32

Figure 2.8: Lower grid foundation part manufactured using Aluminum 6013 for corrosion resistance. 33

Figure 2.9: Lower grid foundation part manufactured using Aluminum 6013 for corrosion resistance. 35

Figure 2.10: Diffuser for transferring the air from a radial fan to the active grid. Two 10mm meshes are applied to generate turbulence and avoid flow reversal. 37

Figure 2.11: Batchelor-Shaw and cubic nozzle geometries. The difference in contraction development between two geometries can be clearly seen in this representation. 39

Figure 2.12: Large Eddy Simulation (LES) analysis of Batchler-Shaw nozzle utilizing Star-CCM+ software. Vorticity along the nozzle with varying inlet conditions. The Reynolds stresses used as inlet conditions are derived from the analysis of a single rotating winglet. The inlet conditions are assumed to be isotropic where $\overline{u_1u_1} = \overline{u_2u_2} = \overline{u_3u_3}$. The inlet boundary conditions are as follows: a) $1\ m/s$, $\overline{u_iu_i} = 9.3j/kg$, b) $2\ m/s$, $\overline{u_iu_i} = 7.51j/kg$, b) $3\ m/s$, $\overline{u_iu_i} = 7.15\ j/kg$ with an input of constant length scale of 0.085 m for all conditions. 40

Figure 2.13: Rapidity profiles for different inlet velocities through the contraction... 41

Figure 2.14: A Batchelor-Shaw profile nozzle designed to yield a contraction ratio of 7.5. The nozzle is attached to the active grid through the M10 connection points near the base of the nozzle. The four joints available at the tip of the nozzle are used to connect the test section. The dimensions are in millimeter. 42

Figure 2.15: The dashed redlines represent the positions at which the gradient measurements taken with the help of line probes. 44

Figure 2.16: Velocity gradients $\partial\overline{U}_1/\partial x_1$, $\partial\overline{U}_2/\partial x_2$ and $\delta\overline{U}_3/\partial x_3$ were measured along eight transverse lines extending from the nozzle axis to the wall, distributed along the axial length of the nozzle. Reynolds Stress Model (RSM)-Quadratic Pressure-Strain model was chosen. The inlet conditions are $5\ m/s$ with $\overline{u_i u_i} = 7.34\ J/kg$ and 0.085 m for the length scale. 44

Figure 3.1: The motion protocols implemented to each individual motor. (a) Flapping protocol with a blockage rate that alternates between 30% (minimum blockage and 85% (fully blocked) as the flaps rotate 180 degrees. All motors have the same motion. (b) Optimized protocol. Each color in the plots represents the individual motion of the motors. At any instant, the blockage rate is kept constant at 52%. 47

Figure 3.2: Transparent shadowgraphy calibration plate by LaVision. 53

Figure 3.3: Calibration graphs optimized grid. The Rsquare, and Root Mean Square Error (RMSE) values can be seen above the graphs. 58

Figure 4.1: Observed droplet breakup types through various Weber ranges. Note that these Weber ranges are rough estimates among the all used active grid protocols 60

Figure 4.2: Droplet breakup statistics based on type of breakup. Each graph displays the statistics of breakup types with respect to active grid protocols. 62

Figure 4.3: Unfiltered Power Spectral Density (PSD) graph for the open grid at $We = 13, 62, 155$. 65

Figure 4.4: PSD of hot-wire data for each protocol at varying We. A 5.5 kHz low-pass filter was applied to the data to remove noise. 66

Figure 4.5: Longitudinal autocorrelation of u_1 velocity fluctuations in time for various grid protocols and We. The signal was low-pass filtered at 5.50 kHz and computed by segmenting the data into 1-second bins. 68

Figure 4.6: Longitudinal autocorrelation of u_1 velocity fluctuations in terms of length for various grid protocols and We obtained through Taylor's frozen turbulence hypothesis. The signal was low-pass filtered at 5.50 kHz and computed by segmenting the data into 1-second bins. a) $We \approx 13$, b) $We \approx 62$, c) $We \approx 170$ 69

Figure 4.7: Integral time scale of the u_1 fluctuations. 70

Figure 4.8: Integral length scale of the u_1 fluctuations. 71

Figure 4.9: Intensity of longitudinal fluctuation..... 74

Figure 4.10: Taylor scale Reynolds number found through utilizing equation (4.16). 75

Figure 4.11: The probability of break-up modes with respect to We. The breakup types are as follows; a) no breakup, b) vibrational, c) bag, d) bag-stamen, e) stamen-multibag, f) multibag, g) sheet-multibag, h) sheet. The probability distributions are calculated using Wilson Score confidence intervals due to its robustness and reliability. The error bars indicate 95% confidence intervals..... 76

Figure 4.12: Droplet breakup process captured by image processing at $We \approx 24$ for the closed grid protocol..... 79

Figure 4.13: The average rate of droplet breakup process vs. time normalized by integral time scale for $11 \geq We \geq 170$ at varying protocols. The pixel count is normalized by the initial droplet size, $D_{0_{pixel}}$ which is ≈ 300 pixels while time is normalized by integral time scale, T..... 80

Figure 4.14: Scatter plot of maximum gradients of mean atomization rate plots. Curve fit was applied as a method of filtering local fluctuations. Each fit is optimized according to its corresponding curve, then the maximum gradient is calculated. 81

Figure 4.15: The average rate of droplet breakup process vs. time normalized by $\overline{u_1 u_1}$, mean velocity $\overline{U_1}$ and droplet diameter D for $11 \geq We \geq 170$ at varying protocols..... 83

Figure 4.16: Maximum stable droplet diameter for each protocol at varying We. 86

LIST OF ACRONYMS AND ABBREVIATIONS

ABS	Acrylonitrile Butadiene Styrene
cDAQ	Compact Data Acquisition
CFD	Computational Fluid Dynamics
CTA	Constant Temperature Anemometry
DNS	Direct Numerical Simulation
HIT	Homogeneous Isotropic Turbulence
LDA	Laser Doppler Anemometry
LED	Light Emitting Diode
LES	Large Eddy Simulation
NI	National Instruments
PID	Proportional Integral Derivative
PIV	Particle Image Velocimetry
PSD	Power Spectral Density
RANS	Reynolds Averaged Navier-Stokes
RDT	Rapid Distortion Theory
RMSE	Root Mean Square Error
RPM	Revolutions Per Minute
RSM	Reynolds Stress Model
RST	Reynolds Stress Transport
SST	Shear Stress Transport

TAB	Taylor Analogy Breakup
TKE	Turbulent Kinetic Energy
USB	Universal Serial Bus
We	Weber number

LIST OF SYMBOLS

A : Constant Temperature Anemometry (CTA) calibration constant

A_{inlet} : Nozzle inlet area $[m^2]$

A_{outlet} : Nozzle outlet area $[m^2]$

B : CTA calibration constant

c : Contraction ratio, $c = A_{inlet}/A_{outlet}$

C_1 : Empirical constant arising from Kolmogorov scaling $C_1 \approx 2$

C_{ij} : Convective transport of $\overline{u_i u_j}$

D : Droplet diameter $[m]$

$D_{0_{pixel}}$: Initial droplet size in terms of pixel number

D^t_{ij} : Diffusive transport due to turbulent fluctuations

D^ν_{ij} : Viscous diffusive transport

D_{max} : Maximum stable droplet diameter $[m]$

E : Voltage obtained from CTA measurements $[V]$

ϵ_{ij} : Viscous dissipation of Reynolds stresses

f : Frequency $[Hz]$

k : Turbulent kinetic energy $[m^2/s^2]$

L : Nozzle length $[m]$

L_{11} : Longitudinal length scale $[m]$

L_{22} : Transverse length scale $[m]$

L_{int} : Integral length scale $[s]$

L_{ij} : Local change of $\overline{u_i u_j}$ in time

M	: Mesh (winglet) size $[m]$
n	: CTA calibration fit constant
n	: Sample size
P	: Pressure $[Pa]$
P_{exp}	: Estimated probability obtained from experiments
P_{ij}	: Production of Reynolds Stresses
P_{wilson}	: Wilson score interval
Πij	: Pressure-strain gradient correlation
$R(\tau)$	: Z-value
Re_L	: Integral length scale Reynods Number $[s]$
Re_λ	: Taylor Reynolds number $Re_\lambda = \frac{k^{0.5} * \lambda_g}{\nu}$
Ro	: Rossby Number $Ro = \frac{\langle U \rangle}{\Omega M}$
S^*	: Mean strain parameter (rapidity) $[s^{-1}]$
t	: Time $[s]$
T	: Integral time scale $[s]$
τ	: Time lag $[s]$
V	: Velocity $[m/s]$
μ_1	: Ratio of longitudinal Reynolds stresses
μ_2	: Ratio of transverse Reynolds stresses
$\overline{U}$	: Mean Velocity $[m/s]$
Z	: Z-value

1. INTRODUCTION

Droplet breakup mechanisms are fundamental to numerous engineering applications including fuel injection systems, spray cooling, pharmaceutical processing, and environmental dispersions. These mechanisms govern the atomization process, directly influencing combustion efficiency, heat transfer rates, and dispersion characteristics in various industrial systems. While the behavior of droplets under uniform flow conditions has been extensively documented, their response to turbulent environments—particularly anisotropic turbulence—remains poorly understood despite its prevalence in real-world applications.

This chapter provides a comprehensive review of the existing literature on aerodynamic droplet breakup, outlining the fundamental mechanisms, classification of breakup regimes, and the key parameters influencing the process. It then presents relevant studies involving active grid systems, emphasizing their role in turbulence generation and control. In addition, the chapter highlights the current gaps in the literature—particularly concerning droplet breakup under anisotropic turbulent conditions and identifies the open research questions that motivate the present study. Following this, the chapter introduces the central hypothesis, stating the primary objective of the research. Finally, the overall methodology employed to investigate the influence of turbulent flow characteristics on droplet atomization is outlined, establishing the framework for the subsequent experimental and analytical work.

1.1 Aerodynamic Droplet Breakup

The study of droplet dispersion holds significant importance across various fields, including combustion, spray technologies (e.g., surface coatings and agricultural sprays), fuel injection systems in jet and rocket engines, and pharmaceutical applications such

as inhalers. Many of these applications require efficient droplet breakup mechanisms, which are typically governed by the interaction between the liquid and gas phases. The atomization process—the disintegration of a bulk liquid into smaller droplets—occurs in two main stages: primary and secondary atomization.

- Primary atomization refers to the initial breakup of the liquid mass, typically occurring at the tip of injectors or nozzles, where hydrodynamic instabilities and velocity gradients cause the liquid to form ligaments and large droplets.

- Secondary atomization involves the further fragmentation of these droplets, primarily driven by aerodynamic forces arising from the relative velocity between the droplet and surrounding gas phase [3, 4].

In accelerating flows, aerodynamic droplet breakup becomes significant when a substantial relative velocity develops between the liquid and gas phases. This condition can be achieved by generating a uniform turbulent jet, for instance, by passing the flow through a contraction or nozzle, and introducing droplets at the nozzle exit. While several experimental methods—such as shock tubes, drop towers, and hybrid techniques—exist for studying droplet breakup, the present study focuses on the breakup behavior of droplets in a turbulent jet generated by the combination of an active grid and an axisymmetric nozzle.

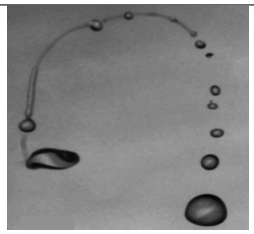
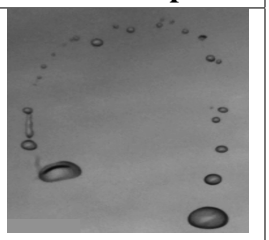
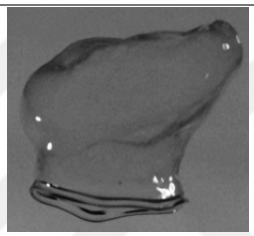
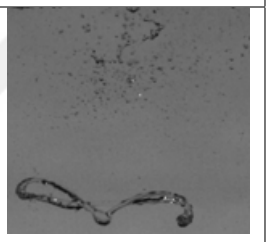
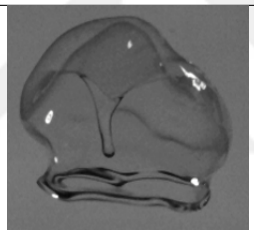
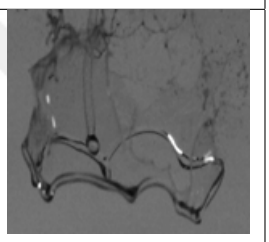
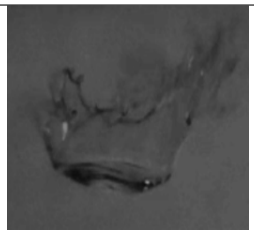
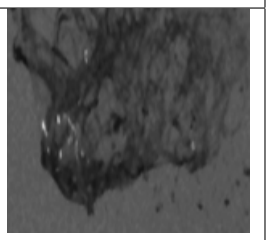
The morphology of droplet breakup is typically classified into five distinct regimes, each depending on the magnitude of the relative velocity between the fluids. These regimes are characterized by the dimensionless We. [4, 1], defined as:

$$We = \frac{\rho_g {U_r}^2 d_0}{\sigma} \tag{1.1}$$

As the relative velocity ${U_r}^2$ between two phases increases, We increases, changing the breakup morphology along with it. Following the work of Pilch and Erdman [1], the

breakup morphologies are as follows:

Table 1.1: *Breakup morphologies and their respective We ranges[1] with the addition of experimental visuals of the present study.*

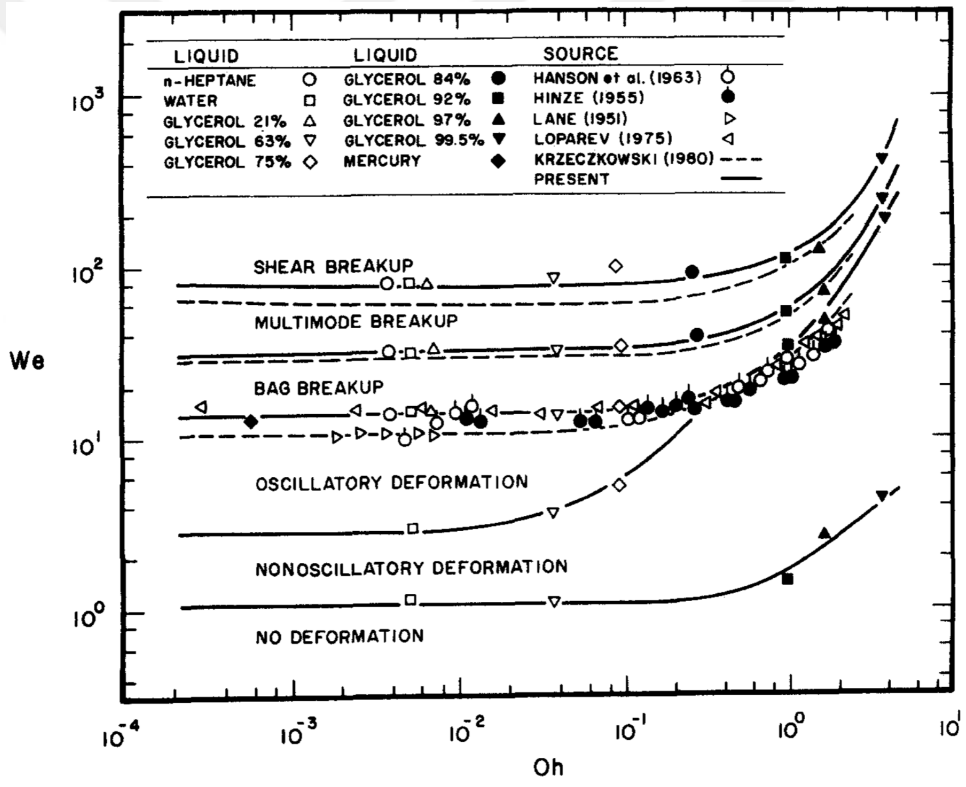
Morphology	We Range	Deformation	Breakup
Vibrational Breakup	$We \leq 12$		
Bag	$12 < We \leq 50$		
Bag and stamen	$50 < We \leq 100$		
Sheet Stripping	$100 < We \leq 350$		
Catastrophic	$We > 350$	None	None

Although We is a key parameter for characterizing droplet breakup, it does not account for the effects of viscosity and turbulence, which tend to resist deformation within the droplet. To incorporate the influence of viscosity, the Ohnesorge number is used. It represents the ratio of viscous forces to surface tension forces, providing a more complete picture of the forces acting on the droplet during breakup.

$$Oh = \frac{\mu_d}{\sqrt{\rho_d \sigma d_0}} \tag{1.2}$$

An increase in Oh represents a lower likelihood of droplet deformation. It is a crucial parameter to define the transition between breakup morphologies as it determines whether the droplet can fragment or not for a flow with a specific We. Considering that there is a limit for the transition between each breakup morphology , a critical We (We_{crit}) is defined for each morphology. The transition map can be seen below in Figure 1.1.

Figure 1.1: *Transition map of breakup morphologies. [2]*



Several studies have published varying critical We for transition between morphologies which is an indication that the transitions may exist in over a small range [3]. Although Oh effects the critical We, it is reported that the values of (We_{crit}) remain the same for $Oh < 0.01$ [2]. Considering the Oh number is below the specified limit in this

study, $Oh \sim 0.0023$, the previously given limits on Table 1 can be considered valid.

We in this study is estimated to be $10 \leq We \leq 170$, thus the breakup morphology is expected to be bag or bag-and-stamen. Yet, the given ranges are the result of a droplet exposed to uniform stream of air, which will not be the case in this study: The droplets are exposed to non-uniform, turbulent flow of air which may result in hybrid morphologies.

Intuitively, droplet breakup in turbulent flows is governed by the intensity, or more precisely, the energy content of the turbulent eddies. As a result, the breakup mechanism varies depending on the range of eddy sizes and their kinetic energy present in the turbulent flow. A droplet immersed in such a flow will interact with large energy-containing eddies, intermediate eddies in the inertial subrange, and small-scale eddies in the viscous range responsible for turbulent kinetic energy dissipation.

It is important to note that an eddy, or a vortex, is a localized region of velocity and pressure fluctuations that produces strain and shear rates—local velocity gradients that can distort a droplet. When a droplet is exposed to these variations, it undergoes deformation, which may lead to instability and eventual breakup.

Hinze argued that eddies with length scales comparable to the droplet diameter generate the most significant hydrodynamic stresses. These eddies induce larger pressure fluctuations across the droplet than smaller-scale eddies [5]. Based on this observation, he proposed a criterion for breakup wherein the critical We, originally based on relative velocity, is redefined in terms of the turbulent energy content of the eddies interacting with the droplet.

$$We_{crit} = \frac{\rho_g \overline{v^2} D_{\max}}{\sigma} \tag{1.3}$$

where ρ_c is density of the continuous fluid, $\overline{v^2}$ is the mean of the squared velocity differences across maximum stable droplet diameter, $D_{\max}$, and σ is the surface tension of the fluid. Hinze continues his work by assuming that the turbulence is Homogeneous

Isotropic Turbulence (HIT), and the majority of the kinetic energy lies within where the Kolmogorov power law is valid, i.e. the inertial subrange, which yields the relation

$$\overline{v^2} = C_1(\varepsilon D)^{\frac{2}{3}} \tag{1.4}$$

where $C_1 \approx 2.0$, and ε is the dissipation rate of turbulence. This equation suggests that the intensity of the velocity fluctuations between two points that are separated by the distance D, the droplet diameter, is of the order of $(\varepsilon D)^{2/3}$, consistent with the Kolmogorov scaling for eddies of size D. Hereafter, it is possible to calculate the maximum stable droplet diameter by plugging equation (1.4) to (1.3) results in,

$$\frac{\rho_g D_{\max}}{\sigma} C_1 \left(\epsilon D_{\max}\right)^{2/3} = \text{const.} \tag{1.5}$$

Manipulating this equation will give the final form of Hinze's scaling law:

$$D_{\max} \approx C \left(\frac{\rho_c}{\sigma}\right)^{-\frac{3}{5}} \varepsilon^{-\frac{2}{5}}. \tag{1.6}$$

It is important to note that D_{max} represents the maximum stable droplet diameter in a turbulent flow and $C \approx 0.725$ is a constant. Droplets exceeding this diameter are likely to undergo deformation and breakup due to turbulent stresses. The stability of droplets in such flows is influenced by several parameters, including surface tension, continuous-phase fluid density, turbulent kinetic energy, and, as a consequence, turbulent dissipation rate. An increase in dissipation rate, typically associated with higher turbulence intensity or turbulent kinetic energy, enhances the ability of the flow to deform droplets.

Through experimental investigation and dimensional analysis, Hinze determined that droplet deformation in turbulence occurs when the critical We reaches approximately $We_{\text{crit}} \approx 1.18$. This value defines the threshold above which turbulent dynamic pressure

overcomes surface tension forces, initiating droplet breakup.

Subsequent researchers expanded on Hinze's framework. Krzeczkowski [6] and Hsiang [2] refined the regime map and developed correlations for droplet deformation times, contributing to a better understanding of breakup dynamics. Later, Pilch and Erdman [1] further classified the droplet breakup process into five distinct morphological regimes, based on We, and proposed empirical correlations for predicting breakup time, fragmentation velocity, and droplet size distributions associated with each regime.

Numerous studies include the modeling of the droplet breakup mechanism utilizing both experimental and numerical techniques to predict the deformation physics of the droplets undergoing aerodynamic forces [3, 4, 7]. Other works include investigations of droplet breakup in the subsonic and supersonic flows in which the contribution of instability physics, such as the Rayleigh-Taylor and Kelvin-Helmholtz instabilities involved in the breakup process are studied [8, 9, 10, 11]. Although the findings listed above are crucial for understanding and modeling the droplet disintegration process, a limited amount of literature is present on the direct effects of turbulence in the droplet breakup mechanisms [33]. Hinze's approach of critical We and maximum stable droplet diameter (Hinze Scale) within a turbulent HIT for predicting droplet breakup in turbulent fields has been used in many analysis [36]. Several experimental and numerical studies are available utilizing Hinze Scale and the effects of turbulence on breakup. However, the works are under the assumption of HIT [12, 13, 14, 15, 16].

According to Vankova et al., two regimes can be identified for the deformation of a droplet: the "turbulent inertial" and the "turbulent viscous" regimes [15]. The turbulent inertial regime consists of eddies that are smaller than the droplet and induce deformation through applying hydrodynamic pressure to the surface of the drop. The turbulent viscous regime, on the other hand, has eddies larger than the droplet which allows viscous shear stress to deform the droplet. Unlike Hinze's work, which proposed that the forces exerted

by eddies of similar size to the droplet are the most effective in atomization, Vankova et al. consider a broader range of turbulent motions. This approach thus extends Hinze's model by incorporating the contributions of both small eddies (which cause atomization through high shear) and larger eddies (which deform droplets primarily through viscous shear stresses). The atomization experiments confirm that the combined influence of large and small eddies drives deviations in the breakup dynamics. As the process unfolds, eddies of different scales successively assume prominence, each playing a critical role when conditions become favorable.

Several models exist to determine the deformation of a droplet. One such model is the Taylor Analogy Breakup (TAB) model which is based on the analogy between a spring-mass system and oscillating and distorting droplet [17]. A review and comparison of models can be accessed through the work of Lasheras [18]. Although the modeling of droplet breakup is out of the scope of this work, there is one particular work that has a crucial finding. Many of the developed breakup models use the assumption of eddies, having a size larger than the droplet, have minimal effect on deformation other than transporting the fluid particles. The findings of Ronie and Bengt Andersson contradict this assumption [12]. In their work, it is stated that the droplets in a turbulent flow are exceptionally deformed before the actual breakup occurs. It is observed that the deformation takes place in the range of milliseconds which suggests that large, energy-containing eddies are responsible for the breakup. Therefore, they implement this knowledge in their model and discover that eddies of similar size and three times larger than a droplet will contribute to the breakup process. This behavior is also evident in the experimental footage, where the droplet undergoes non-uniform deformation, leading to the formation of multiple bag breakups. Such breakups are likely induced by local pressure fluctuations generated by the influence of large eddies.

1.2 Numerical Modeling of Turbulence

The design of an experimental setup requires prior knowledge to anticipate potential outcomes and assess the influence of design choices, thereby minimizing time and reducing costs. To this end, several analyses were conducted to guide the decision-making process, with the experimental setup ultimately manufactured based on chosen turbulence models to accurately predict the flow dynamics whilst running the simulations.

Even though the basic utilization of fluid mechanics dates to the Ancient Greeks, the discovery of theories and concepts still utilized up to our modern times were made in the 17th and 18th centuries. One of the most well-known and groundbreaking development was the Navier-Stokes equations describing the motion of both Newtonian and Non-Newtonian fluids. The Navier-Stokes equations of momentum allow the flow characteristics such as pressure, velocity, density, gravitational acceleration and viscosity to be related and a way of determining how fluids behave with given boundary and initial conditions. However, the non-linear and complex nature of these relations has caused problems in solving them analytically; therefore, computational methods, such as the finite volume method, are developed to model and numerically solve these equations. Although the Navier-Stokes equations can be directly solved using appropriate numerical schemes with minimal discretization errors, the spatial and temporal resolutions required to capture the turbulence scales in the energy cascade, an idea proposed by Richardson [19], is tremendously high. Henceforth, due to the computational cost of Direct Numerical Simulation (DNS), turbulence models are the preferred method for approximating the flow properties. The introduction of statistics to the Navier-Stokes equations by Osborne Reynolds [20] has led to a breakthrough in terms of turbulence modeling. His approach was to decompose the field of flow into its mean and fluctuating parts, resulting in an additional term called Reynolds stresses. Although this method eliminated the need to directly solve the cumbersome Navier-Stokes equations, the addition of additional unknowns due

to Reynolds stresses created a problem known as the 'closure problem'. Many attempts were made to approximate and model the Reynolds stresses utilizing an artificial variable called eddy viscosity, which accounts for any momentum effects produced by turbulent eddies by relating mean strain rate utilizing the Boussinesq hypothesis given by

$$\tau_{ij} = \langle u_i u_j \rangle = \frac{2}{3} k \delta_{ij} - 2\mu_t \langle S_{ij} \rangle \tag{1.7}$$

in which k represents Turbulent Kinetic Energy (TKE) (trace of Reynolds stress tensor, $k = 0.5\langle u_i u_i \rangle$), μ_t represents eddy viscosity while $\langle S_{ij} \rangle$ is the ensemble average of the strain rate. The study was conducted under the assumption of statistically stationary turbulence; therefore, the time-averaged strain rate tensor was employed as a substitute for ensemble averaging.

Many turbulence models, particularly algebraic models, have been proposed to approximate the eddy-viscosity term through linear relationships, often based on Prandtl mixing length theory [21]. This theory assumes that eddy size reduces as the flow approaches the wall, providing a simple means of estimating turbulence effects. Building upon this, Van Driest introduced a damping function to account for the influence of viscosity near the wall region [22].

Well-known examples of models employing such algebraic formulations include those of Cebeci–Smith and Baldwin–Lomax [23, 24]. While these models provide a form of closure, their reliance solely on wall distance (through fixed mixing lengths) limits their ability to capture the history-dependent behavior of turbulence, specifically the transport of turbulent energy through convection and diffusion. In other words, these models cannot adequately represent the energy cascade from large energy-containing eddies to smaller dissipative ones.

To address these limitations, models using transport equations for turbulent kinetic energy and its dissipation rate were developed to better estimate the eddy viscosity. Among the most widely used are the two-equation models, including the k–ϵ model by Jones and Launder and the k–ω model by Wilcox [25, 26]. Over time, both models have been refined with improved wall treatments and damping functions. For instance, Shih et al. introduced the realizable k–ϵ model, and Menter developed the Shear Stress Transport (SST) k–ω model, which is particularly effective in flows with strong adverse pressure gradients and anisotropic effects [27, 28].

The Boussinesq hypothesis assumes that the turbulent viscosity is isotropic, which allows the Reynolds stress tensor to be modeled as being linearly proportional to the mean strain rate. While this approximation works well for many flows, it limits the ability of eddy-viscosity models to accurately capture the behavior of flows with strong anisotropy or high strain rates. To overcome this limitation, more advanced constitutive relations,such as quadratic and cubic non-linear eddy-viscosity models have been proposed. These models incorporate non-linear relationships between the Reynolds stress tensor and the mean strain rate tensor, enabling improved predictions for highly anisotropic turbulence. [29, 30, 31] (see [32] for a more in-depth examination of nonlinear eddy viscosity models). Nevertheless, although the addition of nonlinearity to the eddy viscosity models has been proven successful in predicting flows with large shear and strain rates, these models tend to be flawed for rapidly contracting and expanding flows. Thus, utilizing models directly solving transport equations for each Reynolds stress provides significantly improved results: Such models are called Reynolds Stress Transport (RST), also known as RSM [33]. Considering the fact that Reynolds Stress Models are individually solving Reynolds stresses, the model can naturally depict the effects of anisotropy, rotation, and large strain rates. Though, compared to two-equation models, the Reynolds stress transport equation introduces four additional terms to be modeled; therefore, RST

models are considerably complex compared to their counterparts and open to modeling errors. These terms are turbulent diffusive transport (two terms), pressure strain, and turbulent dissipation.

$$\underbrace{\frac{\partial \overline{u_i u_j}}{\partial t}}_{L_{ij}} + \underbrace{\overline{U_k}\frac{\partial \overline{u_i u_j}}{\partial x_k}}_{C_{ij}} = \underbrace{-\left(\overline{u_j u_k}\frac{\partial \overline{U_i}}{\partial x_k} + \overline{u_i u_k}\frac{\partial \overline{U_j}}{\partial x_k}\right)}_{P_{ij}} - \underbrace{\frac{\partial \overline{u_i u_j u_k}}{\partial x_k}}_{D^t_{ij}}$$
$$\underbrace{-\frac{1}{\rho}\left(\overline{u_j\frac{\partial p}{\partial x_i}} + \overline{u_i\frac{\partial p}{\partial x_j}}\right)}_{\Pi_{ij}} \underbrace{-2\nu\overline{\frac{\partial u_i}{\partial x_k}\frac{\partial u_j}{\partial x_k}}}_{\overline{\varepsilon_{ij}}} + \underbrace{\nu\frac{\partial^2 \overline{u_i u_j}}{\partial x_k \partial x_k}}_{D^\nu_{ij}} \quad (25) \quad (1.8)$$

The terms diffusive transport due to turbulent fluctuations, pressure-strain, and viscous dissipation of Reynolds stress, D^t_{ij}, Π_{ij}, and ϵ_{ij} respectively require modeling [34]. One of the most challenging terms to model is the pressure-strain relationship which represents the effect of fluctuating pressure on turbulent stresses. It is crucial to model the effect of pressure fluctuations for a turbulent flow as pressure is responsible for redistribution of energy among the components of Reynolds stresses. Generally, pressure-strain models consist of 'slow' and 'rapid' terms, each employing their own effects depending on the straining action of the flow. The 'slow' term, being a function of fluctuating strain and rotation rate, is responsible for equipartitioning of the turbulent stresses, or the return-to-isotropy of an anisotropic turbulent field. Meanwhile, the 'rapid' term is accountable for the production of turbulence through the interaction of mean and fluctuating strain and rotation rates.

A linear pressure-strain relationship was developed by Gibson and Launder [35] to account for the effects of turbulence on the atmospheric boundary layer. Another model, the quadratic pressure-strain model, was established by Speziale, Sarka, and Gatski which was proven to be superior compared to other available models in terms of flows with

extreme strain rates as it was modeled in a way to be consistent with Rapid Distortion Theory (RDT) [33].

Given their capability to more accurately predict highly anisotropic flows, in which Reynolds stresses vary substantially in space and time, non-linear eddy-viscosity models present a more realistic framework for capturing the complex turbulence dynamics relevant to droplet atomization. These models offer improved resolution of the pressure and velocity fields, which are critical in governing droplet deformation and breakup mechanisms. Therefore, employing such complex turbulence models can contribute to a more accurate approximation of atomization characteristics by providing a refined representation of the turbulent flow field.

1.2.1 Rapid Distortion Theory (RDT)

In the design phase, numerical models were employed to guide the development of the nozzle geometry and flow characteristics. In contrast, during the analysis phase, analytical calculations were conducted to estimate the turbulence properties in accordance with RDT, thereby enabling the processing and interpretation of the hot-wire experimental data. The foundation of RDT is built upon an extensive history of experimental investigations and mathematical developments, a concise overview of which is presented in this section.

The rapid distortion theory, proposed by Ribner and Tucker [36] and independently by Batchelor and Proudman [37], is a linear theory that is based on the works of Prandtl [38] and Taylor [39]. While performing his experiments to obtain a steady air stream inside a wind tunnel, Prandtl notices that the streamwise vorticity component is amplified while the lateral vorticity components of the flow are reduced. Hence, Prandtl considers vorticity to be the primary variable in a turbulent follow, and considering the conservation of angular momentum, he deduces that the longitudinal velocity component

should decrease while the lateral velocity components are intensified on a single vortex filament. In other words, the vortex filaments are aligned in the direction of the mean strain rate: This phenomenon is carefully examined in the astonishing work of Mugundhan et al. in which the alignment of vortical structures is studied both experimentally and numerically [40]. Taylor, continuing Prandtl's work, studied the effect of contraction while assuming that turbulence is a continuous distribution of vorticity. Utilizing Fourier decomposition, the mathematical relations put forward by Taylor are integrated throughout all wavenumbers to approximate the effect of a contraction on a turbulent flow. Since several assumptions are made throughout the derivation of RDT, recent studies suggest that it can be misleading when used to develop contemporary models aimed at accurately capturing anisotropy effects in contracting flows. These assumptions may oversimplify the complex nature of turbulence evolution. Therefore, care must be taken when utilizing RDT based relationships, as the resulting predictions may not fully reflect the actual behavior of anisotropic turbulence, potentially leading to inaccurate conclusions depending on the rapidity of the applied strain. The dynamics of axisymmetric turbulence is thoroughly investigated in the work of Ö. Ertunç which covers the comparison of models with experimental results [41]. The above mentioned assumptions are as follows;

- Rapid distortion: A key assumption is made which assumes that the relative motion between fluid particles is large enough that the effect of turbulence is negligible, meaning that the mean strain rate dominates.
- Initially homogeneous and isotropic turbulence
- Incompressible flow
- Inviscid flow

While evaluating the accuracy of RDT, Uberoi observed that for nozzles with low contraction ratios, the longitudinal Reynolds stress decreases steadily along the nozzle

and closely follows RDT predictions. However, when the contraction ratio C exceeds 9, an equipartition of Reynolds stresses emerges an effect commonly interpreted as the return to isotropy during the contraction phase [42, 43, 44, 45, 46, 47].

More recent findings by Ertunç and Durst challenge this interpretation as the researchers have come across such phenomenon while utilizing active grid for turbulence generation. They argue that the observed return to isotropy is not a physical phenomenon, but rather a consequence of experimental contamination, including X-wire probe resolution limits, electronic noise, and mass flow rate fluctuations [46]. When these factors are properly accounted for and eliminated, the longitudinal and lateral Reynolds stresses were found to evolve consistently with RDT, with the former decreasing and the latter increasing steadily [40, 46].

Since many Reynolds Averaged Navier-Stokes (RANS) turbulence models incorporate empirical return-to-isotropy terms, their predictions become unreliable in flows with strong mean strain rates, leading to inaccuracies in simulating such flows.

Given the assumptions underlying RDT—particularly its reliance on linear distortion, neglect of nonlinear interactions, and the requirement for initially HIT its predictions are susceptible to both under-prediction and over-prediction of Reynolds stresses. Therefore, further experimental validation is needed.

To address this, a controlled experimental setup is proposed in which well-characterized turbulence is generated using an active grid and subsequently subjected to mean strain via an axisymmetric contracting nozzle. This configuration enables the introduction of anisotropy into the flow in a systematic and repeatable manner. The resulting turbulence lies within the left side of the Lumley's triangle, towards the 2-component isotropic limit, in which the turbulence is stated to be in the shape of an oblate spheroid, or a pancake [19, 41]. The resulting droplet dispersion characteristics will be investigated using high-speed imaging, with the objective of examining turbulence–particle interactions under

controlled anisotropic conditions which is estimated using RDT. It is important to emphasize, however, that the validity of the return-to-isotropy hypothesis remains an open question, and that RDT, due to its inherent simplifications, may not fully capture the complexity of strained turbulent flows in such scenarios. Therefore, caution must be exercised when interpreting the results and applying these theoretical models, as their assumptions may limit their applicability in accurately describing the observed phenomena.

1.3 Active Grid Generated Turbulence

Before the development of active grids, passive grids were commonly used to generate HIT. However, these setups produced flows with relatively low turbulent Reynolds numbers, $50 \leq Re_\lambda \leq 100$ [48], limiting their ability to replicate natural or industrial turbulent phenomena. To study HIT at higher Reynolds numbers, a more advanced approach was required—particularly to better simulate real-world processes such as atmospheric flows.

In response to this need, Makita and Sassa, pioneers of the active grid, introduced a novel system that used electrically driven square winglets mounted on rotating shafts. These winglets oscillated in controlled patterns, enabling the generation of turbulence with significantly higher Reynolds numbers up to ($Re_\lambda = 400$) [49] This technique not only increased the turbulent kinetic energy but also extended the integral length scale, producing turbulence more representative of conditions found in environmental and industrial flows.

Active grids also played a crucial role in experimentally validating Kolmogorov's similarity hypotheses. The first hypothesis states that, at sufficiently high Reynolds numbers, the transfer of energy from large eddies to small dissipative eddies is locally isotropic and homogeneous [50]. The second hypothesis describes the existence of an inertial

subrange—a scale region between the energy-containing eddies and the dissipative eddies—where the energy spectrum follows the famous $\kappa^{-5/3}$ scaling law; with κ representing the wavenumber.

The work of Mydlarski and Warhaft provided critical insights into these hypotheses. By designing their own active grid and generating high-Reynolds-number turbulence, they demonstrated that achieving the $-5/3$ slope in the power spectral density—a hallmark of the inertial subrange, requires turbulence at around $Re_\lambda = 10^4$ [48]. Their findings highlighted the importance of turbulence strength in reproducing the energy cascade predicted by Kolmogorov. However, their results suggest that $Re_\lambda > 200$ produces a well-developed scaling region with an exponent close to $5/3$. It has also been noted that different modes of turbulence initiation are capable of producing the characteristic $5/3$ slope even at relatively low Re_λ. Consequently, a systematic examination of various turbulence generation methods is required to determine whether true universality can indeed be achieved.

Several studies have investigated the influence of initial conditions and motion protocols on turbulence generated by active grids. Larssen and Devenport, for example, employed an active grid with three distinct motion protocols to examine how the resulting turbulence depends on flow velocity, protocol type, and wing rotation rate [51, 52]. Their experimental results highlight the importance of both the Rossby number and grid Reynolds number, showing that increases in these parameters lead to higher turbulence intensity, larger Taylor microscales, elevated dissipation rates, and higher Taylor Reynolds numbers.

Additionally, their findings indicate that as the mean rotation rate of the winglets decreases, the resulting turbulence exhibits larger flow structures—an expected outcome, as the wings block more of the mean flow for longer durations, promoting the formation of larger eddies.

A complementary study by Hearst and Lavoie further emphasizes the influence of the Rossby number, grid Reynolds number, and winglet geometry in shaping the characteristics of active grid–generated turbulence [53].

Beyond characterizing turbulence, some researchers have used active grids to tailor specific turbulence conditions. Notable examples include the works of Skeledzic et al. [54] and Cekli and Water [55], who adjusted grid parameters to generate desired turbulent outputs.

In the spirit of Comte-Bellot and Corrsin's foundational work [56], Kang et al. employed an active grid to generate turbulence at high Reynolds numbers, $Re_\lambda \approx 720$, and compared the experimental results with LES [57]. Their study evaluated the performance of various subgrid-scale models—including Smagorinsky, dynamic Smagorinsky, and nonlinear formulations—in reproducing the observed turbulence characteristics, thereby providing critical validation for LES methodologies. Furthermore, the notable work of Akardere et al. [58, 59], which explores the influence of winglet geometries and motion protocols through comprehensive LES analyses, demonstrated that by optimizing active grid parameters and wing configurations, it is possible to tailor turbulence characteristics, such as turbulence intensity and homogeneity, to meet specific experimental requirements .

It is important to note that the majority of studies involving active grids aim to generate HIT, primarily to investigate the resulting spectral characteristics and turbulent structures under idealized conditions. In contrast, the present study does not prioritize the production of HIT. Instead, the turbulence generated by the active grid is immediately subjected to axisymmetric contraction. As previously discussed, the flow is intentionally designed to be as anisotropic as possible, since the objective is to study turbulence under mean strain. Moreover, for RDT to remain valid, it is essential that the generated turbulence be strained promptly, before significant non-linear interactions develop.

In designing the active grid used in this work, guidance was drawn from the influential studies of Makita, Hearst, and Mydlarski, whose contributions have been foundational in the development and application of active grid technology [49, 53, 60].

1.4 Open Fields in the Literature

While limited research has been conducted on droplet dispersion in turbulent flows, most studies rely on the assumption of HIT, an idealization that rarely reflects real world conditions. Additionally, in many cases, the objective of these studies does not specifically address the effects of turbulence on atomization dynamics.

The recent work of Coşar [61] on droplet atomization in HIT argues that the parameters included in Hinze's scaling law are insufficient to fully characterize the influence of turbulence on droplet breakup. The study reports the occurrence of various breakup morphologies within statistically identical turbulence fields, indicating that the current model lacks the necessary complexity to account for observed behaviors. As a result, the study suggests that Hinze's model should be systematically revisited to identify and evaluate the key turbulence parameters influencing droplet breakup. These parameters include the Reynolds stresses, integral and inertial length scales, as well as their associated time scales.

Since this study employs an active grid, which enables the controlled tailoring of turbulence characteristics, it becomes possible to implement various combinations of motion protocols, including those developed by Akardere et al., to investigate how changes in turbulence influence atomization dynamics. This powerful capability allows for systematic exploration of different turbulent conditions, potentially leading to the development of a comprehensive map that illustrates the relationship between turbulence parameters, such as intensity, integral length scale, and anisotropy, and droplet atomization behavior.

The current lack of experimental data under anisotropic turbulence conditions

highlights the need for further investigation into how varying turbulent flow parameters affect droplet disintegration. Understanding these effects is essential for accurately predicting breakup behavior in realistic flow environments.

1.5 Hypothesis of the Study

A variety of complex dynamics influence droplet behavior in anisotropic turbulent fields, rendering Hinze's scaling law insufficient for accurately predicting the maximum stable droplet diameter under such conditions. It is hypothesized that introducing controlled variations in the turbulence structure—through adjustments to the active grid protocols alters the distribution and interaction of turbulent length and time scales, thereby affecting droplet atomization in terms of breakup probability and atomization intensity. This study aims to demonstrate that additional turbulence characteristics, such as Reynold's stresses, integral length and time scales, beyond those considered in Hinze's law, play a critical role in droplet deformation and breakup, challenging the adequacy of traditional assumptions made for HIT.

1.6 Objectives of the Study

The objectives of the present study can be listed as follows:

- The main objective of this study is to experimentally investigate the breakup behavior of droplets in anisotropic turbulent flow fields generated by an axisymmetric contraction and modulated through the implementation of customized active grid protocols.
- Quantify turbulence characteristics such as turbulent kinetic energy, integral length scales, Taylor's turbulence scale, and anisotropy levels using hot-wire anemometry.
- Capture and statistically analyze droplet deformation and breakup events under

varying turbulent flow conditions.

- Evaluate the effect of different active grid protocols on turbulence structure and their subsequent influence on droplet breakup regimes.

1.7 Methodology

To commence the design of the active grid, turbulence quantities were required for deciding upon the size of the grid winglets. LES analysis of full active grid was planned using Siemens' STAR-CCM+ software to obtain the necessary turbulence data for initiating the calculations. However, the complete Computational Fluid Dynamics (CFD) analysis of the active grid system proved to be costly in terms of both computational resources and time. As a result, a simplified approach was adopted by conducting single-winglet simulations under varying inlet velocities and constant rotational speeds to approximate the turbulence characteristics.

The fluctuating velocity data obtained from the LES analysis were used to estimate key turbulence characteristics such as integral length scales, turbulence dissipation rate, and Reynolds stresses, under the assumption of HIT downstream of the active grid. This approach enabled the application of RDT to estimate the evolution of turbulence at the nozzle exit. In parallel, RST and LES simulations were carried out for the nozzle geometry to validate the RDT-based predictions and finalize necessary parameters required for nozzle design. The potential for droplet breakup was then evaluated using Hinze's scaling law.

Building upon the insights gained from the aforementioned simulations and theoretical analyses, an experimental setup was designed and fabricated. The setup consists of a fan, an active grid with independently rotating shafts, a contracting nozzle, and a

droplet generation system, all configured to be compatible with Particle Image Velocimetry (PIV) (not used in the present work), hot-wire anemometry, and high-speed imaging techniques.The high-speed images and hot-wire measurements obtained from the experiments were processed using custom-developed algorithms to identify potential patterns and correlations between droplet atomization behavior and the characteristics of the turbulent flow.

1.8 Structure of the Thesis

Chapter 2 presents the detailed design of the experimental system, covering the development of the active grid, motor assembly, diffuser, and nozzle. Each section highlights the design rationale, implementation steps, and technical considerations taken during the setup process.

Chapter 3 outlines the experimental procedures conducted in this study. It begins with the description of the active grid protocols implemented to control turbulence characteristics, followed by the methodology for pressure measurements. The subsequent section focuses on droplet atomization experiments, including the methods for droplet generation and visualization. This chapter also details the hot-wire anemometry measurements, encompassing both the experimental procedures and the calibration of the hot-wire system.

Chapter 4 presents the results obtained from the experiments and is divided into three main sections. The first section focuses on the analysis of droplet breakup behavior. The second section addresses turbulence characterization and includes discussions on power spectral density analysis, autocorrelation of velocity signals, and an investigation into the applicability of Rapid Distortion Theory within the flow. The third section examines the influence of turbulence on droplet atomization and compares the present findings with existing knowledge in the literature.

Finally, Chapter 5 concludes the thesis by summarizing the main findings, highlighting the contributions of the study, and offering suggestions for future work.

2. WIND TUNNEL DESIGN FOR DROPLET ATOMIZATION UNDER ANISOTROPIC TURBULENCE CONDITIONS

Various parametric numerical and analytical studies conducted beforehand have paved the way for the design and the manufacturing of the anisotropic wind tunnel. However, it is a known fact that theoretical applications, such as modelling in Star-CCM+ or developing algorithms in MATLAB, may not represent the reality of the experimental limitations. Hence, while making the final design and manufacturing decisions, several aspects were changed to stay within the budget and limit the mechanical stresses in the system.

In this chapter, the procedure for the design and manufacturing of the wind tunnel will be discussed. Several key parameters were considered, including the size, shape, and number of active grid winglets; the distance between the rows of shafts; the motion protocols for the shafts; and the shape, length, and contraction ratio of the nozzle. Most of these parameters were selected according to the present literature on active grid design and turbulence generation. It is important to note that many active grid related works are based on the generation of HIT, or on the real-life applications such as atmospheric boundary layers. Since this study primarily relies on the generation of anisotropic turbulence and does not deal with the delicate nature of producing HIT, the design choices were made accordingly. The design is similar to the active grid designed by Makita and Sassa [49].

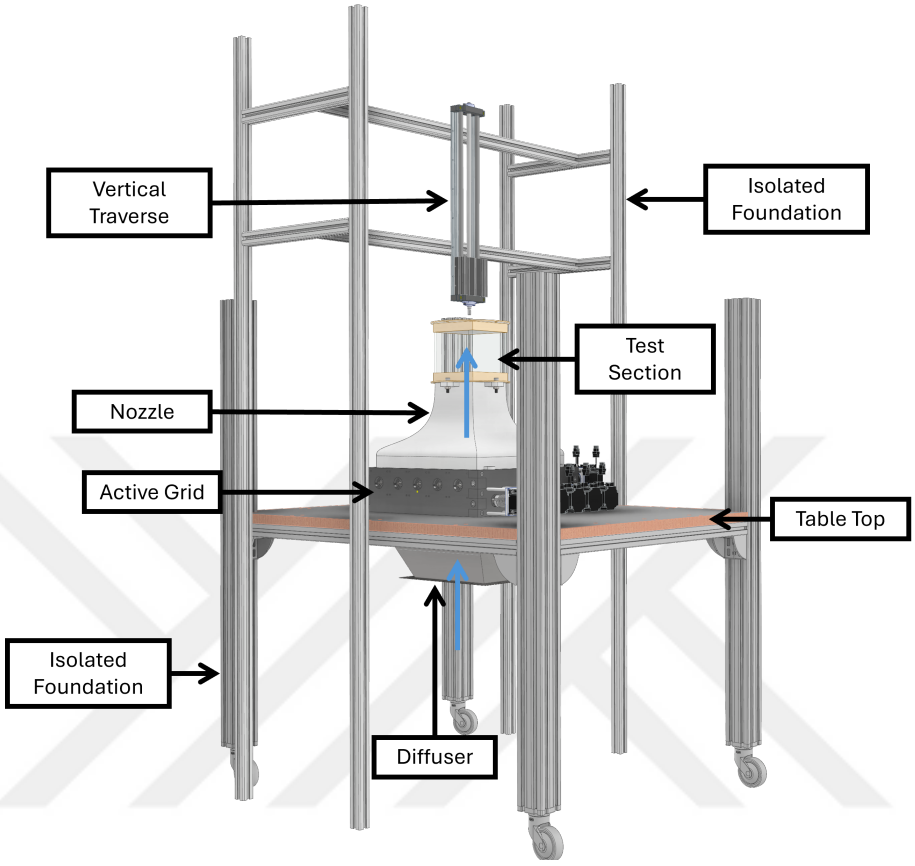
2.1 Design of the Anisotropic Wind Tunnel

The design must incorporate all preliminary insights obtained from numerical simulations and analytical calculations, ensuring that the system meets the specific requirements of the experimental objectives. It should enable the controlled generation of desired turbulence characteristics through the application of active grid protocols, followed by the

immediate straining of the resulting turbulent field via an axisymmetric nozzle. Additionally, the setup must facilitate high-speed imaging of the droplet atomization process, as well as allow for the integration of hot-wire anemometry to capture detailed turbulence measurements. Particular attention must be given to the structural robustness of both the active grid and the nozzle. The active grid must withstand abrupt dynamic loads generated by the rapid motion of individual shafts under various motion protocols, while the nozzle must endure elevated flow rates that may induce localized stress concentrations, posing a risk of structural failure.

Sigma aluminum profiles were selected for constructing the table because of their formability, lightweight structure, and structural resistance to bending moments. 90 by 90 mm sigma profiles were used as the legs of the table while 45 by 45 mm profiles acted as support structures for the active grid and its components. The tabletop was chosen to be 1.40 m by 1.29 m, and 30mm thick Marine plywood for its durability and water resistivity. Moreover, four 100mm diameter wheels with rubber linings were attached to the ends of the legs for allowing easy mobilization as the whole experimental setup weighs approximately 140 kg. The completed experimental setup can be seen in 2.1.

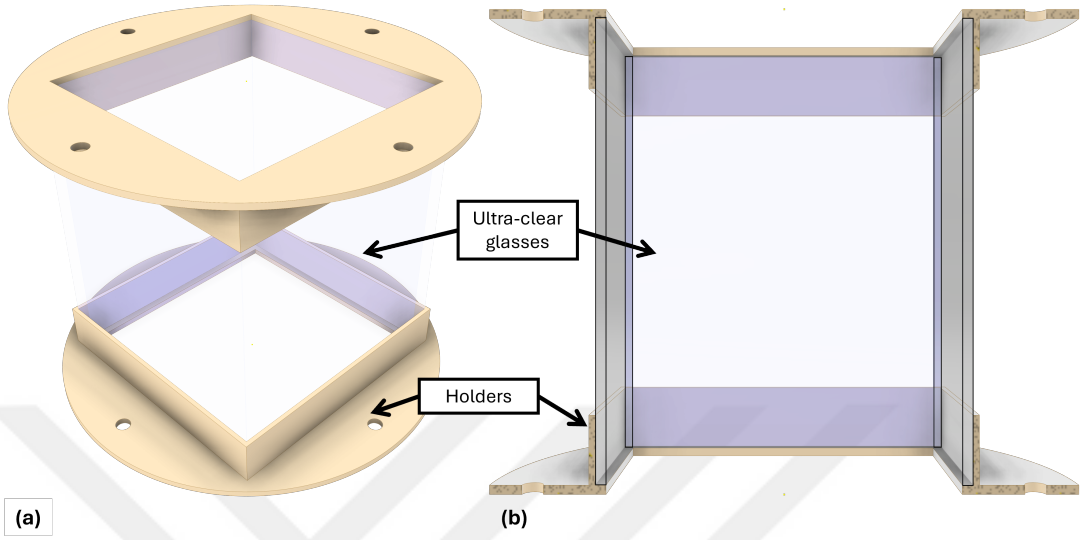
Figure 2.1: *The overall view of the designed experimental setup.*



Considering that the active grid operates under protocols involving abrupt accelerations, any lack of support at the table's foundation could result in oscillatory motion. To mitigate this, the table was designed for maximum rigidity, incorporating numerous connection components and intermediate reinforcements. Also, the wheels were specifically chosen with locking mechanisms to block potential movement.

To support the implementation of the hot-wire probe and the droplet injection mechanism, an independent foundation was constructed to isolate them from vibrations generated by the active grid. This isolation was critical to prevent disturbances in both hot-wire measurements and droplet generation.

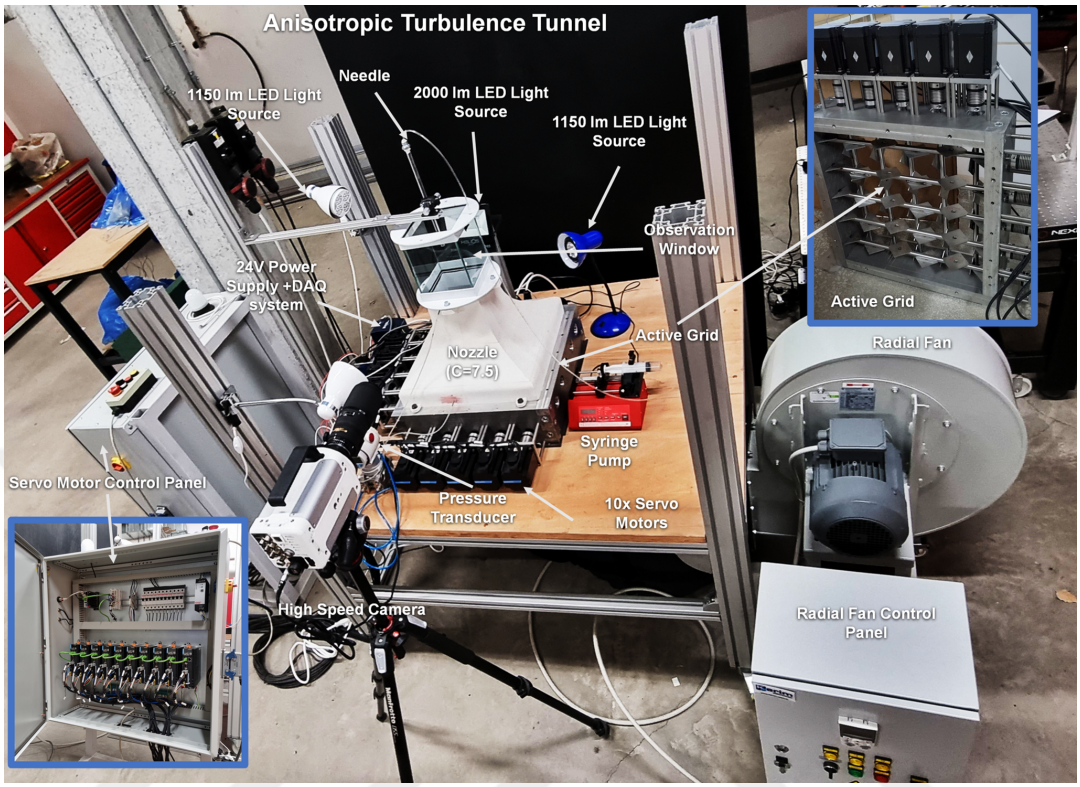
Figure 2.2: *Test section made from ultra-clear glasses and 2 holders for integration to the tip of the nozzle.(a) Isometric view, (b) cross-sectional view.*



A rectangular test section measuring 0.165 × 0.165 m in cross-section and 0.20 m in length was fabricated by bonding four 5 mm thick ultra-clear glass panels using aquarium-grade adhesive. A 0.20 m length allowed the flow to develop while the Ultra-clear glass was specifically selected for its superior optical properties, offering a transmittance of 91% and a reflectivity of only 8%. Minimizing reflectivity was essential for capturing high-quality footage using the high-speed camera. The designed test section can be seen in 2.2.

A radial fan equipped with a 4 kW motor was provided by Euroofan to meet the required mass flow rate within the defined total pressure range. Since the active grid obstructs approximately 85% of the flow area when fully closed, the fan was selected to deliver a volumetric flow rate of 3645 m^3/h at a total pressure of 2500 Pa, ensuring sufficient pressure head to prevent backflow. The finished setup can be seen in Figure 2.3.

Figure 2.3: *The bird eye view of the components of the setup.*

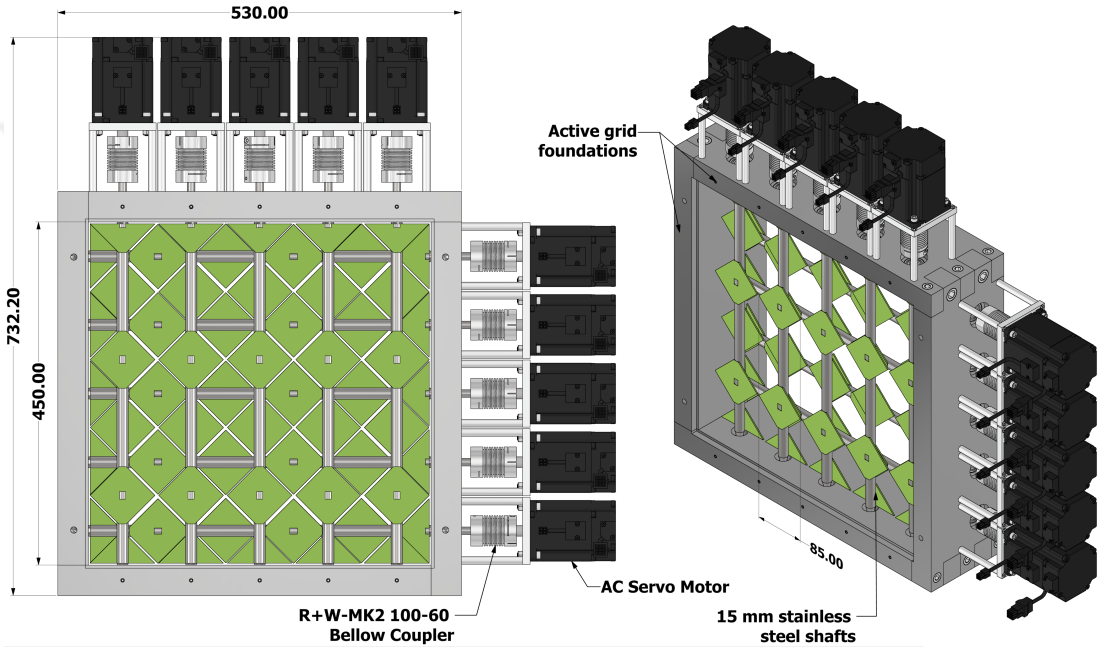


2.2 Active Grid Design

One of the crucial steps in designing a system is choosing appropriate material depending on the operational and environmental conditions. It was decided that the system would be exposed to distilled water and alcohol, or other fluids if necessary; therefore, the system had to be corrosion resistant. Moreover, since the planned motion protocols contained sudden accelerations and high rotational velocities, the system also had to be rigid and tough to prevent any damage to the components. For this reason, the foundation of the active grid was manufactured from Aluminum 6013 for its high strength, corrosion resistance and good formability. Furthermore, the shafts were manufactured with extra durable stainless steel 316L as the shafts are directly exposed to distilled water and

alcohol droplets. Corrosion resistance is specifically crucial as distilled water is highly corrosive since it lacks the dissolved ions, so it tends to bond with metal ions. As stated previously, the shafts must withstand abrupt rotational forces with minimal displacement to prevent contact with other components and to reduce fatigue, ensuring the longevity of the system. The active grid complex can be seen below on Figure 2.4.

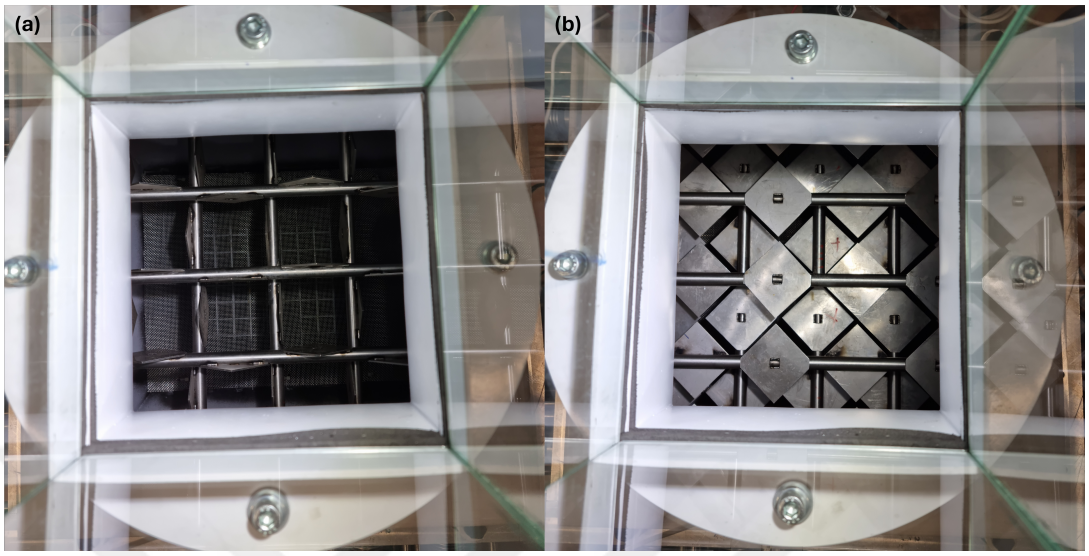
Figure 2.4: *Designed active grid. (a) Top view , (b) isometric view.*



The grid is 0.45 by 0.45 meters with 10 independent stainless-steel shafts with square winglets resulting in a mesh size of M = 0.085 m. Circular winglets with diameters of 0.085 m were also manufactured due to the increased effects on turbulent properties such as turbulence intensity [53, 58]; however, they were not utilized for the experiments as majority of the research on the active grid involves the use of square winglets. Subsequently, the dynamics of square winglets are better known compared to other geometries. The open and closed states of the grid can be seen on Figure 2.5.

The shafts are 15 mm in diameter at the middle and gradually decrease to 10mms at each side to match the bearing bore diameter. The shafts contain a longer 10 mm

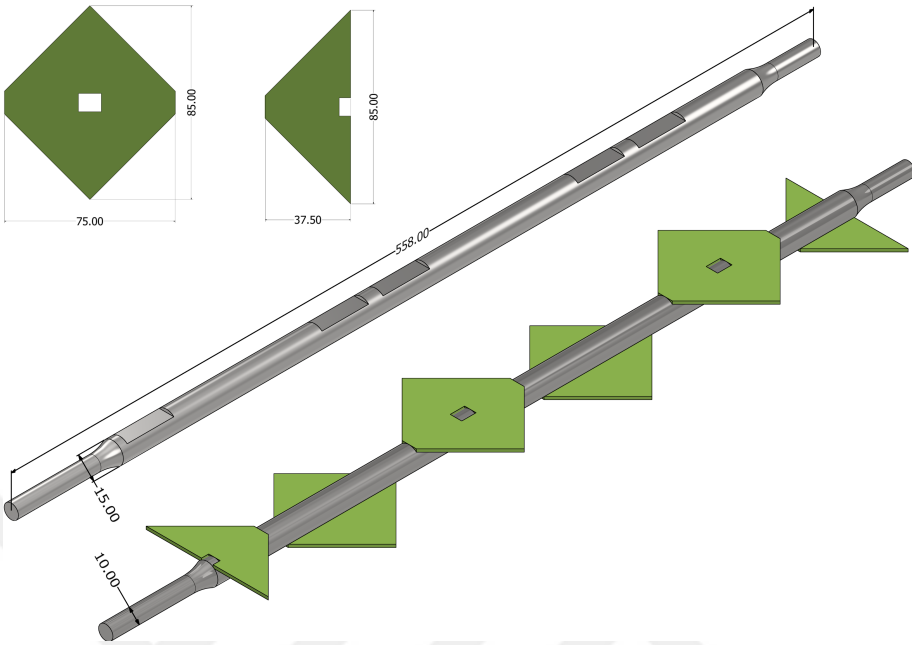
Figure 2.5: *The open and closed states of the grid. (a) Open grid , (b) closed grid.*



portion for creating a junction between the electric motors with the use of a coupler. The middle portion of the shafts are essentially thicker for creating proper seats for the winglets. The preferred method for attaching the winglets was laser welding to prevent distortions caused by heating of the material and ensure a safe connection for protocols requiring elevated torque levels. Each shaft contains four complete and two halved square winglets at the end of the shafts. There are available studies by Mydlarski and Warhaft [48] and Larssen and Devenport [52] on how static (attached to the walls of the grid) and rotating winglets near the grid boundary effects the boundary layer and the resulting turbulence. For our design, the half-winglets are attached to the shafts and offset by 2mm on either side. The rotating winglets at the grid boundaries could result in better turbulence characteristics as majority of the investigations emphasize on the effects of varying motion protocols on the generation of turbulent flows [62]. Yet, it must be noted that there isn't much available research regarding the boundary layer effects of winglets on generated turbulent flows. The resulting shaft configuration can be seen in Figure 2.6.

The winglets were attached by alternating between the top and bottom sides of

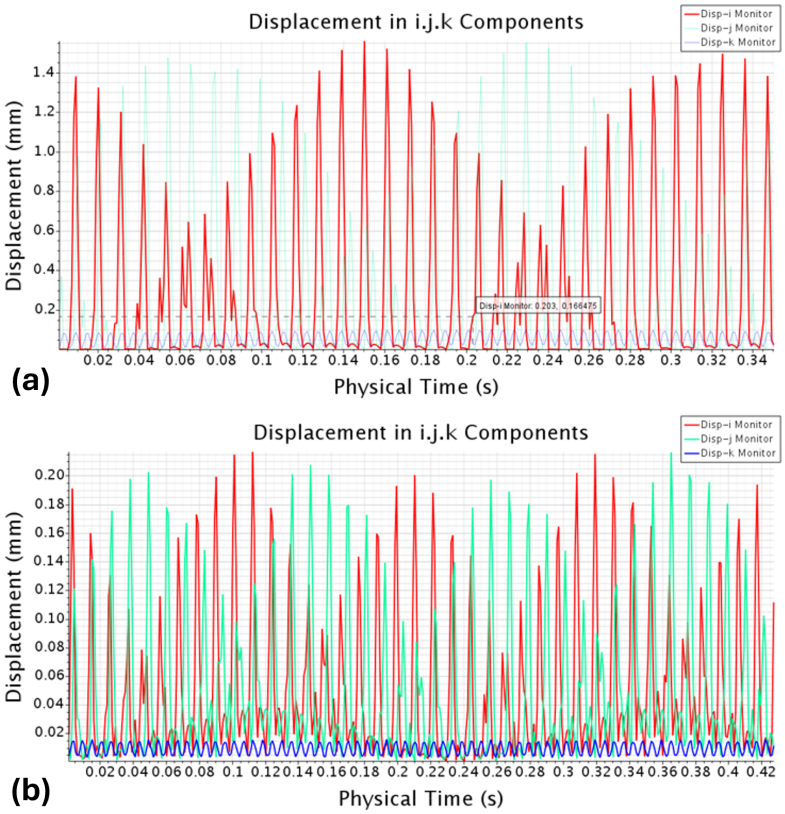
Figure 2.6: *Shaft configuration with square winglets.*



the shafts. The original configuration, with all winglets on one side, proved unstable during dynamic analyses. Considering that the maximum distance between winglets is 5 mm, there is a potential risk of collision. The first configuration exhibited a maximum displacement of approximately 1.5 mm, which could result in a 3 mm gap closure if the shaft deformation aligns harmoniously. Additionally, this estimate does not account for manufacturing misalignment, further increasing the possibility of collisions. The displacement, or the deformation graphs for a single shaft at 3000 RPM can be seen in Figure 2.7. The analysis was conducted under zero flow conditions with solid stress model and finite element solid energy for two proposed versions of winglet configurations as mentioned above. Figure 2.7(a) displays the displacement of the shaft in i and j components as it rotates in the k-axis with all winglets in one side while Figure 2.7(b) demonstrates the displacement for the shaft with winglets alternating between the top and bottom sides of the shafts.

The shafts are connected to SKF 2200 E-2RS1TN9 self-aligning bearings. These

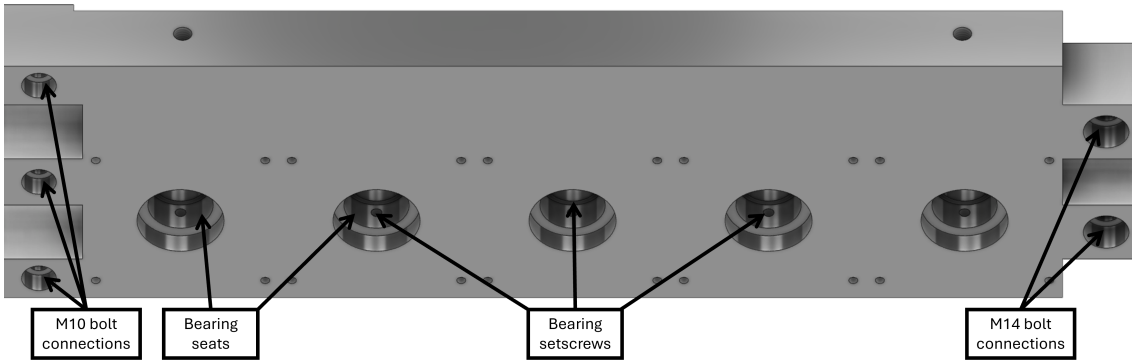
Figure 2.7: *Results of the dynamic analyses done utilizing solid stress and finite element solid energy models in STAR-CCM+ (15.06.007) for a single shaft rotating at a rate of 3000 RPM; the maximum rating of the motors.*



bearings were chosen due to their high ratings of static and dynamic loads, and their ability to operate with misaligned shafts. For a proper fit, the 10mm section of the shafts were given j6 tolerance with respect to the js7 bore tolerance on the bearing. This allowed a tight fit, yet not so tight as to prohibit disassembly. Furthermore, the bearing seat was given a js6 tolerance for a tighter fit between the foundation and the bearing to avoid any movement. Additionally, the bearings were further secured by tightening the setscrews. The active grid foundation part and the bearing seat configuration can be seen in 2.8.

There are a total of four foundation pieces: two serve as bases for supporting the lower grid, while the other two support the upper grid. The pieces are identical, yet the position of the bearing seats differ. Each piece connects to the other pieces through

Figure 2.8: *Lower grid foundation part manufactured using Aluminum 6013 for corrosion resistance.*



puzzle-like connections and to ensure a rigid assembly, the pieces are tightened using M10 and M14 socket head bolts. However, the foundation cannot be fully tightened before the shafts are inserted, so a specific procedure must be followed. Since there are two distinct foundation pieces, one will be referred to as the "upper grid foundation" and the other as the "lower grid foundation" to ensure clarity.

1. Each foundation piece (Figure 2.8) requires five bearings. Before placing any bearings, the bearing seats must be thoroughly cleaned and lubricated with machine oil. Otherwise, the bearings may be damaged, as the tolerances are quite tight and the forces exerted on the bearings could prevent them from functioning properly. Once the seats are prepared, the bearings can be gently tapped into place using a plastic mallet. Next, the setscrews can be tightened, but care must be taken to avoid applying excessive torque that could crush the bearings.

2. Prepared lower and upper foundation pieces are now ready to be connected. After joining one upper and lower foundation pieces utilizing M10 and M14 socket head bolts, and cleaning both sides of the shafts with isopropyl alcohol, the longer side of the shafts are ready to be inserted into the bearings. Due to the placement height

of the bearings, the bearings will bear the weight of the shafts, hence, a support can be inserted to the other side of the shafts to avoid any damage to the bearings.

3. Insert the remaining foundation pieces accordingly. Once the grid assembly is complete, it is crucial to attach the snap rings to both sides of the shafts to inhibit any axial movements.

2.3 Motor Assembly

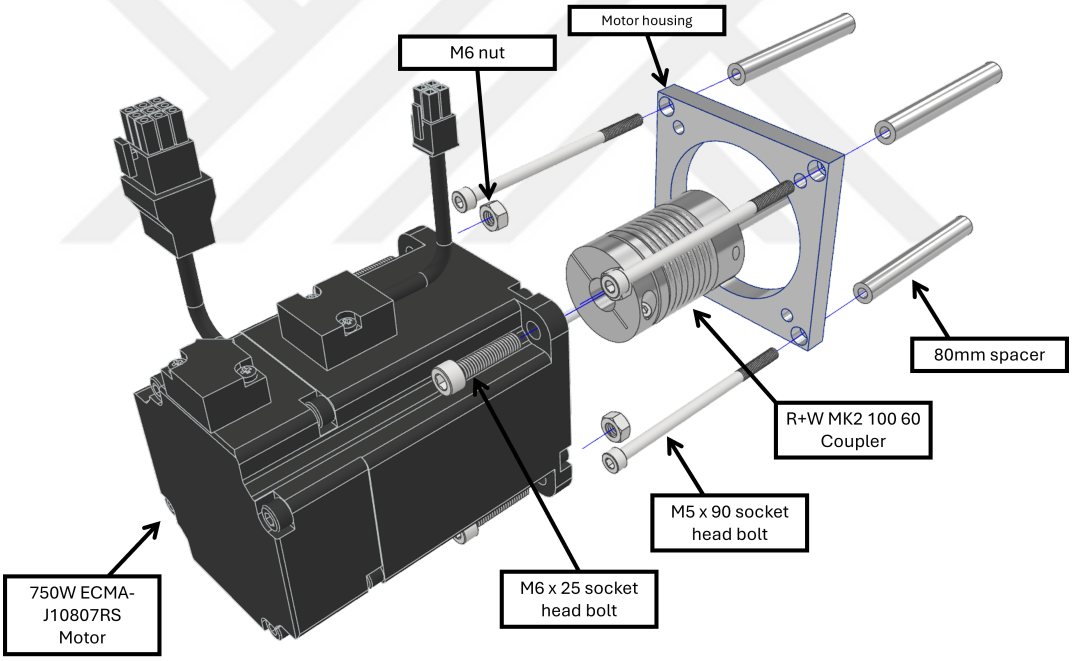
As the base is complete, the motor assembly must be attached to finish the assembly of the active grid. The motor assembly can be seen in 2.9. 750W ECMA-J10807RS: ECMA-A2 Series motor was chosen to drive the shafts as these motors can generate up 2.39 $N * m$ of torque at 3000 RPM. These ratings are adequate to support the implementation of any motion protocol without hesitation, and the high sensitivity of the integrated encoder enables precise execution of the protocols. Without a doubt, these motors are sufficient for active grid applications, as the protocols involve abrupt acceleration increments. However, the power supplied by the motors must be transmitted to the shafts efficiently and reliably. Therefore, it is critical to choose a suitable coupling that will withstand the rotational forces.

Keeping these requirements in mind, R+W brand MK2 100-60 metal bellows coupling was found to be the right choice for this application for several reasons.

1. This coupling links the motor and the shaft through a frictional type connection which involves tightening the clamps on both ends of the coupling. This allows the assembly, or disassembly, to be done in ease. Moreover, compared to the keyed connections, the deformation on the shafts is minimal due to uniform concentration of the stresses. Keyed systems tend to deform both the hub of the shafts and must be replaced if damaged.

2. A bellows coupling is well suited for accommodating misalignment while providing instant power transmission thanks to its high torsional stiffness. However, due to the nature of the design, the active grid system is susceptible to angular and radial misalignment. In addition to the design itself, manufacturing quality also plays a role; therefore, coupling must be capable of tolerating any potential misalignment. Even though the shafts contain snap rings for restricting axial movement, the shaft-bearing system has the potential to slip. The bellows coupler can tolerate these axial misplacement as well.

Figure 2.9: *Lower grid foundation part manufactured using Aluminum 6013 for corrosion resistance.*



To integrate the motor assembly with the active grid foundation, a simple housing was designed to securely hold the motor. A J6 tolerance was specified for the housing, aligned with the motor manufacturer's tolerances, ensuring a firm fit between the motor and the housing. The motor was fastened to the housing using four M6 × 25 mm socket head bolts.

Due to the motor size and limited available space, it was decided that the housing would be fixed to the active grid foundation using M5 bolts first, after which the motor would be attached to the housing with M6 bolts. Consequently, during disassembly, the motor must be removed before the housing can be detached.

Additionally, 80 mm stainless steel spacer cylinders were used to adjust the distance between the motor shaft and the grid shafts, ensuring proper alignment for the coupling connection. This spacing complies with the standard requirement that the coupling must encapsulate the shafts as fully as possible to provide adequate compression. Once the motors are integrated to the active grid assembly, the system takes the form shown in Figure 2.4.

2.4 Diffuser Design

Diffuser design can be complex, as factors such as the expansion angle and length, turbulence, pressure, flow rate and the potential for flow reversal must be considered. However, the diffuser used here is merely a junction connecting the radial fan to the active grid.

The diffuser was made by bending and welding together four galvanized steel sheets. The inlet measures 0.225 m by 0.315 m, resulting in an area of 0.070 m², while the outlet measures 0.450 m by 0.450 m, giving an exit area of 0.2025 m². The ratio of outlet to inlet area yields an expansion ratio of approximately 2.9. Given that the diffuser length is only about 20 cm, the expansion is quite sudden, creating ideal conditions for flow separation, while the differing shapes of the inlet and outlet further increase the likelihood of flow reversal. To mitigate this effect, two 10 mm mesh grids were welded at the inlet and the midpoint of the diffuser, as shown in 2.10.

Figure 2.10: *Diffuser for transferring the air from a radial fan to the active grid. Two 10mm meshes are applied to generate turbulence and avoid flow reversal.*



2.5 Nozzle Design

As with the diffuser, nozzle design requires detailed knowledge of the numerous interacting flow phenomena. The droplet breakup will initiate at the end of the contracting nozzle; hence, it is of utmost importance for the nozzle to deliver the required and expected flow to reduce the effects of unwanted phenomenon so that the droplets will only disintegrate with the expected flow dynamics. Henceforth, research was conducted thoroughly, and several analyses were done to investigate the flow induced by the nozzle.

As one can predict, the design of the nozzle was a crucial aspect of this experimental setup, as it determined the attributes and uniformity of the turbulent flow field in which droplet breakup was investigated. In particular, the works of [43, 63, 42] backed up the design approach and provided benchmarks for comparing nozzle performance.

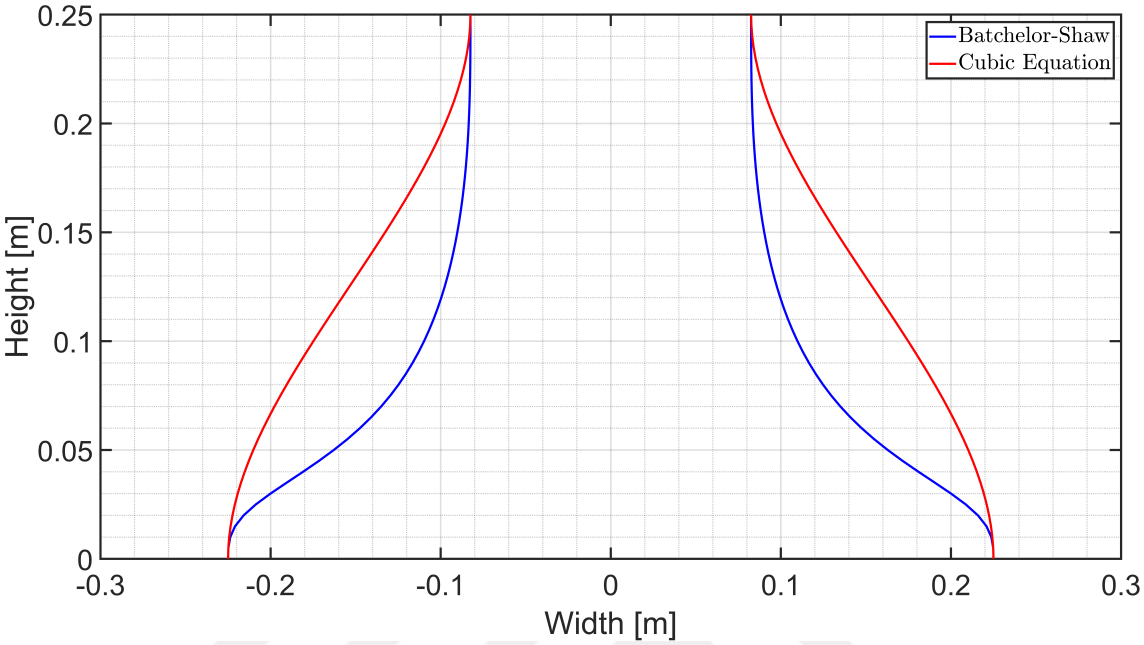
To generate a turbulent field characterized by high intensity and controlled anisotropy, while maintaining a predictable mean velocity profile, a Batchelor–Shaw–type nozzle was selected among the three nozzles. This configuration features a smooth, continuously contracting contour that produces well-defined turbulence spectra and minimizes boundary layer separation. According to Hussain and Ramjee, smooth contraction profiles of this

type significantly reduce the risk of adverse pressure gradients that can lead to recirculation zones or swirl near the nozzle exit. Maintaining attached flow was a critical consideration, as separation introduces unwanted large-scale fluctuations and inhomogeneities that compromise measurement repeatability and complicate the interpretation of droplet breakup dynamics.

Alternative geometries were evaluated in the design process. For example, ASME-standard nozzles were considered due to their ease of fabrication and widespread use in flow measurement. However, prior studies have shown that such designs are more prone to flow separation, particularly when contraction angles exceed approximately 10 degrees. Cubic equation, also called the cubic polynomial nozzles (from here on out, this nozzle will be called "cubic nozzle") offer smoother acceleration than conical designs and can reduce separation if carefully proportioned, but they still present higher sensitivity to contraction ratio and boundary layer development. In contrast, the Batchelor–Shaw profile consistently demonstrates superior performance in producing stable, reproducible turbulence while avoiding excessive turbulence amplification, which [42] observed in very high-contraction nozzles. These effects can be recognized better as one observes the constructed geometries on 2.11.

The Batchelor–Shaw nozzle features a smoothly contoured, accelerating contraction that promotes the rapid amplification and distortion of turbulence without inducing boundary layer separation towards the end of the nozzle. This design enables the turbulence to reach a quasi-equilibrium anisotropic state earlier than in many alternative nozzle geometries. While Hussain and Ramjee [43] recommended a cubic-profile nozzle for its favorable performance in maintaining flow uniformity and minimizing separation, their design required careful tuning of the polynomial coefficients to ensure acceptable pressure gradients. In contrast, the Batchelor–Shaw nozzle is a well-established, experimentally validated geometry specifically optimized for generating controlled, homogeneous

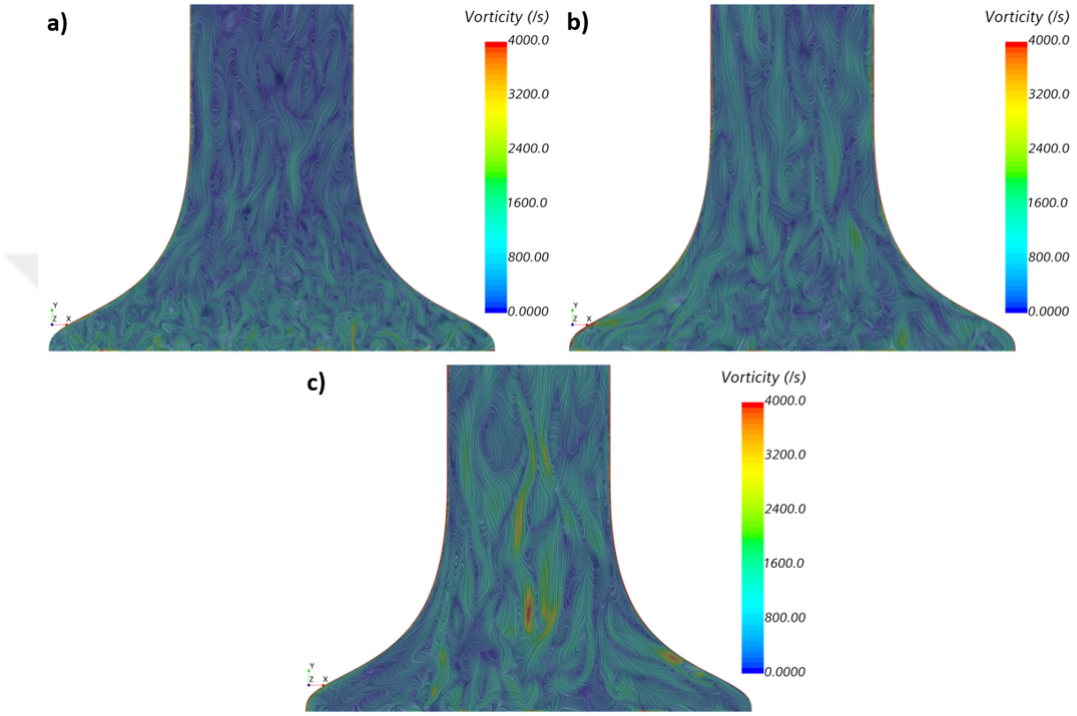
Figure 2.11: *Batchelor-Shaw and cubic nozzle geometries. The difference in contraction development between two geometries can be clearly seen in this representation.*



turbulence fields.

As the name suggests, the validity of RDT depends on the rate of distortion, or the rate of strain caused by the contracting nozzle. Therefore, the measure of rapidity of the strain in the flow is vital for the theory to be valid. In Figure 2.12, it is possible to see the alignment of vortical structures with respect to the mean flow for varying inlet velocities. The illustration clearly displays the change in the dynamics of the turbulence structure with increasing mean velocity, and the local regions of constant vorticity demonstrate the effect of an increasing rate of strain due to the higher mean velocity gradient. Therefore, during the experiments, the inlet velocities should be carefully adjusted to fall within the range where RDT remains valid. The rapidity, denoted as S^*, is a non-dimensional parameter used to characterize the rate of mean strain relative to the turbulence timescales. It is defined as:

Figure 2.12: *LES analysis of Batchler-Shaw nozzle utilizing Star-CCM+ software. Vorticity along the nozzle with varying inlet conditions. The Reynolds stresses used as inlet conditions are derived from the analysis of a single rotating winglet. The inlet conditions are assumed to be isotropic where* $\overline{u_1u_1} = \overline{u_2u_2} = \overline{u_3u_3}$. *The inlet boundary conditions are as follows: a)* $1\ m/s$, $\overline{u_iu_i} = 9.3j/kg$, *b)* $2\ m/s$, $\overline{u_iu_i} = 7.51j/kg$, *b)* $3\ m/s$, $\overline{u_iu_i} = 7.15\ j/kg$ *with an input of constant length scale of 0.085 m for all conditions.*



$$S^* = \frac{Sq^2}{\epsilon}, \tag{2.1}$$

where S is the mean strain rate, q^2 is the trace of the Reynolds stress tensor $\overline{u_iu_j}$, and ϵ is the turbulent dissipation rate. In the case of axisymmetric turbulence, the mean strain rate S can be expressed as:

$$S = \frac{\sqrt{3}}{2}\left|\frac{\partial \overline{U}_1}{\partial x_1}\right|, \tag{2.2}$$

where $\frac{\partial \overline{U}_1}{\partial x_1}$ represents the streamwise gradient of the mean velocity. For a nozzle with contraction ratio c, this gradient can be approximated by:

$$\frac{\partial \overline{U}_1}{\partial x_1} = \frac{\overline{U}_{1,\text{inlet}}(c-1)}{L}, \tag{2.3}$$

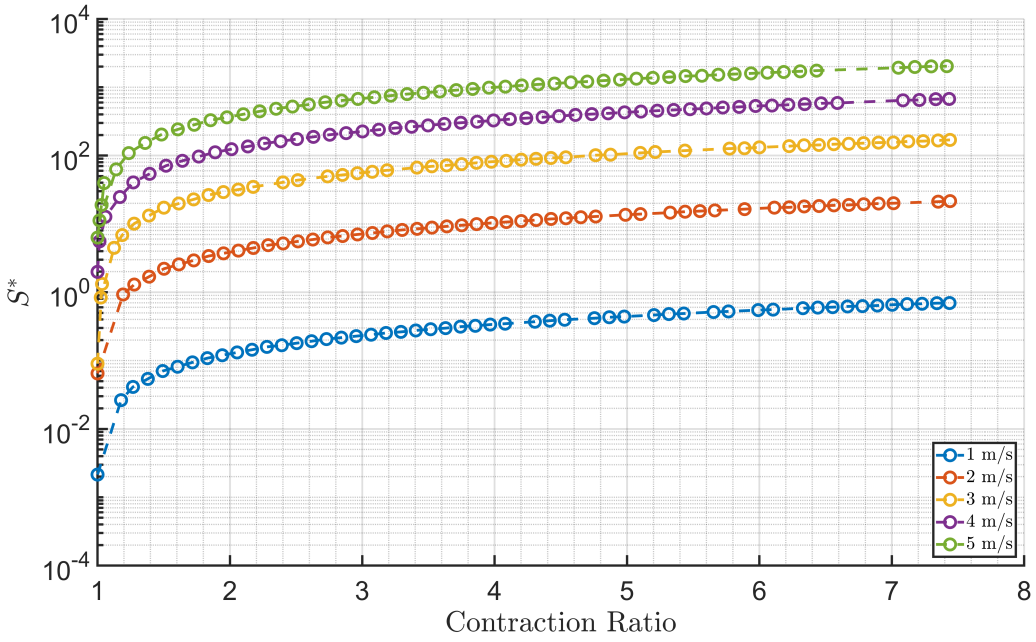
where L is the length of the contracting section. Substituting this into the expression for S and incorporating the relation $q^2 = \frac{15\nu\epsilon}{\lambda_g^2}$ (from Taylor microscale theory), the rapidity can be approximated as:

$$S^* = \frac{\sqrt{3}}{2}\left|\frac{\overline{U}_{1,\text{inlet}}(c-1)}{L}\right|\frac{\lambda_g^2}{5\nu}, \tag{2.4}$$

where λ_g denotes the transverse Taylor microscale and ν is the kinematic viscosity of the fluid [41]. The microscale λ_g was estimated by:

$$\frac{\lambda_g}{u} = \sqrt{\frac{15\nu}{\epsilon}}. \tag{2.5}$$

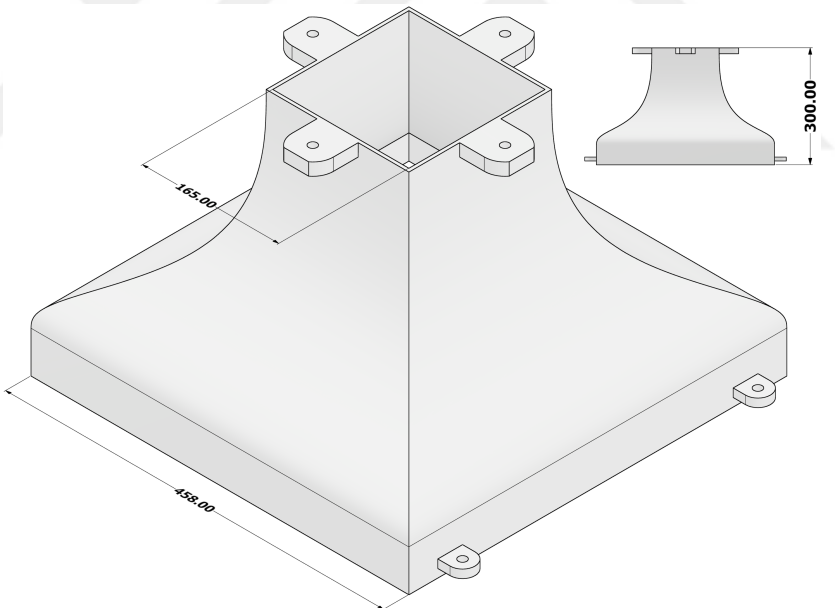
Figure 2.13: *Rapidity profiles for different inlet velocities through the contraction.*



Keeping these in mind, a Batchelor-Shaw type nozzle with inlet dimensions of

0.45 m × 0.45 m and outlet dimensions of 0.165 m × 0.165 m, yielding a contraction ratio of 7.5, was designed and fabricated with an axial length of 0.30 m (Figure 10). A contraction ratio of 7.5 was selected to remain within the range where the RDT remains valid, as larger ratios typically introduce nonlinear interactions that exceed the theory's linear framework [42]. In 2.13, the rapidity for the manufactured nozzle is shown. For RDT to hold, the rapidity parameter must be $S^* << 1$. At 1 m/s, the rate of strain is not high enough for RDT to be applicable. Therefore, the minimum inlet velocity required for RDT to hold should be 2 m/s. This is also obvious from non-aligned vorticity in 2.12. However, RDT is still applied for rough estimation of turbulence characteristics.

Figure 2.14: *A Batchelor-Shaw profile nozzle designed to yield a contraction ratio of 7.5. The nozzle is attached to the active grid through the M10 connection points near the base of the nozzle. The four joints available at the tip of the nozzle are used to connect the test section. The dimensions are in millimeter.*



The nozzle was fabricated using 3D printing technology with Acrylonitrile Butadiene Styrene (ABS) thermoplastic, chosen for its durability and reliability (2.14). Although the original intent was to manufacture the nozzle as a single unit, size constraints necessitated printing it in four separate sections, which were subsequently assembled using

adhesive. Due to the layer-by-layer nature of 3D printing, the internal surface exhibited significant roughness. To address this, the surface was first sanded and then treated with acetone vapor to achieve the smooth finish required for consistent flow characteristics.

Another aspect that must not be overlooked is the uniformity of the flow through the nozzle. Uniformity is essential to minimize the introduction of unintended flow dynamics, ensuring that the data collected during the experiments accurately reflects the effects of the controlled turbulence rather than disturbances caused by nozzle geometry. The uniformity can be checked from an analysis conducted by utilizing RSM with Quadratic Pressure-Strain relationship with a mesh field size of 2 mm. The results were gathered from the beginning of the nozzle towards the inlet of the test section. The measurement positions can be seen in Figure 2.15. The I (x_1) direction is the streamwise direction while J (x_2) and K (x_3) are the transverse directions along the nozzle.The resulting gradients throughout the nozzle are shown in 2.16. Even though J and K velocity gradients display minor non-uniformity possibly due to the wall effects produced by the curvature of the nozzle, overall the velocity gradients along the Batchelor–Shaw nozzle are exceptionally smooth and uniform, demonstrating its suitability for experimental use. The analysis could potentially be extended further until convergence is achieved, which would in turn promote symmetry in the gradients.

Figure 2.15: *The dashed redlines represent the positions at which the gradient measurements taken with the help of line probes.*

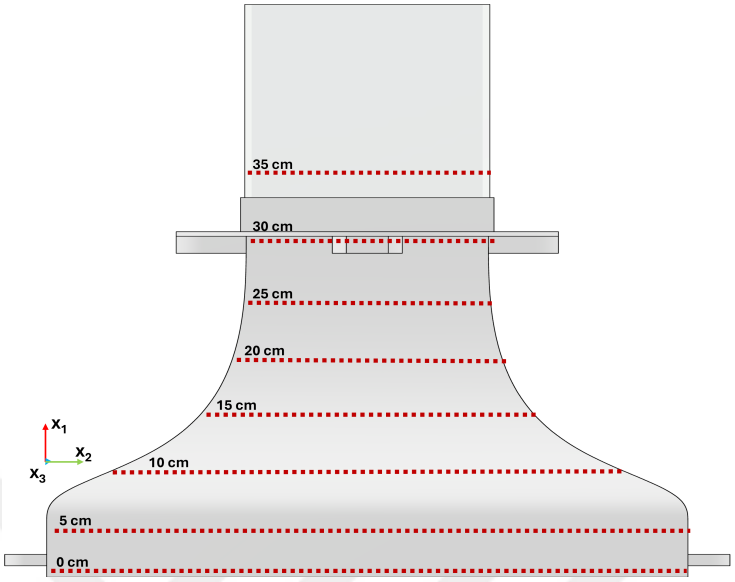
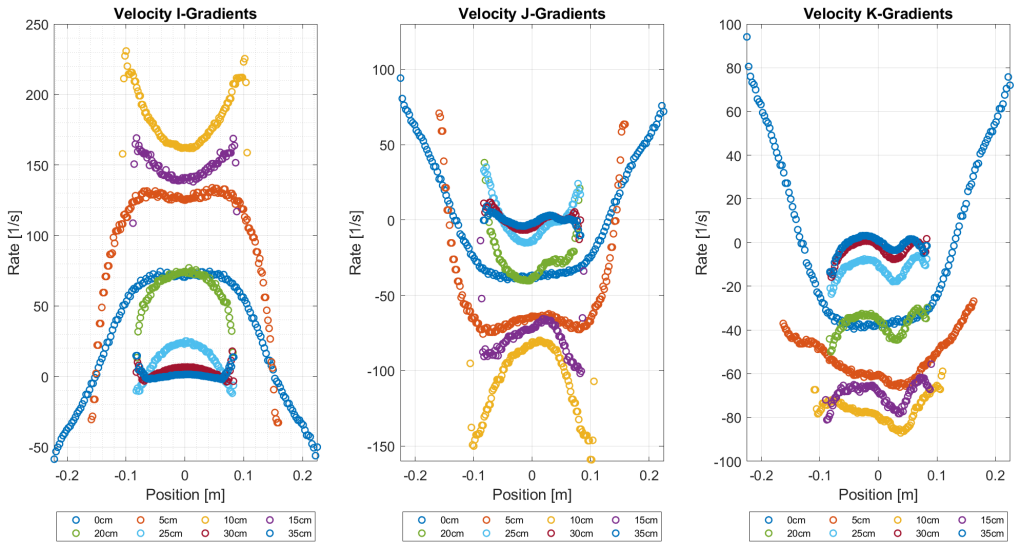


Figure 2.16: *Velocity gradients* $\partial\overline{U}_1/\partial x_1$, $\partial\overline{U}_2/\partial x_2$ *and* $\delta\overline{U}_3/\partial x_3$ *were measured along eight transverse lines extending from the nozzle axis to the wall, distributed along the axial length of the nozzle. RSM-Quadratic Pressure-Strain model was chosen. The inlet conditions are* $5\ m/s$ *with* $\overline{u_i u_i} = 7.34\ J/kg$ *and 0.085 m for the length scale.*



3. EXPERIMENTAL PROCEDURE

A radial fan can be seen on Figure 2.3 which was supplied from Euroofan with a 4 kW motor that can give the required amount of mass flow rate within specified total pressure ranges. When fully closed, the active grid blockades approximately 85% of the area; therefore, for preventing any possibility of backflow, the fan was chosen to supply 3645 m^3/h at a total pressure of 2500 Pa. The fan could operate between 0-50 Hz with 0.1 Hz increments, allowing a fine tuning for desired nozzle exit velocities. Such tuning was required as each protocol required varying fan speeds to match the pressure readings.

At an operating frequency of 50 Hz, the maximum achievable exit velocity from the nozzle reached approximately $40m/s$, corresponding to a We of $We \approx 170$. Conversely, the minimum frequency required to initiate droplet atomization was determined to be approximately 12 Hz, yielding a We of $We \approx 11$. To systematically characterize the transition between different breakup regimes, experiments were conducted across 12 discrete We spanning this range.

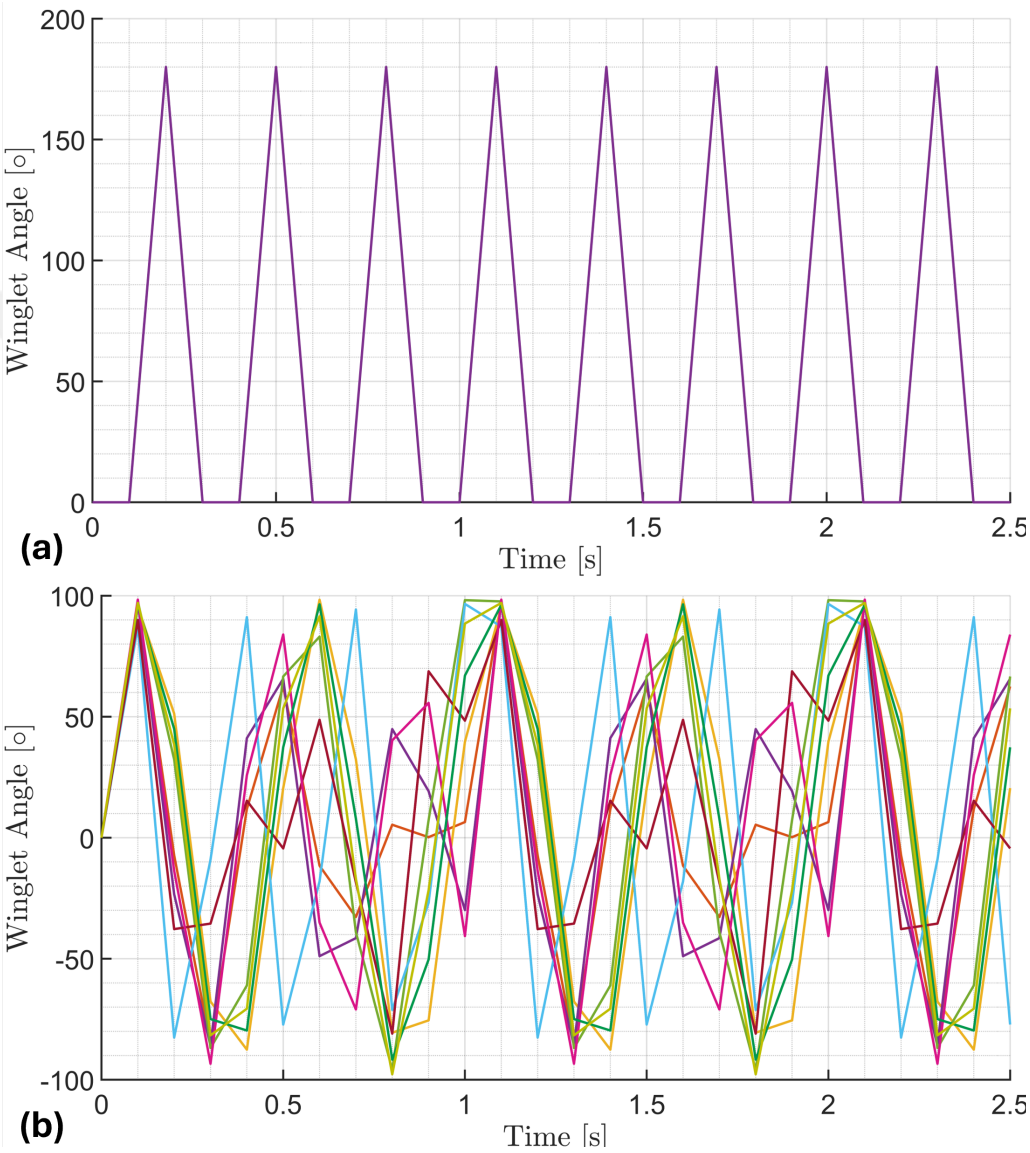
Statistical independence represents a critical requirement for these experiments to eliminate potential biases in the results. Therefore, for each We investigated, 150 individual droplets were analyzed to ensure statistically independent sampling. Given that 12 distinct We were examined across 4 different experimental protocols, this methodology resulted in the analysis of 7,200 droplets in total (4 protocols × 12 We × 150 droplets = 7,200). Building on the acquired video-capturing experience, an additional 720 droplets were analyzed using enhanced camera settings, with the primary objective of achieving optimal image quality and thereby facilitating the image-processing procedure.

3.1 Active Grid Protocols

Four motion protocols are defined for the active grid for acquiring varied levels of turbulence intensity. The protocols include open (static-low turbulence), closed (static-high turbulence), flapping and optimized motion with 52% instantaneous blockage rate. The optimized grid configuration was employed to control the blockage ratio, thereby enhancing the turbulence intensity within the flow. The flapping and optimized motion protocols can be seen in Figure 3.2. The optimized grid protocol was created by Akardere [58, 59] by utilizing genetic algorithm to optimize Rossby Number and blockage ratio.

Initially, the optimized grid contained motion data for every 0.01 seconds; however, due to the sudden acceleration of the heavy shafts, the motors could not keep up with the commands of Proportional Integral Derivative (PID) control; hence, the positional discrepancy between the command of the PID control and the motors force stopped the system. Therefore, the time step resolution was set to be 0.1s with slower acceleration levels while having a constant blockage ratio of 52

Figure 3.1: *The motion protocols implemented to each individual motor. (a) Flapping protocol with a blockage rate that alternates between 30% (minimum blockage and 85% (fully blocked) as the flaps rotate 180 degrees. All motors have the same motion. (b) Optimized protocol. Each color in the plots represents the individual motion of the motors. At any instant, the blockage rate is kept constant at 52%.*



3.2 Pressure Measurement

Gas velocity measurements were obtained using an ABB DP-Style PDS 300 Differential Pressure Transmitter, with pressure taps positioned at the inlet of the nozzle and at the exit via a Pitot tube. For the installation of the pressure port, a 1 mm diameter hole with a 4 mm seating was precisely machined, into which a copper pipe was inserted. The pipe was secured using a metal-to-plastic adhesive, which, upon full curing, provided a rigid and leak-resistant seal. To maintain alignment and structural stability during the curing process, a mechanical support was positioned beneath the pipe, and the assembly was left undisturbed for 24 hours.

Ensuring accurate and consistent pressure readings requires careful attention to the proper installation of the pressure transducer. Accordingly, several critical guidelines were followed, as outlined below:

1. The diameter of the pressure tap must be sufficiently small to avoid disturbing the flow field. In practice, tap diameters in the range of 0.5 to 1.0 mm are typically preferred, as they minimize the potential influence of the pressure port on the local flow characteristics.

2. The pressure tap must be drilled perpendicular to the wall surface to ensure accurate static pressure measurement. If the hole is introduced at an angle, the pressure transducer may detect a combination of static and dynamic pressures, resulting in a reading closer to the total pressure rather than the intended static component. Additionally, depending on the local flow conditions, flow separation can occur within the tap if misaligned, leading to unsteady and unreliable pressure signals. To ensure precision and consistency, a mechanical stand was employed to stabilize the rotary tool (Dremel) during drilling and to maintain perpendicularity with the wall surface.

3. Following the drilling process, it is essential to ensure that the pressure tap is free of burrs, as even minor surface irregularities can significantly affect the accuracy of the pressure measurement by inducing local flow disturbances and fluctuations near the tap entrance. To mitigate this risk, the hole was carefully cleaned of debris, and acetone was applied to smooth the inner surface, given that the nozzle was fabricated from ABS plastic.

4. Prior to adhesive application, the copper tubing was carefully prepared. A 4 × 2 mm copper tube was cut to a length of approximately 5 cm, and both ends were processed to achieve a smooth surface finish. The tube ends were then inspected using a Universal Serial Bus (USB) microscope to ensure the absence of burrs or surface defects that could interfere with measurement accuracy or sealing integrity. Following inspection, a flexible silicone tube with a 2 mm inner diameter was fitted over the copper tube, fully encapsulating it to facilitate connection to the pressure transducer. The length of the silicone tubing was minimized, as extended tubing can introduce time delays and dampening effects in the pressure signal transmission.

5. Given the highly turbulent nature of the flow, the pressure signal is expected to exhibit high-frequency fluctuations. To ensure reliable and stable measurements, appropriate damping was applied to the pressure transducer to attenuate these rapid oscillations without compromising the overall response time.

6. The transducer was zero-calibrated under no-flow conditions to eliminate baseline offset in the pressure readings. Additionally, the measurement range was configured according to the expected experimental conditions to maximize data resolution and ensure accurate capture of pressure variations within the operational range.

Whenever the pressure reading stabilized, the experiments were initiated. The gas velocity was simply calculated through mass conservation equation (3.1) and Bernoulli's

equation (3.2).

$$\rho A_1 V_1 = \rho A_2 V_2 \tag{3.1}$$

$$P_1 + \tfrac{1}{2}\rho v_1^2 + \rho g h_1 = P_2 + \tfrac{1}{2}\rho v_2^2 + \rho g h_2 \tag{3.2}$$

The goal here is to calculate the velocity at the inlet (V_1) of the nozzle. Hence, by manipulating equation (3.1) and assuming constant density, V_1 is obtained by

$$V_1 = \frac{A_2 V_2}{A_1} \tag{3.3}$$

where A_2/A_1 is simply the contraction ratio, c. Assuming that there is no change in height and P_2 is simply the atmospheric pressure, then plugging in equation (3.5) to (3.2) results in

$$V_1 = \sqrt{\frac{2(P_2 - P_1)}{\rho(c^2 - 1)}} \tag{3.4}$$

With known inlet velocity, the velocity at the exit of the nozzle can be approximated through

$$V_2 = cV_1 \tag{3.5}$$

These relations are used for calibrating the data acquired by hot-wire measurements. Pressure readings from a pitot tube were also taken to verify the accuracy and validity of the actual pressure measurements. The pitot reading were taken by the hand pressure measurement instrument HMG-03 manufactured by Paul Gothe GmbH. The readings are almost identical at low We ranges; however, after $We \approx 80$, the velocities obtained from pitot readings are, in average, 6.13% higher. This may be due to the range of the device as its maximum rating is 1000 Pa.

3.3 Droplet Atomization Experiments

The droplet experiments can be separated into two phases; the initial experiments were conducted for the sole purpose of observing droplet breakup types for varying We and grid protocols and the second phase involved the capturing the high-speed footage of droplet breakup that is suitable for proper image-processing.

The experiment begins by adjusting the syringe pump and the operational frequency of the fan in accordance with the pressure readings. Based on the active grid protocol, once the desired pressure is reached, the flow is allowed to stabilize for 10 seconds. Subsequently, the syringe pump is activated to inject droplets into the turbulent flow. The recording system is then initiated, capturing approximately 1.2 seconds of data at a time, enabling the capture of nearly 10 droplets per recording interval. The recordings were saved for post-processing. This procedure was repeated for all We ranges and protocols.

3.3.1 Droplet Generation

Droplet generation was achieved by operating a syringe pump and a G21-0.8mm needle. With the proper settings, the system can consistently generate droplets of 2.35±0.1mm in diameter. The droplets had to be introduced into the test section without initial deformation at the tip of the needle; therefore, a stagnation region had to be created. This was accomplished by attaching the needle into a 12x8mm plexiglass tube with a length of approximately 0.25m. This allowed the droplet to exit at a velocity of 1.85 m/s. This is a crucial parameter as the droplet must disintegrate far away from the tube, without the influence of the flow field created by the tube. However, at high We, this was not possible as the incoming velocity dominated, and the droplets disintegrated immediately after exiting the tube.

3.3.2 Droplet Visualization

High-speed imaging was performed using a Phantom Fastcam Nova S6 800K-M-16GB camera with a Nikon AF Micro Nikkor 200 mm lens to capture close-up images of the droplet breakup process. The PFV4 (x64) software was used to control the high-speed image capture. Since twelve different We were tested, the frame rates and shutter speeds were carefully selected for each condition to obtain the best image quality. A 100 W Light Emitting Diode (LED) panel was used as the light source, but it did not provide enough light at higher gas velocities. Therefore, frame rates and shutter speeds were adjusted to compensate for the lower light levels. To create a smooth background and avoid false edge detection, a piece of fine cloth was placed behind the test area to provide uniform contrast across the imaging region.

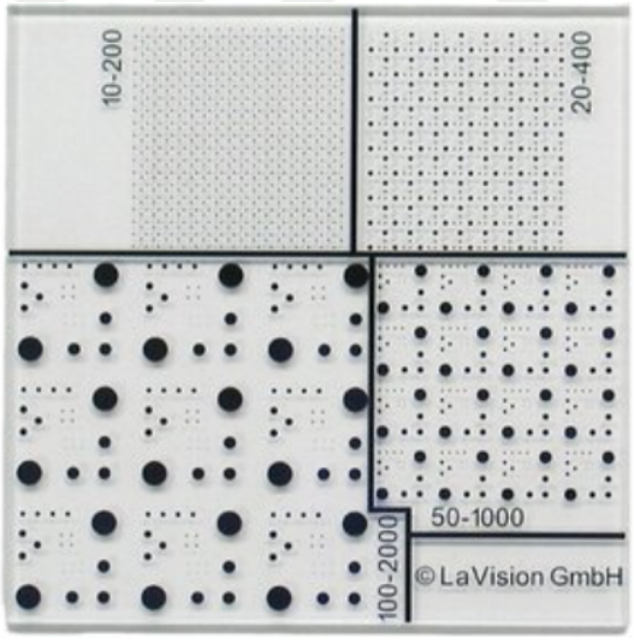
The image processing of the images in high We ranges ($\sim 100 - 170$) were demanding as the proper contrast for edge detecting was difficult to achieve. Yet, since identical camera settings available on Table (3.1) were applied between the grid protocols, the extracted atomization data will only show variations due to flow conditions.

The diaphragm aperture and depth of field were carefully calibrated using a transparent calibration plate specifically designed for shadowgraphy applications. Once the optimal depth of field and focus parameters were established, the camera settings remained fixed and undisturbed throughout the entire experimental campaign to ensure consistent imaging conditions.

Table 3.1: *Camera settings were optimized and standardized to ensure uniform image acquisition and maintain consistent imaging quality across all experimental conditions.*

We	Frame Rate	Shutter Speed
∼13	15,000	1/80,000
∼22	20,000	1/80,000
∼28	20,000	1/80,000
∼32	20,000	1/80,000
∼40	24,000	1/80,000
∼61	24,000	1/80,000
∼77	32,000	1/100,000
∼90	36,000	1/100,000
∼105	36,000	1/100,000
∼125	40,000	1/100,000
∼145	50,000	1/150,000
∼170	50,000	1/150,000

Figure 3.2: *Transparent shadowgraphy calibration plate by LaVision.*



3.4 Hot-wire Anemometry

Hot-wire anemometry operates on the principle of heat transfer from a wire, typically composed of tungsten or platinum (in this study, tungsten wire was utilized), to the surrounding fluid. When the wire is heated by an electric current, the fluid flow induces heat transfer, cooling the wire. The rate of cooling is directly proportional to the fluid velocity, allowing for the determination of velocity by maintaining a constant temperature of the wire CTA. The electrical power required to maintain this constant temperature is thus related to the fluid velocity. This technique is favored over other methods due to its high spatial resolution, which allows for the measurement of velocity at small scales, and its high-frequency response, making it particularly suited for turbulence analysis. Unlike pressure-based techniques, hotwire anemometry minimally disturbs the flow field, enabling detailed measurements of both mean velocity and turbulent fluctuations without significantly affecting the fluid dynamics; an important aspect as turbulent structures are exceptionally sensitive to any available obstruction in the flow field.

The installation and preparation of a hot-wire probe are critical to ensuring accurate and reliable measurements. Proper probe positioning is essential, typically achieved through a mechanical traverse system that ensures the wire is oriented perpendicular to the flow direction. Misalignment can lead to significant measurement errors, therefore the probe and the constructed superstructure was aligned with the aid of a water gauge. Calibration is required to establish a relationship between the voltage output and fluid velocity, often performed by testing the probe in a controlled flow with known velocity, such as using a pitot tube.

Environmental factors such as temperature and humidity must be carefully monitored and accounted for, as they significantly affect the wire's heat transfer properties and the overall measurement accuracy. Variations in temperature and humidity can alter the

thermal conductivity of the fluid, thereby influencing the cooling rate of the wire. Additionally, stabilizing the power supply is crucial to prevent fluctuations that could lead to erroneous data or instability in the system. Proper insulation of wire connection points is equally important to prevent hot-wire burnout, which can occur due to electrical shorts or overheating.

Furthermore, it is good practice to ensure that the medium used for experiments is properly filtered to remove any micro-particles or contaminants that could interfere with the data acquisition process. Micro-particles in the fluid can affect the hot-wire's heat transfer characteristics, leading to inaccuracies in velocity measurements. Contaminants can also cause physical damage to the probe over time, reducing the reliability and longevity of the measurement system.

The initiation of the hot-wire experiments followed a similar procedure to the droplet experiments. After allowing the flow to develop, hot-wire readings were then acquired using LabVIEW for data collection and analysis.

3.4.1 Hot-wire Anemometry Experiments

The measurements were conducted using a Dantec Dynamics 55P11 single hot-wire probe, with resistance calculations and adjustments made on the mini-CTA 54T42 in strict accordance with the manufacturer's guidelines. To ensure precise data acquisition, an National Instruments (NI)-Compact Data Acquisition (cDAQ) chassis was employed in conjunction with the NI-9220 module. This module, capable of collecting real-time data at a maximum rate of 100 kS per second across its 16 channels, was specifically chosen for its compatibility with the required sampling rate of 30 kHz. The selection of an appropriate data acquisition module is a critical factor in ensuring the reliability and accuracy of the measurement process. A module with an insufficient sampling rate could lead to aliasing or signal distortion, thereby compromising the integrity of the data. In contrast,

the NI-9220 module was selected to match the high-frequency response of the hot-wire probe, ensuring that the captured data accurately reflects the dynamic turbulence fluctuations without distortion. This careful consideration of module capabilities is essential for obtaining reliable and meaningful measurements in high-speed turbulence studies.

The hot-wire probe was mounted on a vertical traverse system which enabled measurements at varying positions in the streamwise direction. For each measurement point, three sets of 3 million data points were acquired, totaling 9 million data points per position. Six measurement locations were established at 5 mm intervals to quantify turbulence decay; however, the kinetic energy calculations did not reveal any evidence of decay [19].

Measurements were taken both perpendicular to and at an angle of 30° relative to the flow direction to capture the longitudinal and transverse velocity components, respectively. Although the data has been collected, proper calibration relationships must still be derived for calculating transverse turbulence quantities. This aspect constitutes an ongoing study which will not be addressed here. Instead, RDT is applied for turbulence predictions.

3.4.2 Hot-wire Anemometry Calibration

The voltage data collected from hot-wire experiments must be converted into velocity data to effectively investigate turbulence characteristics; therefore, calibration is essential. Calibration involves first setting the active grid to an open protocol, as it induces minimal turbulence, and adjusting the operational frequency of the fan in intervals of 5 Hz. An example of a calibration table for the open grid is presented in 3.2.

The calibration of a hot-wire anemometer can be performed using a linearized equation (3.6) proposed by H. H. Bruun [64], which relates the output voltage of the hot-wire to the fluid velocity.

Table 3.2: *Experimental data for different fan frequencies and corresponding flow parameters.*

Fan Hz	Pressure [Pa]	Offset Pressure [Pa]	Pitot Pressure [Pa]	Velocity In [m/s]	Velocity Out [m/s]	We	Pitot-Exit Velocity
0	2.8	0	-	-	-	-	-
10	38.7	35.9	51	1.0693	8.020	8.13	9.12
15	79.6	76.8	117	1.5337	11.50	16.69	13.82
20	134.6	131.8	196	1.9944	14.96	28.23	17.89
25	203.1	200.3	298	2.149	18.37	42.61	22.06
30	296.4	293.6	435	2.959	22.20	62.2	26.65
35	408.5	405.7	605	3.474	26.06	85.7	31.43
40	541	538.2	792	3.9983	29.99	113.5	35.96
45	695.5	692.7	995	4.5335	34.00	145.9	40.31
50	866.5	863.7	1240	5.0601	37.95	181.7	44.98

$$E(t)^2 = A + BU_e(t)^n \tag{3.6}$$

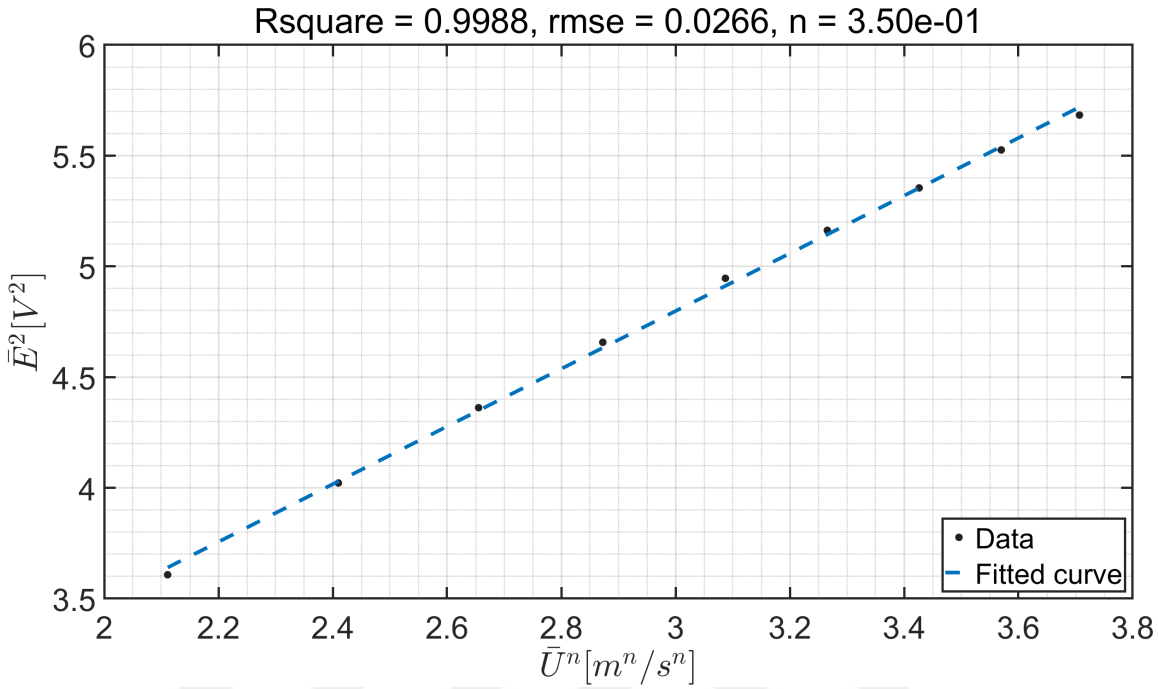
Since $\overline{U_e}$ is known from calibration measurements, the equation

$$\bar{E}^2 = A + B\bar{U}_e^n. \tag{3.7}$$

can be used to calculate the calibration constants A, B and n.

By squaring the raw voltage signal and using the corresponding velocity profile from table 3.2), the value of n can be adjusted to achieve the optimal fit for the data. It was decided that the best fit was achieved when $n = 0.35$ and the calibration constants A and B were calculated. The calibration curves can be seen in Figure 3.3. It should be noted that the calibrations for each protocol were conducted with the active grid in a fully open and stationary configuration, meaning no winglet motion was applied during the calibration process.

Figure 3.3: *Calibration graphs optimized grid. The Rsquare, and RMSE values can be seen above the graphs.*



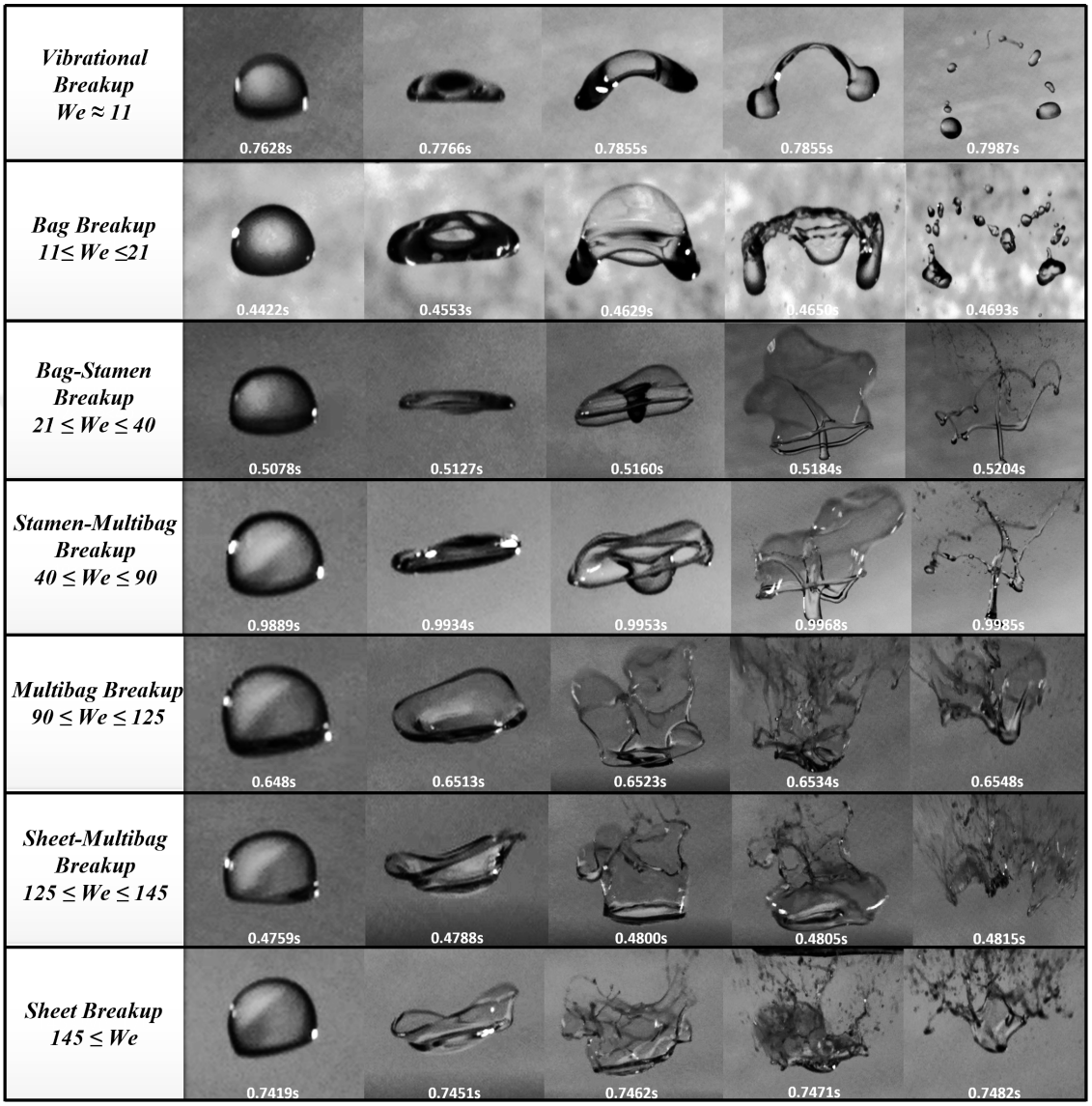
4. RESULTS

This chapter presents the results from both droplet atomization and hot-wire experiments, with a focus on the relationship between atomization processes and turbulence characteristics. It investigates how different turbulence regimes affect the breakup mechanisms of droplets, specifically examining the transition between distinct breakup regimes. By analyzing the hot-wire measurements alongside the droplet data, the chapter explores how turbulence intensity influences the nature of droplet deformation and fragmentation.

4.1 Droplet Breakup Statistics

The droplets exhibited a range of breakup behaviors, as seen in Figure 4.1, which were categorized into distinct types. To quantify the breakup probability for each type, the Wilson score interval method was employed. This statistical approach provides a more reliable estimation of the true breakup probabilities, especially given the variability in the observed breakup behaviors across different We. The Wilson score interval was chosen due to its superior accuracy over traditional methods, particularly for proportions close to 0 or 1, and for its ability to handle small sample sizes effectively. For each We, the observed proportion of droplets exhibiting each breakup type was calculated, and the corresponding Wilson score interval was computed to provide a confidence range for the true breakup probability. This method ensures that the calculated probabilities are more precise and robust, reducing potential bias introduced by extreme values or small sample sizes.

Figure 4.1: *Observed droplet breakup types through various Weber ranges. Note that these Weber ranges are rough estimates among the all used active grid protocols*

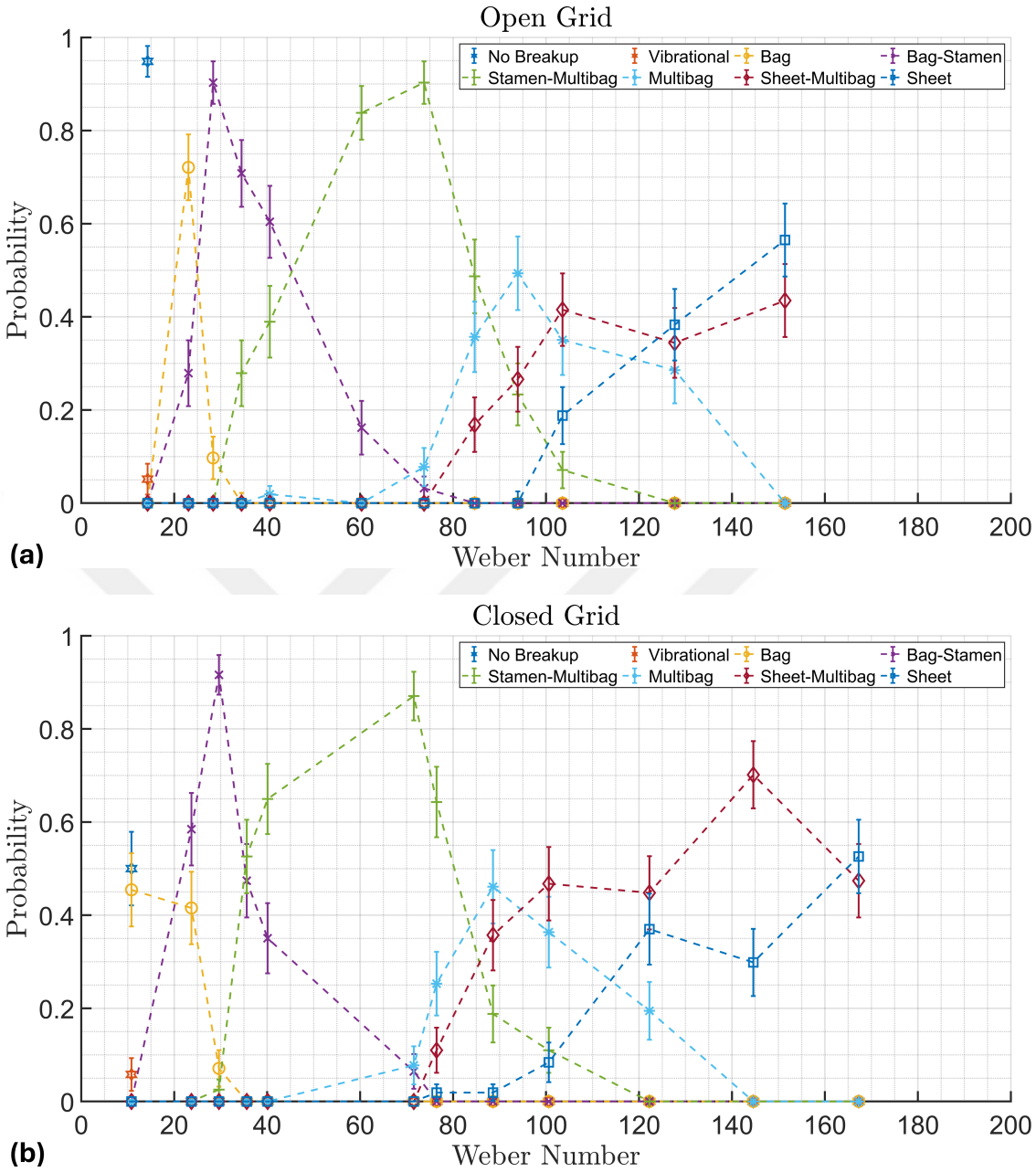


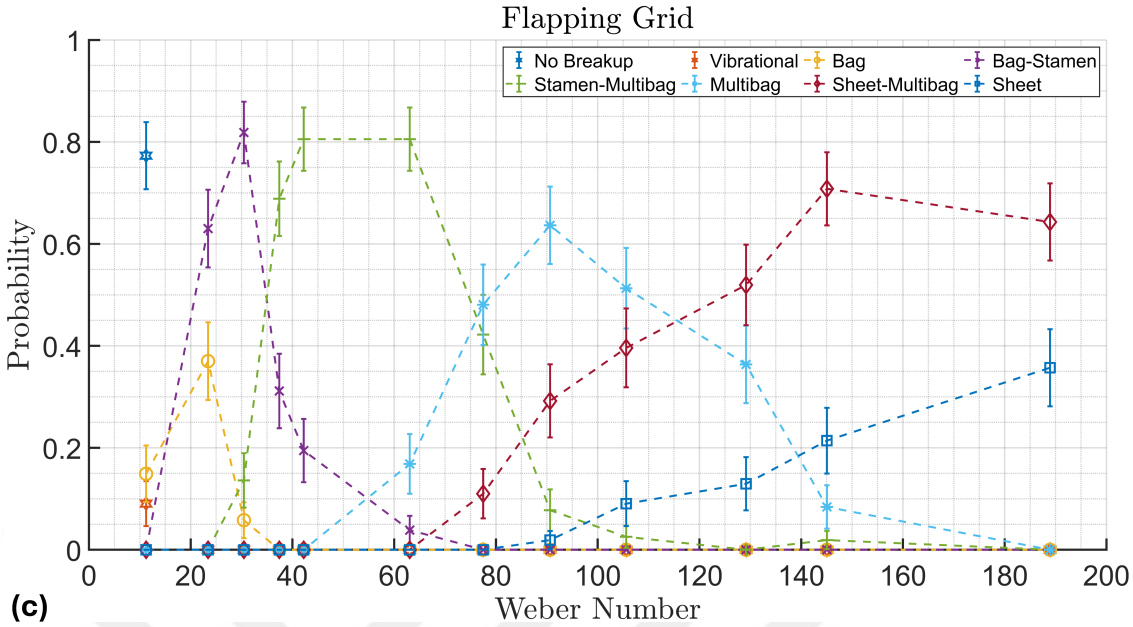
For each Weber, the counts of specific breakups observed were counted and divided by 150 for estimating the probability, P_{exp}. Then, for determining the uncertainty in estimated probability P_{exp}, Wilson score interval method was applied which is given as [[65]]:

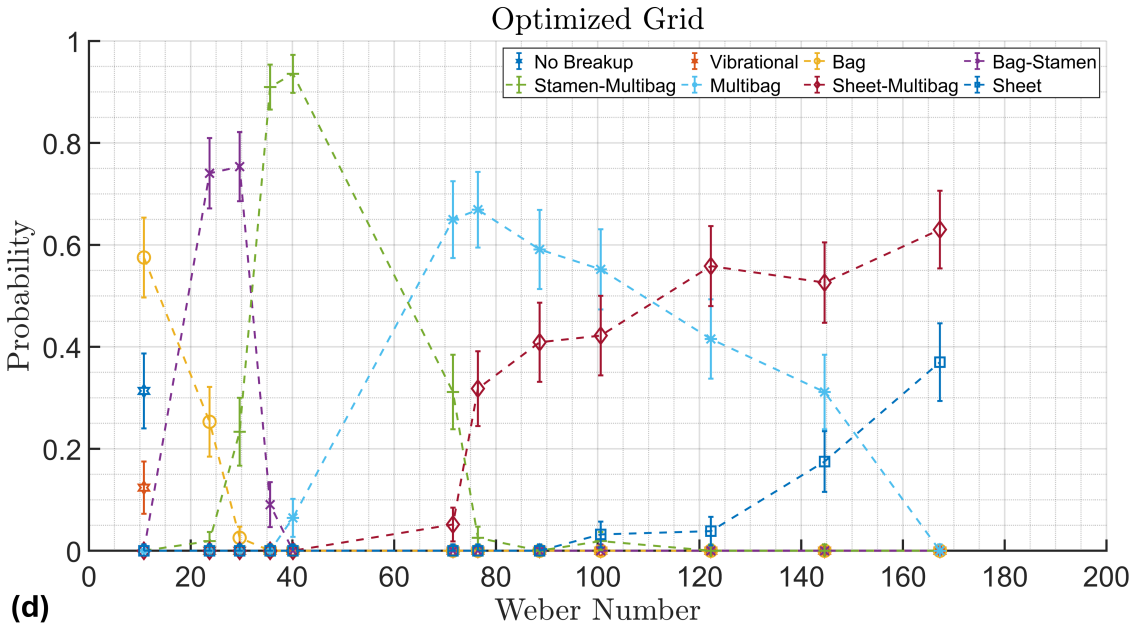
$$P_{Wilson} = \frac{P_{exp} + \frac{Z^2}{2n}}{1 + \frac{Z^2}{n}} \pm \frac{Z}{1 + \frac{Z^2}{n}} \sqrt{P_{e\hat{x}p}\left(1 - P_{exp}\right) + \frac{Z^2}{4n}}. \tag{4.1}$$

where Z is the $Z - value$ for a chosen confidence level, and n is the sample size. A 95% confidence interval was chosen, corresponding to $Z = 1.96$. The first term in the formula modifies the observed proportion by incorporating a correction factor that accounts for the sample size, ensuring a more accurate estimate. The second term calculates the confidence interval's width, which reflects the uncertainty of the estimate. This width is influenced by the standard error, which takes into consideration both the observed proportion and the number of observations, thereby quantifying the variability of the estimate. The calculated probability estimations can be seen in Figure 4.2.

Figure 4.2: *Droplet breakup statistics based on type of breakup. Each graph displays the statistics of breakup types with respect to active grid protocols.*







Looking at Figure 4.2, analyzing low Weber ranges give rather intriguing results. At $We \approx 12$, open grid fails to initiate the breakup mechanism compared to other grids. Bag breakup dominates closed and optimized grids while the flapping grid displays alterations between Vibrational and Bag breakup. It seems that the disturbances caused by the motion of the grid successfully initiate instabilities on the droplets. Progressing to

$We \approx 25 - 35$, the Bag-Stamen breakup follows a similar trend between all protocols where open grid achieves the highest probability. The shared probability of Bag and Bag-Stamen types can be seen on flapping and closed grids. Interestingly, the optimized grid at these levels displays consistent Bag-Stamen breakup; however, at $We_g \approx 35$, Stamen-Multibag breakup creeps in. This behavior is also observed for flapping grid yet; it is not as prominent. As the Weber further progresses to $We \approx 40 - 80$, the slow decay of Bag-Stamen breakup is observed in the open grid. Overall, within these Weber ranges, the static grids seem to struggle to transition towards the breakup types such as Multibag and Sheet-Multibag. As $We \approx 80 - 130$ ranges are achieved, the static grids display a faster decay in Multibag, while the grids with assigned motions conserve this property. This may be due to the dynamic eddies formed within the turbulent flow which promotes the formation of multiple bags. Finally, at $We < 130$, the probability of Sheet-Multibag and Sheet breakups are similar for all protocols, however, probability of Sheet breakup type dominates for static grids, while the Sheet-Multibag type is persistent. It seems that the dynamic eddies generated by the motion of the grid play a role in the formation of Bag type breakups.

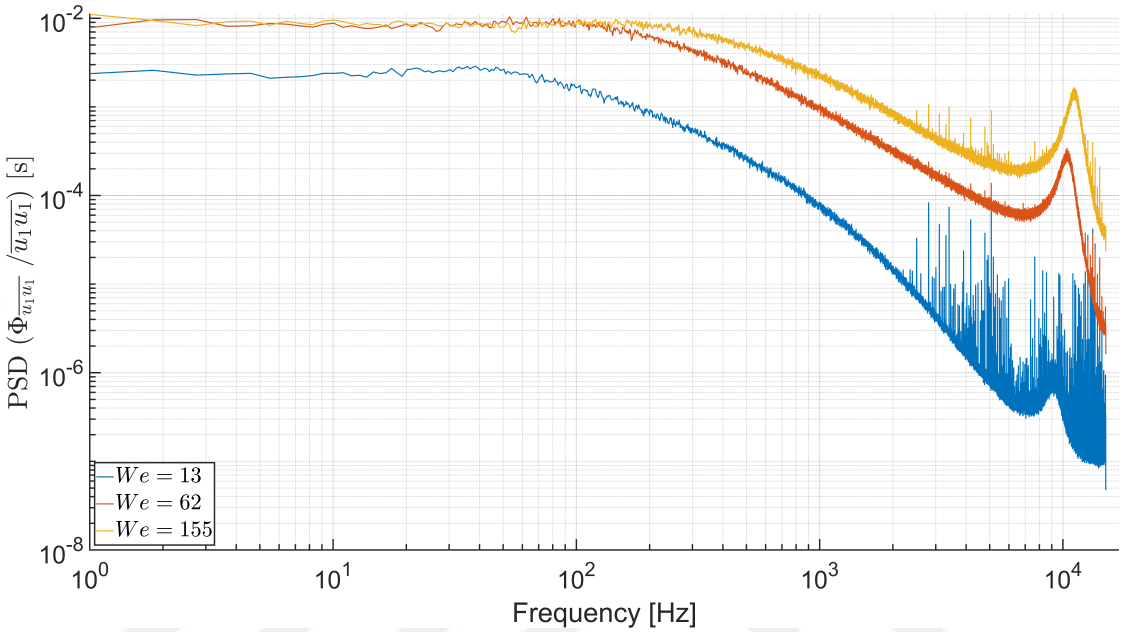
4.2 Turbulence Analysis

4.2.1 Power Spectral Density

The data obtained from the perpendicular hot-wire experiments were processed and compared across different active grid protocols. The resulting PSD for the open grid configuration is presented in Figure 4.3. To compute the PSD, the velocity signal was first segmented into one-second bins. For each segment, the power spectral density was estimated using Welch's method (pwelch function) with overlapping, and the final PSD curve was obtained by averaging across all segments. This approach ensures statistical

convergence and reduces spectral leakage, providing a more reliable representation of the energy distribution across frequencies.

Figure 4.3: *Unfiltered PSD graph for the open grid at* $We = 13, 62, 155$.



A consistent noise was observed in the data, which became more pronounced as the flow velocity increased. To mitigate this issue, a 5.5 kHz low-pass filter was applied, effectively removing the majority of the noise and improving the clarity of the measurements. It is important to note that the PSD plots exhibit a cutoff at 15 kHz, which is a direct consequence of the Nyquist frequency. According to the Nyquist-Shannon sampling theorem, the maximum frequency that can be accurately captured is half of the sampling rate. Given that the sampling rate was set to 30 kHz, the Nyquist frequency is 15 kHz, beyond which any higher frequency components would be aliased and misrepresented in the data, leading to potential distortion. The filtered PSD plots for each grid at varying We can be seen in Figure 4.4.

Figure 4.4: *PSD of hot-wire data for each protocol at varying We. A 5.5 kHz low-pass filter was applied to the data to remove noise.*

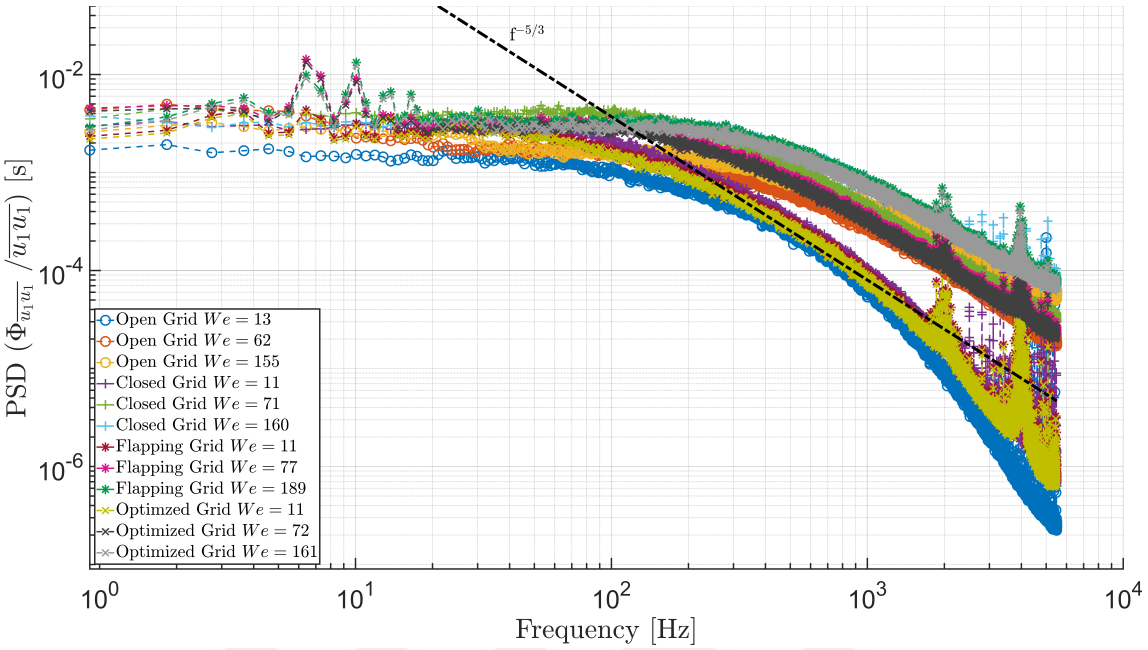


Figure 4.4 also displays the behavior of turbulence between grid protocols as We varies. It is possible to observe the spikes of energy in low frequency regions for the grids with motion protocols. This is an indication of larger scales of turbulence gaining energy from the disturbances caused by the rotating winglets. The increasing We seems to amplify this effect. Overall, the energy of $\overline{u_1u_1}$ is observed to be higher for closed grid and decay slower as We is increased; however, with increasing air velocity, the flapping and optimized grid protocols 'catch up' to the energy levels of the closed grid.

Additionally, it can be observed that the level of turbulence increases with the velocity. A more pronounced and fully developed turbulence regime is evident after $We \approx 13$, where the PSD plots begin to show a clear trend, becoming more linear and aligning closely with the $f^{-5/3}$ line. This behavior indicates a transition to an inertial sub-range, characteristic of fully developed turbulence, where the energy spectrum follows a

well-established power law typical of turbulent flows.

4.2.2 Autocorrelation

One of the important parameters in this study was the integral time and length scale calculations in the streamwise direction. The calculation of these parameters kick started the turbulence calculations. The autocorrelation function is given by

$$R(\tau) = \frac{\langle u_i(t) u_i(t+\tau) \rangle}{\langle u_i(t)^2 \rangle}, \quad i = 1, 2, 3. \tag{4.2}$$

where u_i is the fluctuating velocity component, t is time and τ is the time lag. The integral time scale T of the u_1 fluctuations can be found through integrating equation (4.2) through out the time lag domain:

$$T = \int_0^\infty R_\tau d\tau. \tag{4.3}$$

Keeping Taylor's frozen turbulence hypothesis in mind, manipulating equation by multiplying time lag with the mean velocity will result in the calculation of integral length scale. Hence, equation (4.3) becomes

$$L_{int} = \int_0^\infty R_r dr, \tag{4.4}$$

where $r = \overline{U_1}\tau$. Since only longitudinal fluctuating components are available as data, R_{11_e} and L_{11_e} will be calculated at the exit of the nozzle. The subscripts in and e will be used to represent the inlet and the outlet of the nozzle.

Figure 4.5: *Longitudinal autocorrelation of u_1 velocity fluctuations in time for various grid protocols and We. The signal was low-pass filtered at 5.50 kHz and computed by segmenting the data into 1-second bins.*

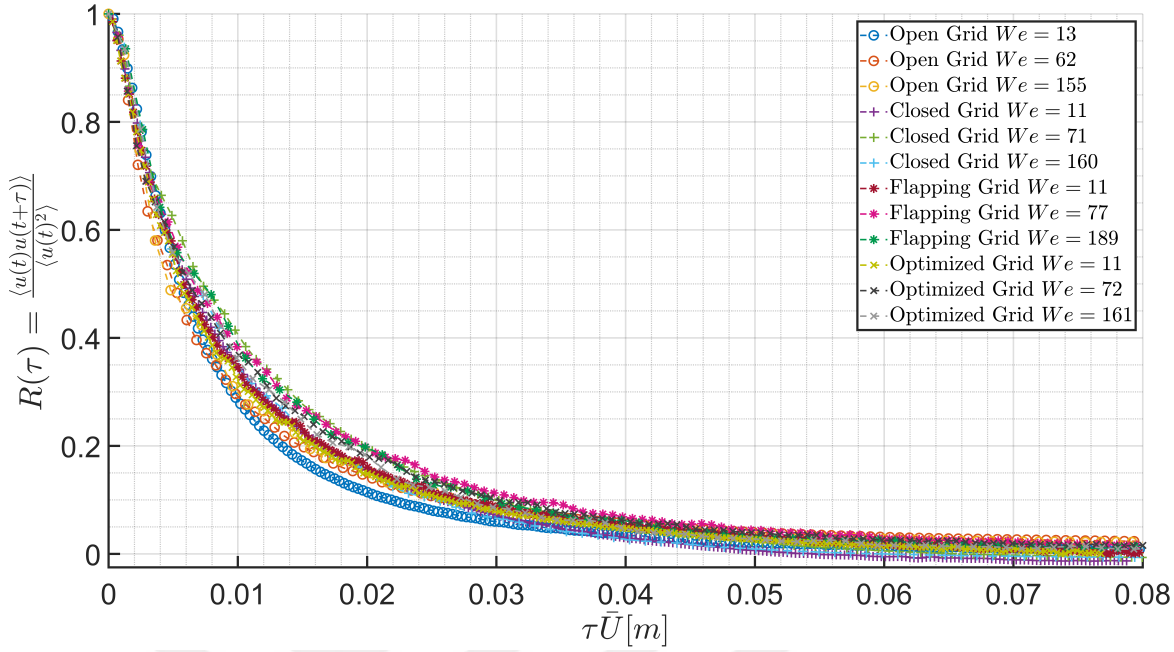
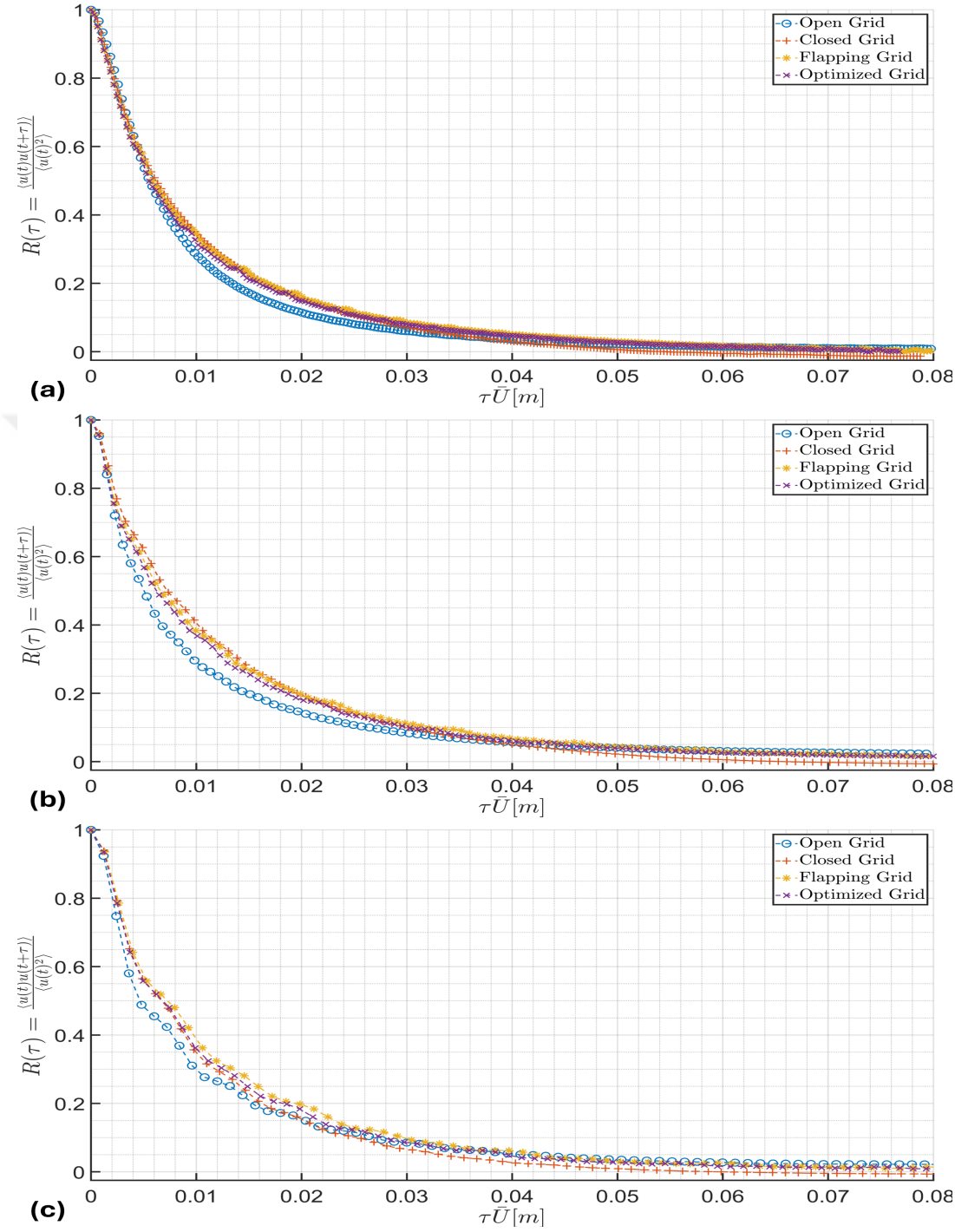


Table 4.1: *Integral time scales corresponding to different We and grid protocols.*

We	Open Grid [ms]	Closed Grid [ms]	Flapping Grid [ms]	Optimized Grid [ms]
≈13	0.8872	1.097	1.136	1.136
≈22	0.6542	0.7713	0.8150	0.8150
≈28	0.6056	0.7074	0.7482	0.7482
≈32	0.5533	0.6528	0.6757	0.6756
≈40	0.6126	0.6117	0.6348	0.6348
≈61	0.5627	0.4778	0.5727	0.5727
≈77	0.5152	0.4393	0.5175	0.5175
≈90	0.4840	0.4035	0.4614	0.4614
≈105	0.4670	0.3843	0.4303	0.4302
≈125	0.4470	0.3378	0.3626	0.3626
≈145	0.4343	0.3004	0.3491	0.3491
≈170	0.4262	0.2874	0.3149	0.3149

Figure 4.6: *Longitudinal autocorrelation of u_1 velocity fluctuations in terms of length for various grid protocols and We obtained through Taylor's frozen turbulence hypothesis. The signal was low-pass filtered at 5.50 kHz and computed by segmenting the data into 1-second bins. a) $We \approx 13$, b) $We \approx 62$, c) $We \approx 170$*



From Figures 4.5 and 4.6, the open grid contains smaller scale eddies as the timescale are relatively short. However, as We increases, this difference minimizes. An

interesting thing to note is that the correlation curves for flapping and optimized grid are almost identical. The same trend can be seen in the PSD of u_1 in Figure 4.4; however, flapping grid appear to contain additional energy compared to the optimized grid. The calculated integral time and length scales can be observed in Tables 4.1 and 4.2 and Figures 4.7 and 4.8. While the grids display a similar decreasing trend for the time scales, the length scales for the closed grid seems to be constant throughout the given We range.

Table 4.2: *Integral length scales corresponding to different We and grid protocols.*

We	Open Grid [mm]	Closed Grid [mm]	Flapping Grid [mm]	Optimized Grid [mm]
≈13	9.776	10.03	11.01	10.52
≈22	9.211	10.34	11.41	10.83
≈28	9.651	9.861	12.01	11.37
≈32	9.694	10.28	12.19	11.48
≈40	12.94	10.32	12.59	11.90
≈61	13.13	11.08	14.51	13.68
≈77	13.33	10.56	15.02	14.14
≈90	13.33	10.63	14.67	13.60
≈105	13.36	9.938	14.80	13.91
≈125	13.47	10.56	14.85	13.95
≈145	14.29	10.69	15.02	14.08
≈170	15.34	11.39	15.59	14.60

Figure 4.7: *Integral time scale of the u_1 fluctuations.*

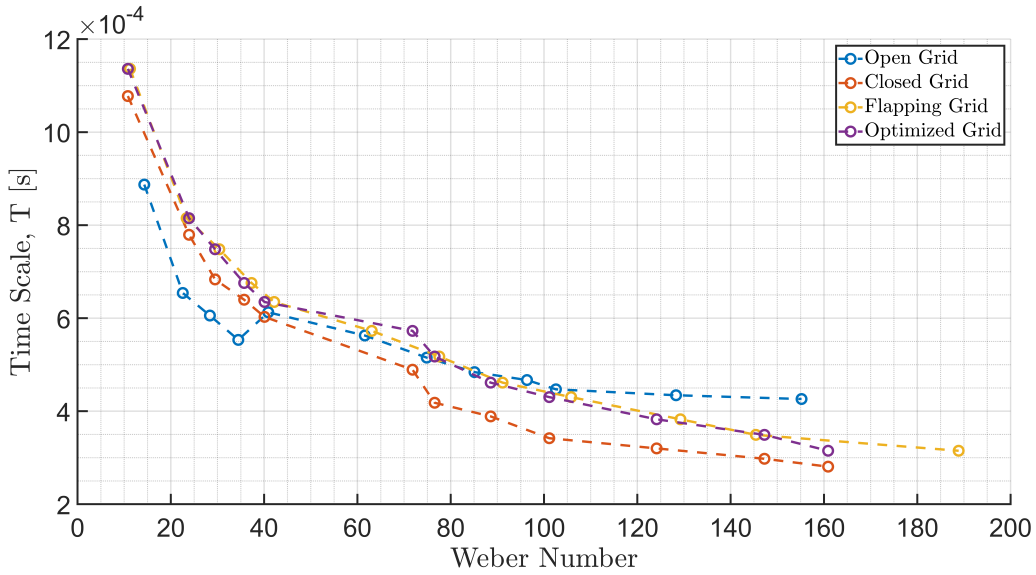
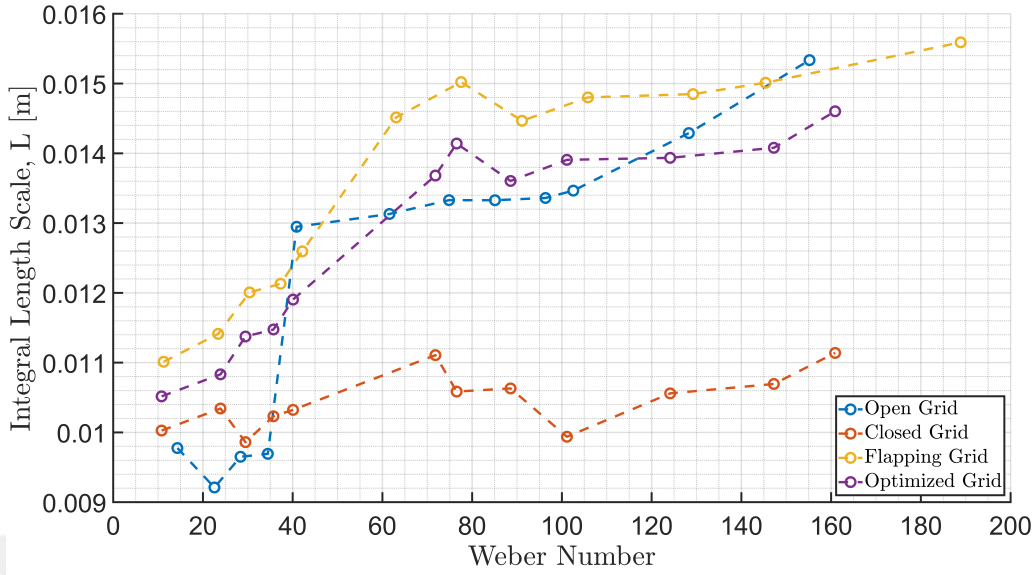


Figure 4.8: *Integral length scale of the u_1 fluctuations.*



4.2.3 Using Rapid Distortion Theory to Find Transverse Characteristics of Turbulence

With the assumption of HIT at the active grid, it is possible to find the energy of the transverse components. Utilizing the work of Batchelor and Proudman, the ratio of $\overline{u_1u_1}_e/\overline{u_1u_1}_{in}$ can be estimated by

$$\mu_1 = \frac{\overline{u_1u_1}_e}{\overline{u_1u_1}_{in}} = (3/4)c^{-2}[(1+\alpha^2)/(2\alpha^2)ln\left(\frac{1+\alpha}{1-\alpha}\right) - \alpha^{-2}] \tag{4.5}$$

where $\alpha^2 = 1 - c^{-3}$ and c is the contraction ratio found by $c = \frac{A_{inlet}}{A_{outlet}}$ in which A_{inlet} and A_{outlet} are the inlet and outlet area respectively. Working backwards from nozzle exit to the grid, $\overline{u_1u_1}_{in}$ can be found. Furthermore, since the flow is assumed to be HIT, $\overline{u_1u_1}_{in} = \overline{u_2u_2}_{in} = \overline{u_3u_3}_{in}$. Also, assuming $\overline{u_2u_2}_e = \overline{u_3u_3}_e$, the lateral energy ratio can be predicted through

$$\mu_2 = \mu_3 = \frac{\overline{u_2 u_{2_e}}}{\overline{u_2 u_{2_{in}}}} = (3/4)c + (3/4)c^{-2}((1/2)\alpha^{-2} - ((1-\alpha^2)/(4\alpha^3))ln\left(\frac{1+\alpha}{1-\alpha}\right)). \tag{4.6}$$

Knowing the amplification factors μ_1 and μ_2, the propagation of $\overline{u_1 u_1}$ and $\overline{u_2 u_2}$ can be approximated by

$$\overline{u_1 u_{1_e}} = \mu_1 * \overline{u_1 u_{1_{in}}}, \tag{4.7}$$

$$\overline{u_2 u_{2_e}} = \mu_2 * \overline{u_2 u_{2_{in}}}. \tag{4.8}$$

Considering $\overline{u_1 u_1}$ and $\overline{u_2 u_2} = \overline{u_3 u_3}$ in the assumption of RDT, the TKE can be calculated by

$$k = \frac{1}{2}(\overline{u_1 u_1} + 2\overline{u_2 u_2}). \tag{4.9}$$

Considering longitudinal length scale (L_{11_e}) is known at the exit of the nozzle, $L_{11_{in}}$ can be found through the relation

$$L_{11_{in}} = L_{11_e}/c^{0.5}. \tag{4.10}$$

The assumption of isotropy allows the following relations to be utilized:

$$L_{22_{in}} = \frac{L_{11_{in}}}{2}, \tag{4.11}$$

$$\lambda_{22_{in}} = \frac{\lambda_{11_{in}}}{\sqrt{2}}. \tag{4.12}$$

With known $L_{22_{in}}$ (equation 4.11), and through the use of equation 4.9 for the determination of TKE at the inlet of the contraction, k_{in}, $Re_{L_{in}}$ can be calculated by:

$$Re_{L_{in}} = \frac{k_{in}^{0.5} L_{22_{in}}}{\nu}. \tag{4.13}$$

By calculating $Re_{L_{in}}$, equation (4.13), and using equation (4.11), one can predict $\lambda_{22_{in}}$ through the use of equation

$$\frac{\lambda_{22_i}}{L_{22_i}} = \sqrt{10} Re_{L_i}^{-\frac{1}{2}}. \tag{4.14}$$

Then, knowing $\lambda_{22_{in}}$, it is possible to predict λ_{22_e} through

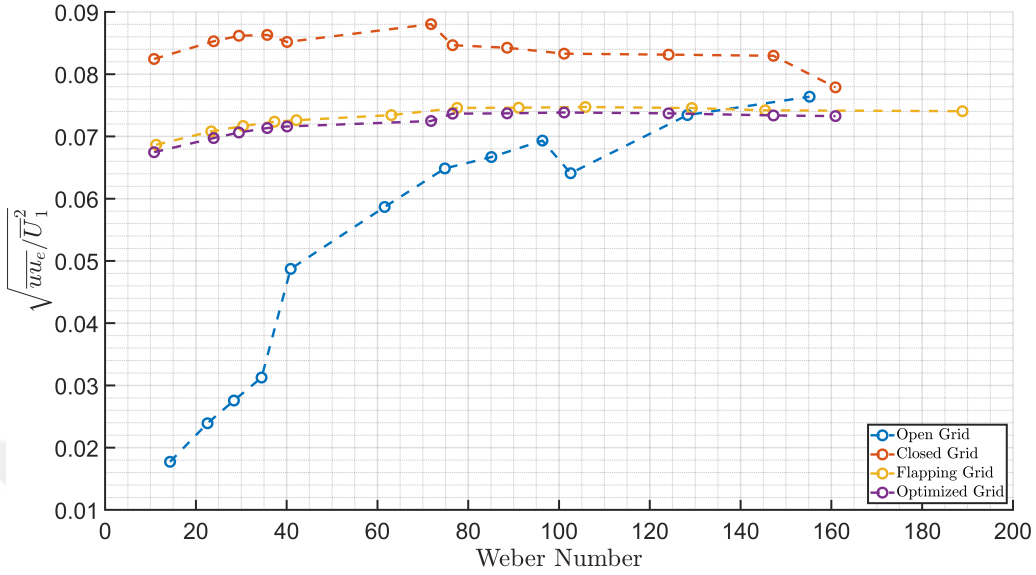
$$\lambda_{22_e} = \lambda_{22_{in}} \frac{1}{\sqrt{C_{L_{11}}}} \tag{4.15}$$

where $C_{L_{11}} = \frac{L_{11_e}}{L_{11_{in}}} = c^2 \frac{1}{\mu_2}$. Utilizing these relations, one can calculate the Taylor Reynold's Number at the exit of the nozzle which is given as

$$Re_{\lambda_e} = \frac{k_e^{0.5} \lambda_{22_e}}{v}. \tag{4.16}$$

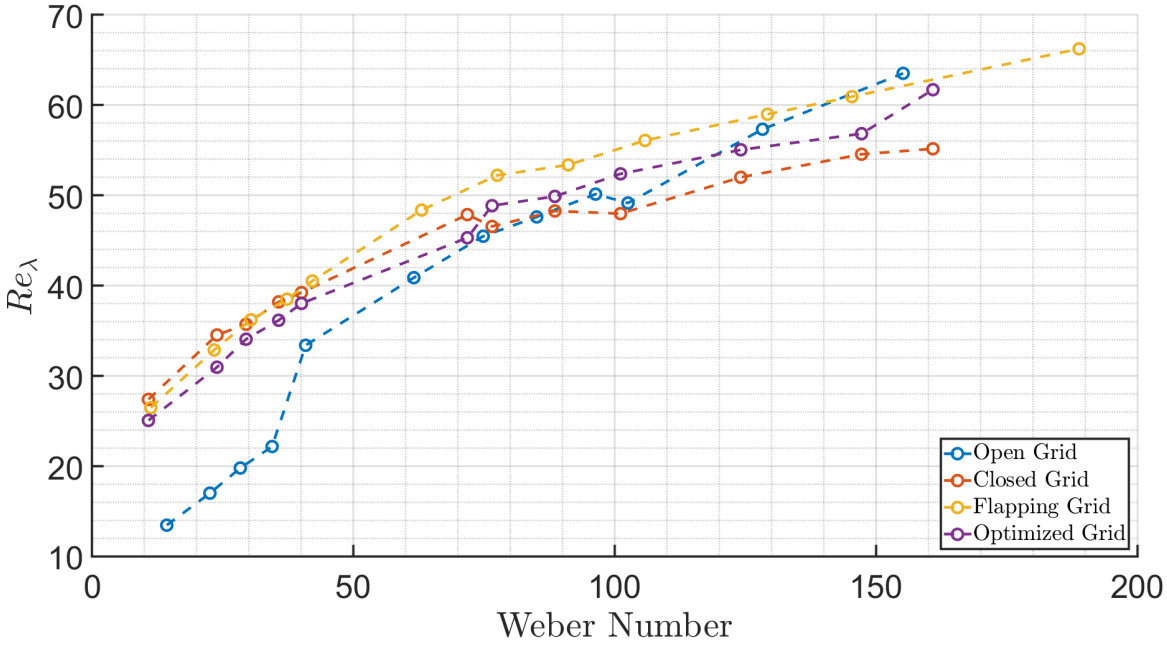
Through these relations, $\overline{u_1 u_{1e}}$, k_e, and Re_{λ_e} were calculated and plotted with respect to We. The $\overline{u_1 u_{1e}}$ and k_e intensity and Re_{λ_e} plots can be seen in Figure 4.9, , and 4.10 respectively.

Figure 4.9: *Intensity of longitudinal fluctuation.*



Although the intensity of $\overline{u_1 u_{1e}}$ can be considered constant for closed, flapping, and optimized grids, there is a tremendous increase in intensity for the open grid as We increases (Figure 4.9). A similar tendency can be seen in Figure and 4.10 in which open grid tends to have a sudden increase in turbulence intensity while the other grids show a decreasing trend. It seems that the turbulent effects induced by the grid diminishes as the We, or the flow velocity is increased. This behavior may be attributed to the onset of fully developed turbulence as the flow velocity increases. The results indicate a convergence in the characteristic length scale of turbulence, with the Taylor microscale approaching approximately 40 μm as the We increases, suggesting the formation of a well established inertial subrange as can be seen in 4.4.

Figure 4.10: *Taylor scale Reynolds number found through utilizing equation (4.16).*



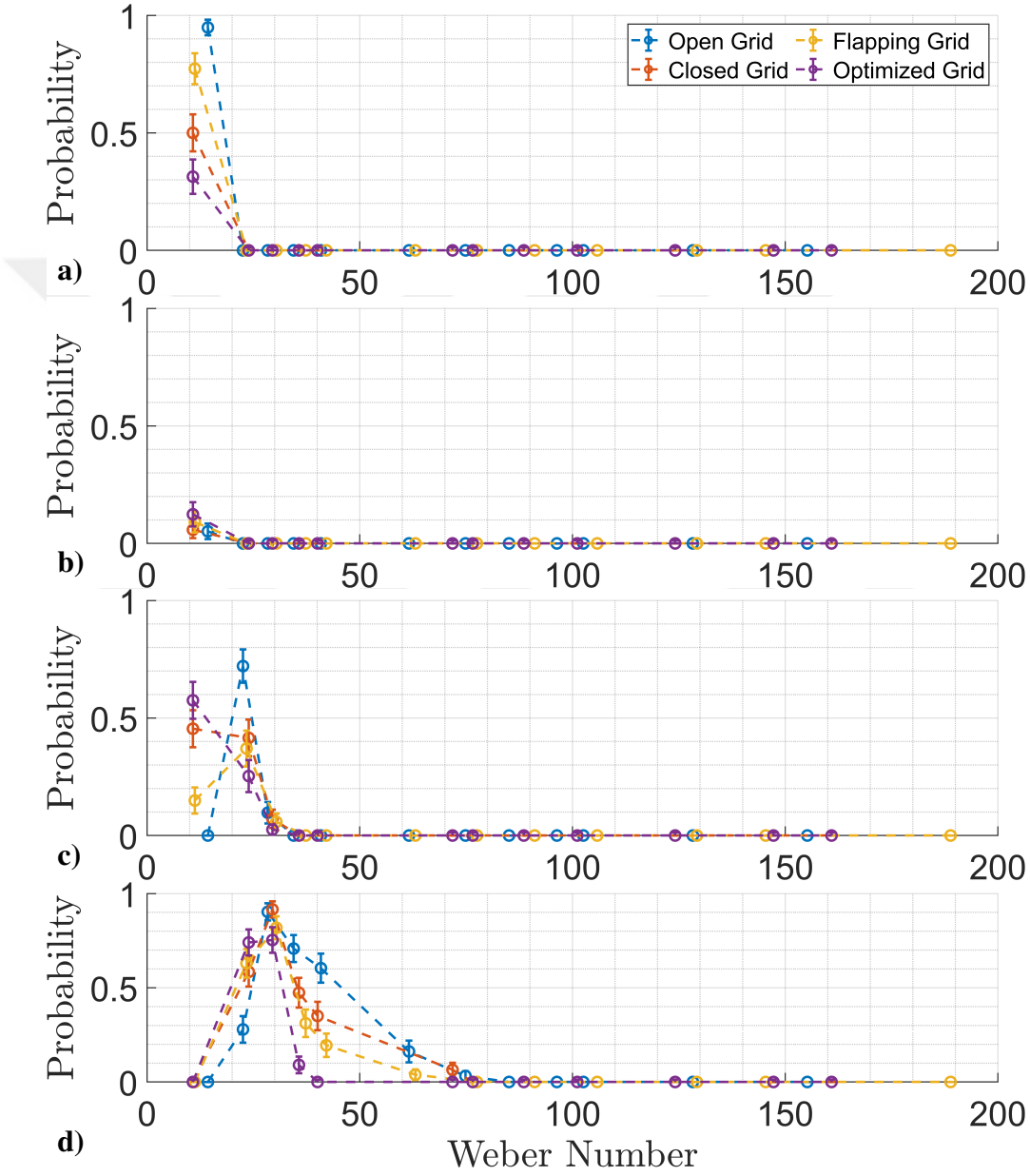
4.3 Effect of Turbulence on Atomization

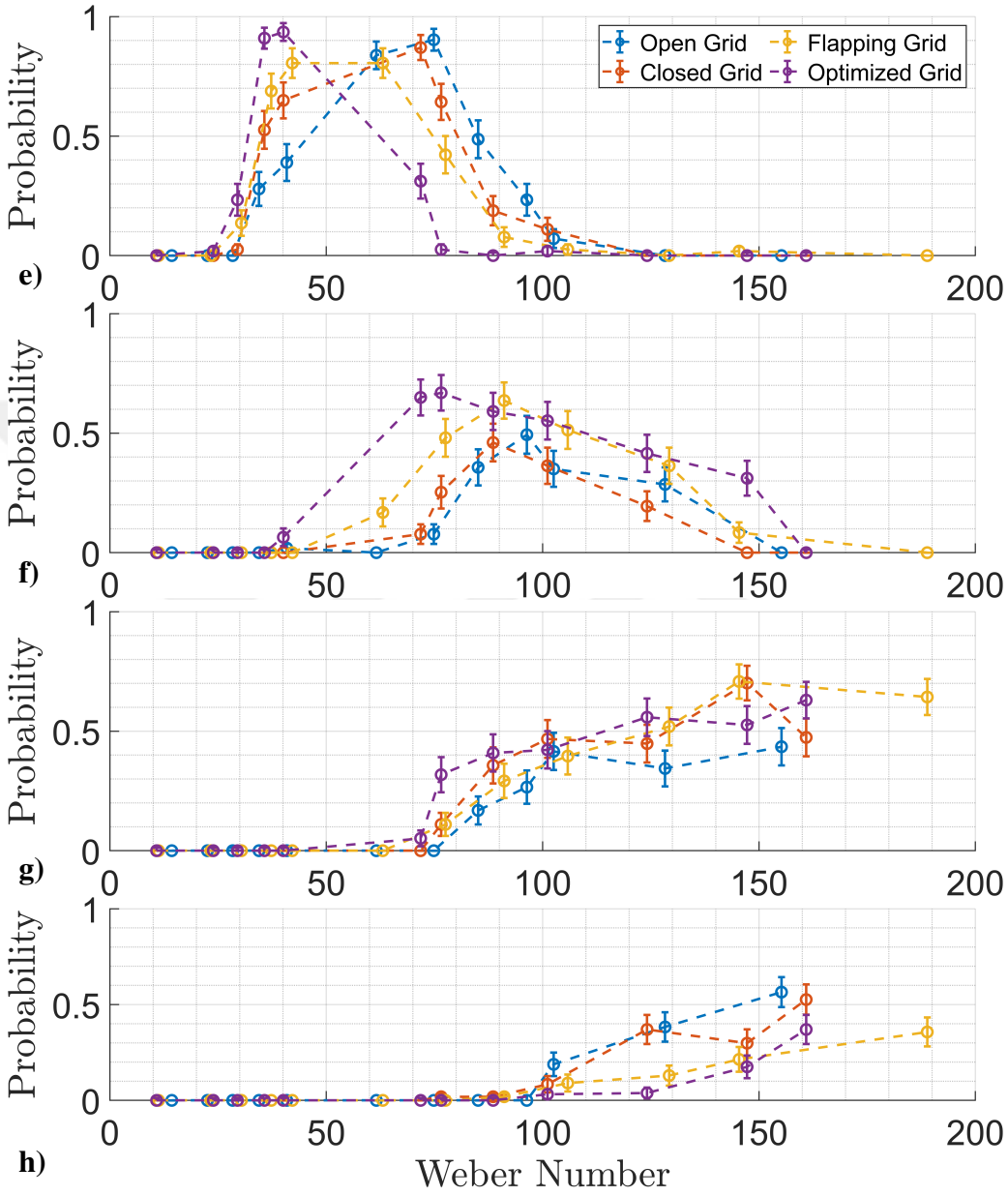
4.3.1 Break-up Modes and Probabilities

The effect of turbulence on droplet breakup statistics is clearly demonstrated in 4.11, which displays the frequency distribution of each breakup type as a function of We. Compared to the open grid configuration, the closed, flapping, and optimized grids exhibit sharp transitions in breakup statistics as the We increases. Specifically, these three grid types show rapid increases followed by rapid decreases in the occurrence frequencies of Bag, Bag-Stamen, Stamen-Multibag, and Multibag breakup modes as the We progresses. This distinct behavior persists until the We reaches approximately 100, at which point the turbulence characteristics of the open grid begin to converge with those of the other grid configurations.

Consequently, for higher We breakup modes such as Multibag and Sheet-Multibag, the statistical distributions become remarkably similar across all grid protocols. Furthermore, as the turbulence intensity of the open grid increases at these higher We, the breakup

Figure 4.11: *The probability of break-up modes with respect to We. The breakup types are as follows; a) no breakup, b) vibrational, c) bag, d) bag-stamen, e) stamen-multibag, f) multibag, g) sheet-multibag, h) sheet. The probability distributions are calculated using Wilson Score confidence intervals due to its robustness and reliability. The error bars indicate 95% confidence intervals.*



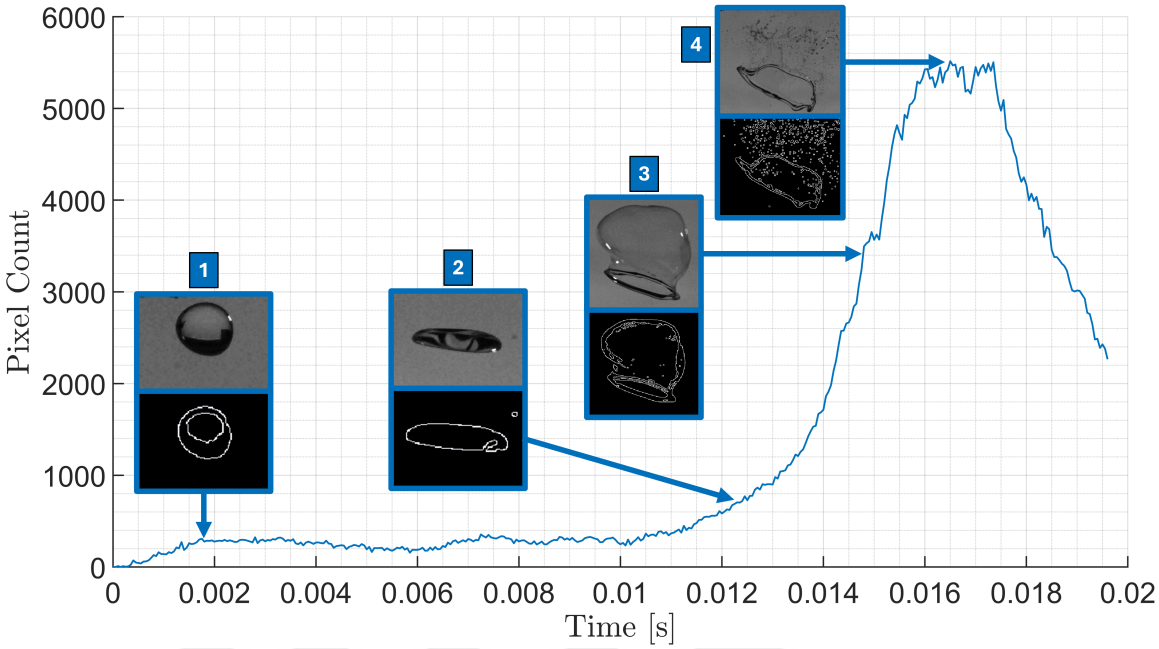

Open Grid
Flapping Grid
Closed Grid
Optimized Grid
Probability
e)
f)
g)
h)
0
0.5
1
50
100
150
200
Weber Number

statistics progressively align with those of the other grid types, eventually equalizing the breakup mode distributions across all configurations. However, for maximizing atomization efficiency at low We, the turbulence generated by the optimized grid should be preferred even though its turbulent characteristics are lower than those of the closed grid. Moreover, flapping and optimized grid protocols exhibit almost identical turbulence characteristics, yet the atomization is still more prominent in the optimized protocol. This clearly demonstrates how non-coherent local turbulent structures create force imbalances that drive the atomization process. While the flapping grid exhibits similar mechanisms, the eddy formation frequency differs considerably. The coherent flapping motion generates large eddies less frequently than the randomized optimized protocol. Consequently, droplets may restore force equilibrium between flaps, whereas the optimized protocol's continuous random motion has the probability of preventing this recovery. Thus, turbulence created by the optimized protocol can be considered as ideal mechanism.

4.3.2 Atomization Rate

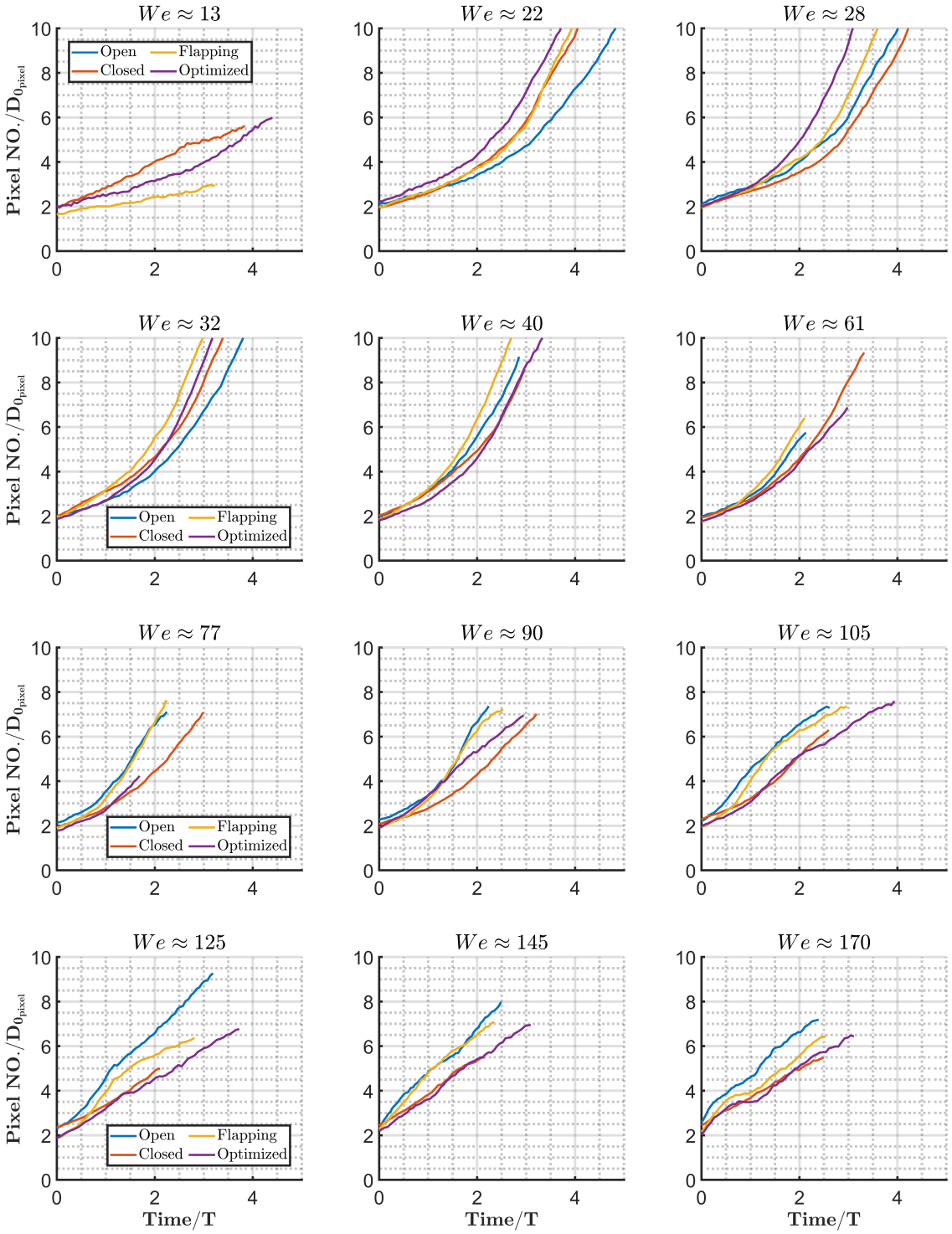
Figure 4.12 illustrates the stages of a bag breakup under closed grid conditions. In the first stage, the droplet is in its maximum stability phase immediately after leaving the stagnation tube. In the second stage, approximately 16 mm from the tip of the tube, the droplet assumes a "pancake" shape due to the influence of aerodynamic forces. In the third stage, the droplet further expands under the influence of these forces, developing into a bag shape. Finally, in the fourth stage, the droplet undergoes fine atomization as the bag structure erupts. The large particles visible in the images are approximately 0.25 mm in diameter.

Figure 4.12: *Droplet breakup process captured by image processing at $We \approx 24$ for the closed grid protocol.*



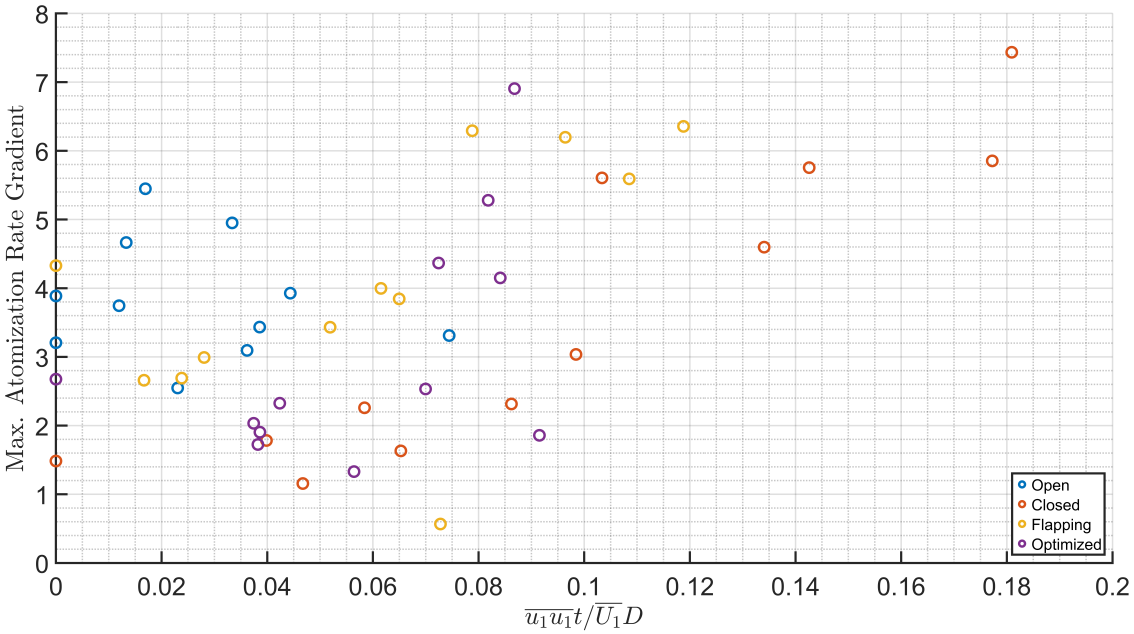
These images were processed using the Canny edge detection algorithm, applied to 16 droplets for each We case across four different active grid protocols. The edge detection algorithm identifies the white pixels along the edges of the droplets throughout the atomization process. To pinpoint the initiation of atomization, the ”findchangepts” function was utilized. This function detects points of abrupt change by analyzing statistical properties, enabling accurate identification of the onset of atomization. Only the curves corresponding to the initiation of atomization were considered in the analysis. The average of the 16 atomization curves for each We and active grid protocol was calculated to provide a comprehensive characterization of the atomization dynamics.

Figure 4.13: *The average rate of droplet breakup process vs. time normalized by integral time scale for* $11 \geq We \geq 170$ *at varying protocols. The pixel count is normalized by the initial droplet size,* $D_{0_{pixel}}$ *which is* ≈ 300 *pixels while time is normalized by integral time scale,* T.



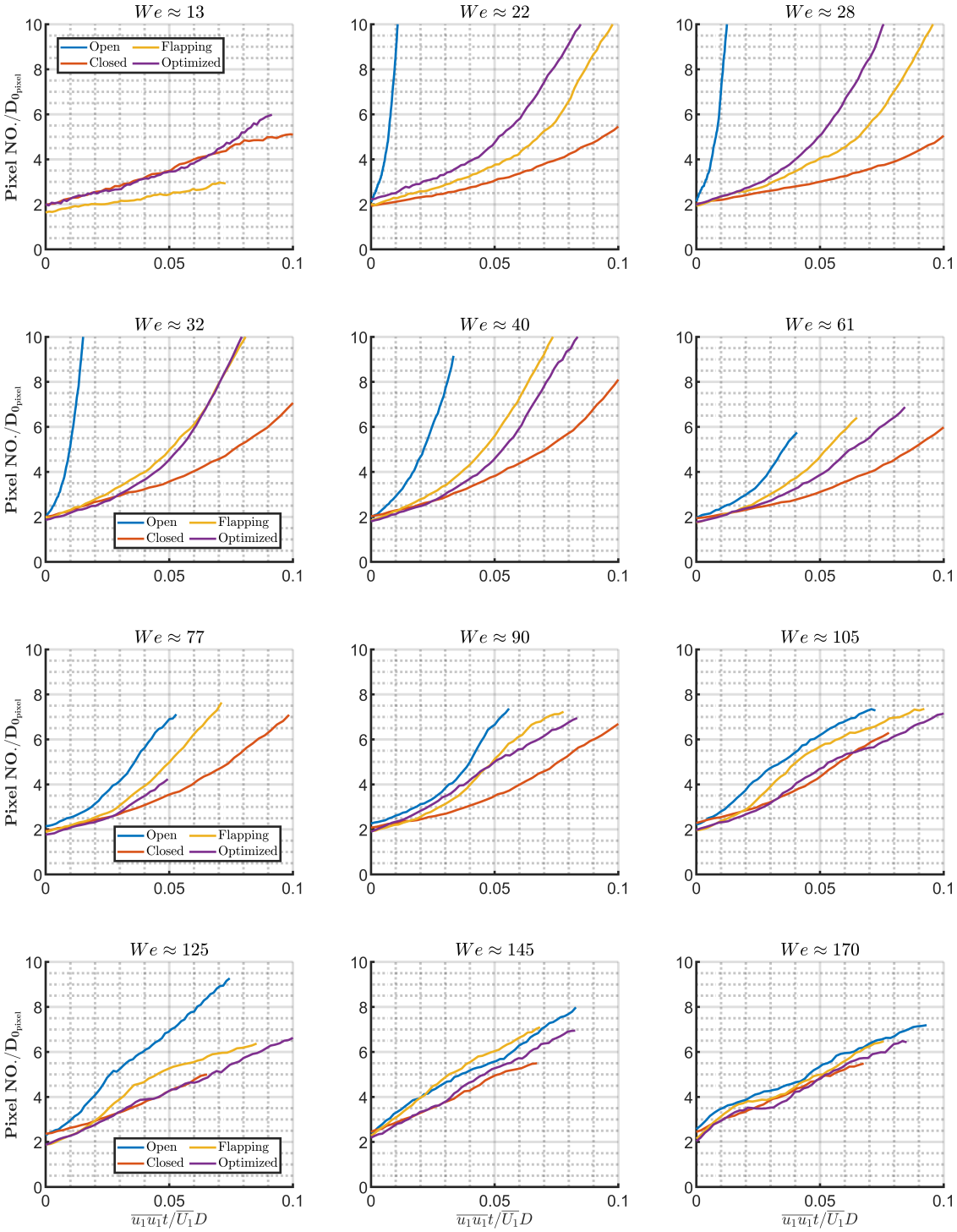
The average results obtained through image processing are presented in Figure 4.13. Note that the curves initiate at a pixel ratio of 2, as this is the point at which the droplet expands into a ”pancake” shape which can be seen at Figure 4.12. Notably, at lower We (We) ranges, protocols involving motion dominate the intensity at which droplets atomize. However, as We increases, the atomization rate of the optimized grid decreases drastically. Interestingly, as shown in Figure 4.11, the optimized grid exhibits better breakup statistics and earlier transition between morphologies, despite having turbulence characteristics that are quite similar to those of the flapping grid. This observation, also supported by Figure 4.14, suggests a more efficient atomization process under certain conditions. The scatter plot indicates that at lower turbulence intensities, where the mean velocity dominates, the atomization rate is improved. This phenomenon is best represented by the points represented by the open grid.

Figure 4.14: *Scatter plot of maximum gradients of mean atomization rate plots. Curve fit was applied as a method of filtering local fluctuations. Each fit is optimized according to its corresponding curve, then the maximum gradient is calculated.*



Furthermore, as the open grid show a drastic increase in $\overline{u_1 u_1}$ intensity with increasing We as seen in Figures 4.9 and 4.10, the open grid protocol begin to dominate the atomization rate levels at $We \approx 63$, while the closed grid protocol performs worse in comparison. This behavior may be attributed to the vortex shedding phenomenon, as the open grid can be regarded as a layered shaft arrangement that effectively functions as a passive grid. It is well-known that the passive grid turbulence levels increase with increasing gas velocities. While this trend is clearly observed for the open grid, the closed grid exhibits similarly intriguing behavior. Notably, it maintains an almost constant integral length scale (Figure 4.8) as well as consistent streamwise turbulence intensities, represented by $\overline{u_1 u_1}$. This behavior may also be attributed to its passive-grid nature, in line with the distinct characteristics displayed by the open grid. However, unlike the open grid, the closed grid demonstrates a more pronounced reduction in integral time scales with increasing velocity (Figure 4.7), which may explain its comparatively lower atomization rates. The shortened persistence of turbulent structures in time could limit their ability to deform and disrupt droplets, thereby reducing breakup effectiveness despite the presence of sustained spatial scales.

Figure 4.15: *The average rate of droplet breakup process vs. time normalized by* $\overline{u_1 u_1}$*, mean velocity* $\overline{U_1}$ *and droplet diameter* D *for* $11 \geq We \geq 170$ *at varying protocols.*



As observed in the high-speed atomization experiments, at higher We ($73 \leq We \leq 170$), droplets tend to exhibit a sheet stripping morphology, which is often followed by multiple bag-type breakups. These bags eventually collapse inward toward the central mass or "blob" of the droplet. Although this sequential breakup pattern is consistently observed across all grid protocols, the collapsing behavior appears to have a more pronounced effect on atomization rate in grids with higher blockage ratios. In the closed, flapping, and optimized grid configurations, the initial deformation begins with sheet formation at the periphery of the flattened ("pancaked") droplet. This evolves into multiple bag-like structures, which exhibit remarkably high atomization rates. However, the fragmented remnants still possessing the potential for further atomization, tend to collapse inward toward the core of the droplet, effectively suppressing further breakup as the core acts as a protective barrier against the flow. This behavior contrasts with that observed in the open grid configuration, where such collapse is less prominent, allowing more complete atomization to occur as can be seen from Figure 4.15. This is perhaps due to the uniform turbulent flow achieved by the open grid as it allows the droplets to expand, while the other grids prevent the droplet from expanding as much and results in a collapse towards its center possibly due to local pockets of high pressure regions formed by the turbulent structures. This effect is also evident in Figure 4.2, where the occurrence of sheet and sheet–multibag breakup modes is statistically more prominent in the open grid configuration, indicating its greater ability to generate well-defined sheet-type breakup compared to the other grid protocols. This may suggest that, at high We, the highly anisotropic turbulent flow, despite its chaotic nature, induces restorative forces that drive the droplet to collapse inward. This self-organizing behavior, arising from the turbulent fluctuations, results in a form of emergent order that ultimately inhibits further atomization.

Ultimately, it would be advised to utilize closed grid $We \leq 23$ for both better atomization probability and rates while for $23 \leq We \leq 83$, grids with implemented motion protocols would be ideal for obtaining earlier transition to desired breakup morphology and atomization rate. The reason for the inferior performance of motion protocol can be due to the formation frequency of the turbulent structures and the energy they contain as evident from Figure 4.7 and Figure 4.4 between frequency ranges of $1 \leq f \leq 100$. The closed grid contains lower times scales, meaning higher formation frequencies of eddies, and higher eddy energies between the given frequency range, even surpassing the energies obtained by open grid at $We \approx 13,155$, optimized grid $We \approx 11,170$, and flapping grid $We \approx 11,189$. It is evident that the motion protocols excel as the We increase as the frequency of eddy formation is promoted and larger structures are formed while closed grid displays a constant integral length scales. Finally, at $We \geq 83$, although its overall breakup probabilities are subpar, the open grid favors the sheet breakup and its atomization performance is superior compared to the other grids. This suggests that for given ranges of We, the protocols implemented to the active grid must carefully tailored for achieving optimal atomization characteristics.

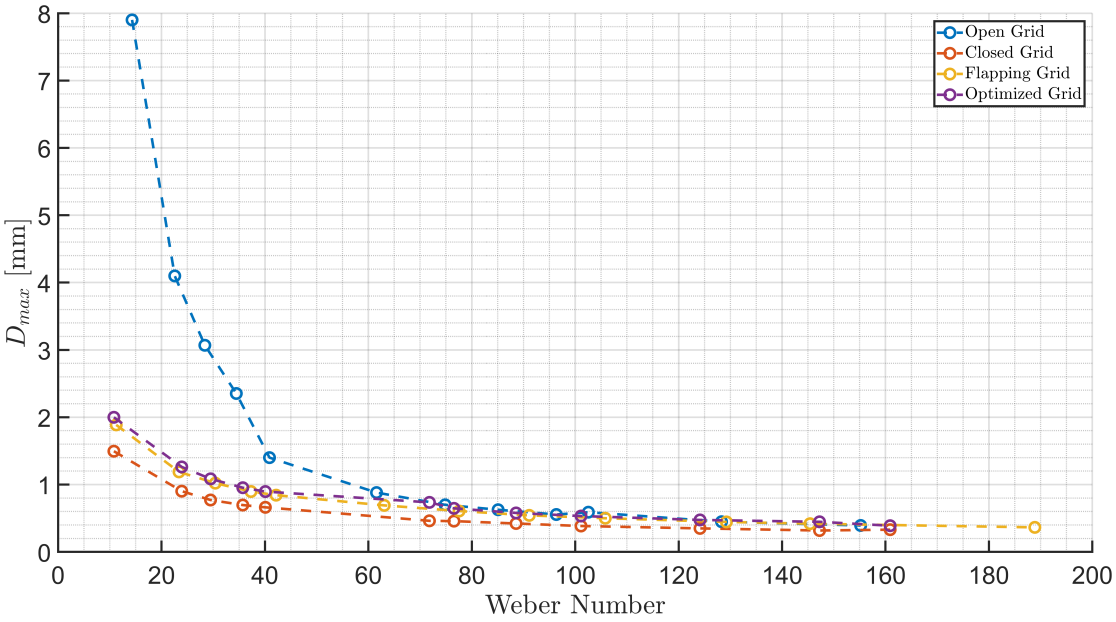
This hypothesis is further supported when the maximum stable diameter, D_{max} is calculated by approximating the turbulent dissipation rate. Although the assumption of isotropy is not strictly valid in this context, isotropic relations at the nozzle exit are used to approximate the dissipation rate.This approach is based on the equation:

$$\varepsilon = \frac{k^2}{Re_L \nu}. \tag{4.17}$$

Breakup is observed for a droplet diameter of 2.35 mm within the range $13 \leq We \leq 35$ under open grid conditions. However, according to Hinze's scaling law, the maximum stable droplet diameter is between $2.36 \leq D_{max} \leq 7.91$ millimeters as seen in Figure 4.16, which suggests that the atomization should not be possible due to turbulence.

Moreover, the generation of large, stable droplets is considerably difficult to achieve without the formation of satellite or daughter droplets. This process requires precise control of parameters such as injection pressure, mass flow rate, and nozzle geometry, as discussed in the work of [66]. It can be seen that the anisotropy of the turbulent flow significantly influences the breakup mechanisms.

Figure 4.16: *Maximum stable droplet diameter for each protocol at varying We.*



The obtained probability distributions of breakup types under various turbulent flow conditions can be integrated into a flow simulation software along with the turbulence modeling framework to predict breakup of droplets. Moreover, the findings here can be utilized to expand on Hinze's scaling law for better predictions. Such predictions have significant implications for applications including gas turbine combustion dynamics and spray technology optimization.

5. CONCLUSION AND FUTURE WORK

5.1 Conclusion

An experimental setup involving an active grid and a contracting nozzle was designed and manufactured to observe the droplet breakup mechanisms in anisotropic, strained turbulent flows. The characteristics of turbulence were altered by utilizing an active grid and the generated flow was strained with the help of a nozzle. Approximately 2.35 mm ethanol droplets were introduced to the strained turbulent flow and the disintegration process was captured by a high-speed camera. Hot-wire measurements were taken where the droplet atomization took place.

Effect of Active Grid Protocols on Generated Turbulence

- Turbulence measurements indicate that as the Weber number increases, the influence of the turbulence generation protocol on the turbulence statistics vary depending on the nature of the protocol.

- The passive grids, the open and the closed grids, are on the far sides of the spectrum as the open grid excels in terms of atomization rate at higher Weber ranges while closed grid excels at initiating droplet breakup at low Weber ranges.

- The motion protocols, namely the flapping and optimized grids, excel within the intermediate Weber ranges in terms early initiation of breakup morphologies and atomization rates.

- The resulting variations between the protocols are due to the frequencies involved within the turbulent flows. The closed grid displays high frequency and energetic eddies in low Weber ranges. As Weber number increases, the effect of closed grid diminishes as it produces eddies of similar sizes throughout the Weber number

range. Meanwhile, the motion protocols influence the flow so that ranges of eddies are formed, inducing extra energy to the flow. Finally the open grid most likely induces Von-Karman vortex shedding which progressively gets stronger with increasing velocities.

- This suggests that protocols can be tailored to optimize turbulence characteristics for given Weber ranges.

Effect of Generated Turbulence on Droplet Atomization

- The results suggest that at $We \leq 23$ higher probability of breakup is achieved with closed, flapping, and optimized grids. It is seen that the transition limits and morphologies are shifted towards lower Weber ranges specifically for the grids with implemented motion. Although open grid has subpar breakup probabilities compared to the other grids, it shows higher probabilities of sheet breakup morphology, since it is seen that the turbulence characteristics equalizes with respect to the other grids.

- Although open grid does not necessarily display any shift in morphology transition or better probabilities, it makes up by increased atomization rates due to the effect of turbulence on the droplets.

- The uniform turbulent flow achieved by the open grid inhibits the droplet from collapsing to itself, promoting a better atomization behavior when $83 \leq We \leq 170$. This behavior is also observed in the open grid, it is less prominent compared to the other grids.

- The formed core of the droplet after the peripheral atomization acts as a protective shield, which suppresses any further atomization attempts made by the turbulent

flow, resulting in poor atomization performance in closed, flapping, and optimized grids at high We ranges.

- As suggested earlier, by optimizing the grid protocols, the length scales along with energies of the turbulence structures can be tailored for achieving better atomization characteristics.

It is important to consider the trade-off between atomization rate and statistical performance. The optimized grid protocol yields better transition between breakup morphologies compared to the flapping grid while the flapping grid offers a better rate of atomization. The open grid, on the other hand, surpasses the atomization rate of the flapping grid at high Weber numbers, yet exhibits a relatively low probability of breakup in lower Weber ranges as it also does not offer any benefits in terms of breakup morphology transition. Depending on the specific objective of the application, this trade-off must be carefully evaluated. This raises a critical question: Should the priority be placed on ensuring consistent and reliable droplet atomization by maximizing breakup probability, or on achieving higher atomization rate to promote finer droplet sizes?

5.2 Future Works

For this study, only square winglets were used in the active grid. Circular winglets, which are available for use, could be implemented in future studies to explore variations in atomization and turbulence characteristics. Additionally, various combinations of protocols could be applied to the active grid to further improve atomization performance at higher inlet velocities. It is also possible that optimizing the size of the mesh could enhance the formed turbulent scales, allowing for better control over droplet atomization.Finally, various nozzle geometries and contraction rates can be tested to observe how changes in these parameters affect the overall performance.

The results from perpendicular hot-wire measurements were solely utilized in this analysis. Data for 30° slanted hot-wire measurements are available for post-processing; however, proper mathematical relations must be established to achieve appropriate calibration. Once calibrated, turbulence can be measured in all three components, providing a more comprehensive analysis.

Non-intrusive measurement techniques, such as PIV or Laser Doppler Anemometry (LDA), could be employed to visualize the turbulent field or the droplet atomization processes. For these techniques to be effective, the method of droplet introduction to the flow must be refined, as in high Weber number conditions, the droplet fails to travel far from the stagnation tube. Additionally, improvements in the droplet generation and introduction methods are necessary to ensure high-quality image processing for better analysis. Incorporating these improvements will allow the proper measurements necessary for predicting breakup time, fragmentation velocity and droplet size distributions.

6. END SECTIONS

6.1 Bibliography

The references should be listed in order of appearance. We use the standard IEEE transactions bibliography style in the thesis. You should add your references to the bibliography.bib file according to its type. Several common examples are added to bibliography.bib for your use. Further information on other document types can be found at [**?**].

Now, let us cite some studies: one source as [**?**], two sources as [**?**, **?**] or you may cite three or more sources as [**?**, **?**, **?**, **?**, **?**, **?**, **?**, **?**].

6.2 Appendices

Ancillary material should be put in appendices, which appear just after the bibliography. An example is added for you to the main.tex file.

REFERENCES

[1] M. Pilch and C. Erdman, "Use of breakup time data and velocity history data to predict the maximum size of stable fragments for acceleration-induced breakup of a liquid drop," *International journal of multiphase flow*, vol. 13, no. 6, pp. 741–757, 1987.

[2] L.-P. Hsiang and G. M. Faeth, "Near-limit drop deformation and secondary breakup," *International journal of multiphase flow*, vol. 18, no. 5, pp. 635–652, 1992.

[3] I. M. Jackiw and N. Ashgriz, "On aerodynamic droplet breakup," *Journal of Fluid Mechanics*, vol. 913, p. A33, 2021.

[4] D. Guildenbecher, C. López-Rivera, and P. Sojka, "Secondary atomization," *Experiments in Fluids*, vol. 46, no. 3, pp. 371–402, 2009.

[5] J. O. Hinze, "Fundamentals of the hydrodynamic mechanism of splitting in dispersion processes," *AIChE journal*, vol. 1, no. 3, pp. 289–295, 1955.

[6] S. A. Krzeczkowski, "Measurement of liquid droplet disintegration mechanisms," *International Journal of multiphase flow*, vol. 6, no. 3, pp. 227–239, 1980.

[7] M. Jain, R. S. Prakash, G. Tomar, and R. Ravikrishna, "Secondary breakup of a drop at moderate weber numbers," *Proceedings of the Royal Society A: Mathematical, Physical and Engineering Sciences*, vol. 471, no. 2177, p. 20140930, 2015.

[8] T. Theofanous, G. Li, and T. Dinh, "Aerobreakup in rarefied supersonic gas flows (keynote)," in *Fluids Engineering Division Summer Meeting*, vol. 36967, pp. 1685–1703, 2003.

[9] T. Theofanous, "Aerobreakup of newtonian and viscoelastic liquids," *Annual Review of Fluid Mechanics*, vol. 43, no. 1, pp. 661–690, 2011.

[10] T. Theofanous, V. Mitkin, C. Ng, C. Chang, X. Deng, and S. Sushchikh, "The physics of aerobreakup. ii. viscous liquids," *Physics of Fluids*, vol. 24, no. 2, 2012.

[11] D. D. Joseph, J. Belanger, and G. Beavers, "Breakup of a liquid drop suddenly exposed to a high-speed airstream," *International Journal of Multiphase Flow*, vol. 25, no. 6-7, pp. 1263–1303, 1999.

[12] R. Andersson and B. Andersson, "Modeling the breakup of fluid particles in turbulent flows," *AIChE Journal*, vol. 52, no. 6, pp. 2031–2038, 2006.

[13] M. M. Clark, "Drop breakup in a turbulent flow—i. conceptual and modeling considerations," *Chemical engineering science*, vol. 43, no. 3, pp. 671–679, 1988.

[14] R. Skartlien, E. Sollum, and H. Schumann, "Droplet size distributions in turbulent emulsions: breakup criteria and surfactant effects from direct numerical simulations," *The Journal of chemical physics*, vol. 139, no. 17, 2013.

[15] N. Vankova, S. Tcholakova, N. D. Denkov, I. B. Ivanov, V. D. Vulchev, and T. Danner, "Emulsification in turbulent flow: 1. mean and maximum drop diameters in inertial and viscous regimes," *Journal of Colloid and Interface Science*, vol. 312, no. 2, pp. 363–380, 2007.

[16] A. Begemann, T. Trummler, E. Trautner, J. Hasslberger, and M. Klein, "Effect of turbulence intensity and surface tension on the emulsification process and its stationary state—a numerical study," *The Canadian Journal of Chemical Engineering*, vol. 100, no. 12, pp. 3548–3561, 2022.

[17] P. J. O'Rourke and A. A. Amsden, "The tab method for numerical calculation of spray droplet breakup," tech. rep., SAE technical paper, 1987.

[18] J. C. Lasheras, C. Eastwood, C. Martınez-Bazán, and J. L. Montañes, "A review of statistical models for the break-up of an immiscible fluid immersed into a fully developed turbulent flow," *International Journal of Multiphase Flow*, vol. 28, no. 2, pp. 247–278, 2002.

[19] S. B. Pope, *Turbulent Flows*. Cambridge University Press, 2000.

[20] O. Reynolds, "Iv. on the dynamical theory of incompressible viscous fluids and the determination of the criterion," *Philosophical transactions of the royal society of london.(a.)*, no. 186, pp. 123–164, 1895.

[21] L. Prandtl, "Report on investigation of developed turbulence," *Zeitschrift fuer Angewandte Matematik und Mechanik*, vol. 5, no. NACA-TM-1231, 1949.

[22] E. R. Van Driest, "On turbulent flow near a wall," *Journal of the aeronautical sciences*, vol. 23, no. 11, pp. 1007–1011, 1956.

[23] A. Smith and T. Cebeci, "Numerical solution of the turbulent-boundary-layer equations," tech. rep., DOUGLAS AIRCRAFT CO LONG BEACH CA AIRCRAFT DIV, 1967.

[24] B. Baldwin and H. Lomax, "Thin-layer approximation and algebraic model for separated turbulent flows," in *16th aerospace sciences meeting*, p. 257, 1978.

[25] W. P. Jones and B. E. Launder, "The prediction of laminarization with a two-equation model of turbulence," *International journal of heat and mass transfer*, vol. 15, no. 2, pp. 301–314, 1972.

[26] B. Launder, "Turbulence modelling for cfd. by dc wilcox. dcw industries inc., 1993. 460pp. $75.," *Journal of Fluid Mechanics*, vol. 289, pp. 406–407, 1995.

[27] T.-H. Shih, W. W. Liou, A. Shabbir, Z. Yang, and J. Zhu, "A new k- eddy viscosity model for high reynolds number turbulent flows," *Computers & fluids*, vol. 24, no. 3, pp. 227–238, 1995.

[28] F. R. Menter, "Two-equation eddy-viscosity turbulence models for engineering applications," *AIAA journal*, vol. 32, no. 8, pp. 1598–1605, 1994.

[29] F.-S. Lien, "Low-reynolds-number eddy-viscosity modelling based on non-linear stress-strain/vorticity relations," in *Proc. 3rd Symposium On Engineering Turbulence Modelling and Measurements*, pp. 1–10, 1996.

[30] A. Hellsten, "New advanced kw turbulence model for high-lift aerodynamics," *AIAA journal*, vol. 43, no. 9, pp. 1857–1869, 2005.

[31] P. R. Spalart, "Strategies for turbulence modelling and simulations," *International journal of heat and fluid flow*, vol. 21, no. 3, pp. 252–263, 2000.

[32] B. E. Launder and N. D. Sandham, *Closure strategies for turbulent and transitional flows*. Cambridge University Press, 2002.

[33] C. G. Speziale, S. Sarkar, and T. B. Gatski, "Modelling the pressure–strain correlation of turbulence: an invariant dynamical systems approach," *Journal of fluid mechanics*, vol. 227, pp. 245–272, 1991.

[34] Özgür Ertunç, "Derivations of the transport equations for the reynolds stresses, the turbulence kinetic energy, and its dissipation rate," tech. rep., Özyeğin University, 2025.

[35] M. Gibson and B. Launder, "Ground effects on pressure fluctuations in the atmospheric boundary layer," *Journal of Fluid Mechanics*, vol. 86, no. 3, pp. 491–511, 1978.

[36] H. S. Ribner and M. Tucker, *Spectrum of turbulence in a contracting stream*, vol. 1113. National Advisory Committee for Aeronautics, 1952.

[37] G. K. BATCHELOR and I. PROUDMAN, "The effect of rapid distortion of a fluid in turbulent motion," *The Quarterly Journal of Mechanics and Applied Mathematics*, vol. 7, pp. 83–103, 01 1954.

[38] L. Prandtl, "Attaining a steady air stream in wind tunnels," tech. rep., National Advisory Committee for Aeronautics, 1933.

[39] G. Taylor, "Turbulence in a contracting stream," *ZAMM-Journal of Applied Mathematics and Mechanics/Zeitschrift für Angewandte Mathematik und Mechanik*, vol. 15, no. 1-2, pp. 91–96, 1935.

[40] V. Mugundhan, R. Pugazenthi, N. B. Speirs, R. Samtaney, and S. T. Thoroddsen, "The alignment of vortical structures in turbulent flow through a contraction," *Journal of Fluid Mechanics*, vol. 884, p. A5, 2020.

[41] Özgür Ertunç, *Experimental and Numerical Investigations of Axisymmetric Turbulence*. PhD thesis, University of Erlangen-Nuremberg, 2007.

[42] M. S. Uberoi, "Effect of wind-tunnel contraction on free-stream turbulence," *Journal of the Aeronautical Sciences*, vol. 23, no. 8, pp. 754–764, 1956.

[43] A. Hussain and V. Ramjee, "Effects of the axisymmetric contraction shape on incompressible turbulent flow," *ASME: Journal of Fluids Engineering*, 1976.

[44] J. L. L. Hunt Tennekes, "A first course in turbulence," *Journal of Fluid Mechanics*, vol. 58, no. 4, p. 816–819, 1973.

[45] K.-S. CHOI and J. L. LUMLEY, "The return to isotropy of homogeneous turbulence," *Journal of Fluid Mechanics*, vol. 436, p. 59–84, 2001.

[46] Ertunç and F. Durst, "On the high contraction ratio anomaly of axisymmetric contraction of grid-generated turbulence," *Physics of Fluids*, vol. 20, p. 025103, 02 2008.

[47] R. R. Mills and S. Corrsin, "Effect of contraction on turbulence and temperature fluctuations generated by a warm grid," *NASA Memorandum*, vol. 47, no. 1959, pp. 31–47, 1959.

[48] L. Mydlarski and Z. Warhaft, "On the onset of high-reynolds-number grid-generated wind tunnel turbulence," *Journal of Fluid Mechanics*, vol. 320, pp. 331–368, 1996.

[49] H. Makita and K. Sassa, "Active turbulence generation in a laboratory wind tunnel," in *Advances in Turbulence 3: Proceedings of the Third European Turbulence Conference Stockholm, July 3–6, 1990*, pp. 497–505, Springer, 1991.

[50] A. N. Kolmogorov, "The local structure of turbulence in incompressible viscous fluid for very large reynolds numbers," *Proceedings of the Royal Society of London. Series A: Mathematical and Physical Sciences*, vol. 434, no. 1890, pp. 9–13, 1991.

[51] J. V. Larssen, *Large scale homogeneous turbulence and interactions with a flat -plate cascade*. PhD thesis, Virginia Polytechnic Institute, 2005. Copyright - Database copyright ProQuest LLC; ProQuest does not claim copyright in the individual underlying works; Last updated - 2023-03-03.

[52] J. V. Larssen and W. J. Devenport, "On the generation of large-scale homogeneous turbulence," *Experiments in fluids*, vol. 50, no. 5, pp. 1207–1223, 2011.

[53] R. J. Hearst and P. Lavoie, "The effect of active grid initial conditions on high reynolds number turbulence," *Experiments in Fluids*, vol. 56, no. 10, p. 185, 2015.

[54] H. L. E. J. T. Skeledzic, J. Krauss, "Characterization of turbulence generated by an active grid with individually controllable paddles," in *New Results in Numerical and Experimental Fluid Mechanics XI: Contributions to the 20th STAB/DGLR Symposium Braunschweig, Germany, 2016*, vol. 136, pp. 105–114, Springer, 2017.

[55] H. E. Cekli and W. van de Water, "Tailoring turbulence with an active grid," *Experiments in fluids*, vol. 49, no. 2, pp. 409–416, 2010.

[56] G. Comte-Bellot and S. Corrsin, "Simple eulerian time correlation of full-and narrow-band velocity signals in grid-generated,'isotropic'turbulence," *Journal of fluid mechanics*, vol. 48, no. 2, pp. 273–337, 1971.

[57] H. S. Kang, S. Chester, and C. Meneveau, "Decaying turbulence in an active-grid-generated flow and comparisons with large-eddy simulation," *Journal of Fluid Mechanics*, vol. 480, pp. 129–160, 2003.

[58] A. Akardere, "Les analysis of turbulence generated by active grid : Effect of winglets and motion protocol," Master's thesis, Özyeğin University, 2024.

[59] A. Akardere, A. M. Karul, and Ö. Ertunç, "Large eddy simulations of active grid turbulence generators," *ICHMT DIGITAL LIBRARY ONLINE*, 2024.

[60] L. Mydlarski, "A turbulent quarter century of active grids: from makita (1991) to the present," *Fluid Dynamics Research*, vol. 49, no. 6, p. 061401, 2017.

[61] V. C. Coşar, "Investigations of atomization of droplets in turbulent flows," Master's thesis, Özyeğin University, 2022.

[62] R. Porte and A. Biesheuvel, "Experiments on the motion of gas bubbles in homogeneous isotropic turbulence," *Journal of Fluid Mechanics*, vol. 461, pp. 127–154, 2002.

[63] A. Klein and V. Ramjee, "Effects of contraction geometry on non-isotropic free-stream turbulence," *Aeronautical Quarterly*, vol. 24, no. 1, pp. 34–38, 1973.

[64] H. H. Bruun, "Hot-wire anemometry: principles and signal analysis," *Measurement Science and Technology*, vol. 7, no. 10, p. 024, 1996.

[65] D. S. Wilson, "Confidence intervals for motion and deformation of the juan de fuca plate," *Journal of Geophysical Research: Solid Earth*, vol. 98, no. B9, pp. 16053–16071, 1993.

[66] V. C. Coşar, O. Şen, Ö. Ertunç, S. Qureshi, and Ö. Bebek, "A solenoid injector based drop-on-demand system for generating large droplets," *Review of Scientific Instruments*, vol. 94, no. 9, 2023.